Metal Oxide Thin Film Growth by Laser Ablation and Its Applications in High Surface Area Photoanodes

Rudresh Ghosh

A dissertation submitted to the faculty of the University of North Carolina at Chapel Hill in partial fulfillment of the requirements for the degree of Doctor of Philosophy in the Department of Physics and Astronomy.

Chapel Hill
2012

Approved by:

Rene Lopez

Charles Evans

Laurie E McNeil

Thomas J Meyer

Edward T Samulski

Abstract

Rudresh Ghosh: Metal Oxide Thin Film Growth by Laser Ablation and Its
Applications in High Surface Area Photoanodes
(Under the direction of Rene Lopez)

Thin films are widely used in various applications, including but not limited to simple reflective coatings for mirrors, electrodes for lithium batteries, conducting substrates for electronic circuits, gas sensors and solar cells. As the scope of their applications has widened over the years so has the need to obtain different structural motifs for thin films. A large variety of fabrication techniques are commonly employed to obtain these structures. Pulsed laser deposition (PLD) can be used to obtain films varying from extremely compact and only a few angstroms thick to micron thick porous structures. In this dissertation I introduce a model for predicting different structures as a function of laser parameters and deposition environments in a pulsed laser deposition system. This is followed by a comparison of simulated and experimentally obtained structures. I then use this model to obtain tailored structures suited for individual applications. One of the unique structures obtained using the PLD consists of vertically-aligned structures with nanoparticles as their building blocks. I investigate the superiority of this unique structure over random nanoparticle networks as photoanodes for titanium dioxide (TiO_2)-based dye- sensitized solar cells (DSSC). UV-Vis studies show that there is a 1.4 x enhancement of surface area for PLD-TiO_2 photoanodes compared to the best sol-gel films. PLD-TiO_2 incident photon to current efficiency (IPCE) values are comparable to 3 x thicker sol-gel films and nearly 92% absorbed photon to current efficiency (APCE) values have been observed for optimized structures. I also examine the suitability of PLD-synthesized niobium oxide (Nb_2O_5) and tantalum-doped titanium

oxide (Ta: TiO_2) as photoanode materials. For optimized PLD-Nb_2O_5-based DSSCs IPCE values up to 40%, APCE values around 90% and power conversion efficiency of 2.41% were obtained. DSSCs made of PLD-Ta:TiO_2 show enhanced photocurrents as well photo efficiency over those based on PLD-TiO_2. I show that this improvement is due to the slower recombination rates because of the presence of Ta^{5+}. I also show the applicability of other structures obtained using the PLD. I use very compact thin films for obtaining the band edges of different potential candidates suitable for photoanodes of dye sensitized photoelectrochemical cells (DSPEC). This is done by a combination of x-ray and ultraviolet photoemission spectroscopy (XPS-UPS) and inverse photoemission spectroscopy (IPS). I also use porous tungsten oxide (WO_3) PLD films as H_2 sensors. I determine the optical constants for WO_3 in the colored and bleached states and use them to correlate the gasochromic and electrochromic behavior of WO_3. I also introduce polymer encapsulation of WO_3 thin films to protect them from aging.

Acknowledgements

I would Like to start of by thanking my advisor, Dr Rene Lopez. His way of letting me do my own things yet prodding me towards the final destination, helped me in becoming independent without getting lost in thousands of different directions. He was always there to offer advise, support and enthusiasm.

I would also like to thank all my committee members for being a part of this effort. Provided me with many inputs at all times. I am thankful that I had so many extremely brilliant scientists to show me what being a researcher was all about. Most importantly for me them gave me confidence and pushed me towards being a better overall scientist.

All the work in this thesis is more a testament of the really intelligent scientists I have met over the course of my graduate work. I have recieved support and advice from collaborators within and outside of UNC. I have been trained on experimental techniques, analysis methods and presentation skills by a bunch of extremely talented people. I have constantly asked for help and never been said no to.

I would like to thank all the lovely people at CHANL. Every grad student thinks their research is the most important thing in the world. You guys knew better, yet played along. Everytime I did something stupid with the instruments you guys made me feel like it was not really my fault. I have never been without the support of CHANL and really dont know how research was done here before you guys.

I would also like to thank the people at UNC-EFRC. I would like to thank for all the instrumentation provided. But more importantly for bringing people with extremely

diverse research and channeling their efforts towards a common goal.

This would be a good time for me to also thank the unofficial mentors I have had. Kyle, I really did not know anything at all about dye sensitized solar cells, photophysics, instrumentation or chemistry. Thank you so much for all the help to not only get me started , but helping me everytime I needed. Thank you for all the help with the numerous talks and papers. Ken, as I said to you once, I felt lost everytime people spoke in the language of chemistry. Thank you for translating that into a language i understand. Thank you for helping me in projects that you had absolutely no reason to. Thank you for editing so many things that I wrote, scientific or otherwise. Paul, I would like to thank you for all the advice with the different projects. You always seemed to know the right recipes, methods and explanations for physical processes that puzzled me. Leila, your help with the devices lab is so highly appreciated. Thanks for all the support in the different projects, even the ones that you and I knew would not work.

I would like to thank not only my lab mates but everyone in the basement of Chapman. I have borrowed things from every lab, walked in talking loudly in the middle of what I later realized were possibly important scientific conversations. We started our own basement soccer league and that I am prety sure has not happened on any other floors of Chapman or any other research building.

I would also like to thank the people who have not known me professionally but have helped me keep my sanity. I would like to thank the lunch group for all the weird conversations we have had. All the soccer people for allowing me to call you names and force you into playing soccer even when it made no sense to. I would like to thank so many of my friends for the rides to and from different places.

I would like to also thank my family (my mom, dad and Urmila masi) for their love and support. I would like to thank my sister for all the inspiration and tough love. If it had not been for her following a career in science I would most probably not be doing

it either.

I would also like to thank my partner, Oana Lungu. Her drive for excellence and ambition has definitely helped me work harder. Her love for the science she does made me more passionate about mine.

Thank you everyone.

Table of Contents

List of Tables

List of Figures

List of Abbreviations

PLD: Pulsed laser deposition

DSSC: Dye sensitized solar cell

IPCE: Incident photon to current efficiency

APCE: Absorbed photon to current efficiency

DSPEC: Dye sensitized photoelectrochemical cell

XPS: X-ray photoelectron spectroscopy

UPS: Ultra violet photoelectron spectroscopy

IPS: Inverse photo emission spectroscopy

CNT: Carbon nanotube

ICCD: Integrated charge coupled device

SEM: Scanning electron microscope

TEM: Transmission electron microscope

AFM: Atomic force microscope

TCO: Transparent conducting oxide

HOMO: Highest occupied molecular orbital

LUMO: Lowest unoccupied molecular orbital

CB: Conduction band

MLCT: Metal to ligand charge transfer

TBP: 4-tert-Butylpyridine

IMVS: Intensity-modulated-voltage spectroscopy

ITO: Indium tin oxide

FTO: Fluorine doped tin oxide

LHE: Light Harvesting Efficiency

EIS: Electrochemical impedance spectroscopy

Voc: Open circuit voltage

Jsc: Short circuit current density

UHV: Ultra high vacuum

CMA: Cylindrical mirror analyzer

VBM: Valence band maximum

CBN: Conduction band minimum

EA: Electron affinity

PDMS: Polydimethylsiloxane

RBS: Rutherford back scattering

MSE: standard mean squared errors

Chapter 1

Introduction

1.1 Motivation

Human ingenuity has produced great technological advances in the last few centuries. This technological progress has improved our overall quality of life. However, it has come at the cost of large amounts of energy consumption. If this trend continues, we can anticipate doubling of the world's energy needs by 2050 and tripling by 2100. The increased energy demand has been met over the last couple of decades mostly by fossil fuels. However, the limited availability of these resources as well as their adverse environmental effects have forced us to look for other sources of energy.

One of the main alternative avenues being pursued is direct harvesting of the sun's energy. In order for the sun to become a viable alternative to fossil fuels we need to be able to harness this energy cheaply and efficiently. Dye sensitized solar cells (DSSC) provide hope of such a solar cell. However, for solar energy to become the primary energy resource we need to improve the efficiency of the devices used to harvest it to at least close to their theoretical maximum. In order for this to happen we need to vigorously investigate the possible bottlenecks in the current device architecture.

1.2 Thesis Contributions

One of the known bottlenecks for enhanced DSSC performance is the random nanoparticle network that is conventionally used. In this thesis we investigate the effects of different film morphologies on device behavior. Unlike the conventional sol gel method we have used pulsed laser deposition (PLD) in order to be able to tailor the film structures. The high-energy ablation process as well as the decoupling of the evacuation and deposition steps allows PLD to be used under different reactive and non-reactive growth environments. This allows us to play with different growth parameters to obtain tailored structures using this process. Besides just investigating film structures we have also explored the suitability of other materials with potential to replace TiO_2 as the only DSSC photoanode material.

1.3 Document outline

In order to be able to tailor structures for different applications it is necessary to know how the film of interest grows by PLD. In the beginning of chapter 2 I briefly talk about the development in laser systems that helped in the getting to the present state of PLD systems. This is followed by an overview of the functioning of our PLD system. Next I discuss about the different occurrences at the different time scales after laser ablation of the material. I then introduce a model for the film deposition starting from particles and their interactions as they travel in the target-substrate region. Experimental and modeled structures are compared as well.

Chapter 3 explains the working principles of DSSCs. I start with a energy level description of the device components. This is then followed by a discussion of the effect of different properties of materials used for the devices. Understanding of the working of the DSSC leads me to the proper choice of materials for these devices. Next I talk

about the different characterization techniques and the experimental setups I have used.

Chapter 4 focuses on the optimization of photoanodes for DSSCs. In the first section I compare PLD-based TiO_2 to conventional sol gel-based TiO_2 photoanodes. I also discuss film morphology and its effect on device performance. The next section deals with photoanodes made of Niobia (Nb_2O_5). In this section I describe growth conditions and the resulting structures. This is followed by comparing device performance for different structures for this new material as a photoanode. The third part investigates TiO_2 doped with a metal (Ta). Knowledge from earlier sections is used to synthesize hierarchical, high-surface-area structures for Ta-doped TiO_2 and undoped TiO_2. Photophysical performance of the two types of photoanodes are compared. I discuss what might be the cause of the differences in performance.

Chapter 5 investigates other possible applications of PLD's ability to tailor film structures. I also talk about potential applications for our methods for hybrid-photovoltaics and DSSC based Tandem cells. Applications to hydrogen gas-sensors are described in detail.

Chapter 6 summarizes the work done as described in the earlier chapters. It briefly talks about all that has been learnt during and the application of that knowledge.

Chapter 2

Thin film synthesis using pulsed laser deposition: growth model

2.1 Introduction

Early uses of thin films focused mostly on electronic and optical devices with simple but high-quality architectures. In these applications it was important to have perfect surfaces for near-zero-resistance interconnection, and so monolithic films free of particles were necessary. The inevitable particle formation during PLD severely limited the use of the technique in the fabrication of such films. This caused a lot of the theoretical and practical advancements in the field to focus on trying to eliminate particles. Successful methods to obtain particle-free films included (a) deposition at laser powers below the threshold energy for particle formation (1), (b) mechanical shutters that use the difference in time when the atomic plasma and the particles reach the substrate(2; 3), (c) gas dynamic separation(4; 5), (d) using a molten target(6) among others.

Use of these techniques allowed PLD to be then used for thin film growth for high temperature superconductors(7; 8), epitaxial oxides on semiconductors(9; 10; 11), and tribological coatings(12). In more recent years PLD applications have included carbon nanotube(CNT)-assisted battery LiCoO2 electrode(13), ZnO nanocones for field emission properties(14), nanostructured SiC(15) and metamaterials(16).

However, as newer thin film applications have arisen, PLD has been embraced for what was earlier considered its drawback. For example gas sensors(17) and dye sensitized solar cells (DSSC)(18; 19), need high surface areas and the porous network of particles produced by laser ablation at high background pressures provides just that. During work with DSSCs (18; 19) it was observed that different morphological structures could be formed by deposition under different background pressures. It had already been suggested that controlling the morphology for such structures using PLD can be done using the ratio of the target to substrate distance to the plume length(20) as a guideline. However a growth model for the structure has not yet been proposed.

In order to understand the nanostructure growth mechanism I divide the effect of each pulse into three separate time regimes. The first is the short time scale that ranges from nanoseconds to a few hundred microseconds after the ablation (time scale in which the atomic and molecular species are dominant), the second is the medium time scale which is in the millisecond range (particle formation due to a single pulse) and continues till the next pulse hits the target. The longest time scale consists of particle interactions due to multiple trains of laser shots.

However, before I jump into describing a theoretical model for the nanostructured growth, it is necessary to give a brief overview of our PLD system.

2.2 Pulsed Laser Deposition: overview

Of the many physical vapor deposition techniques used for thin film growth, pulsed laser deposition (PLD), with its decoupling of the energy source for vaporizing materials and the vacuum hardware for the deposition chamber itself provides a unique flexibility in terms of deposition environments. The directionality of the laser itself in combination with mobile targets and optics may be used to obtain anything from simple single layered to complex multilayered films. This allows a single PLD system to operate practically

as an entire deposition laboratory by itself.

Further, in concept a pulsed laser deposition system is possibly the simplest thin film deposition system. It consists of a high power laser incident on a target that gets vaporized and is deposited on the substrate. However the actual system is a little more complex and looks more like figure 2.1.
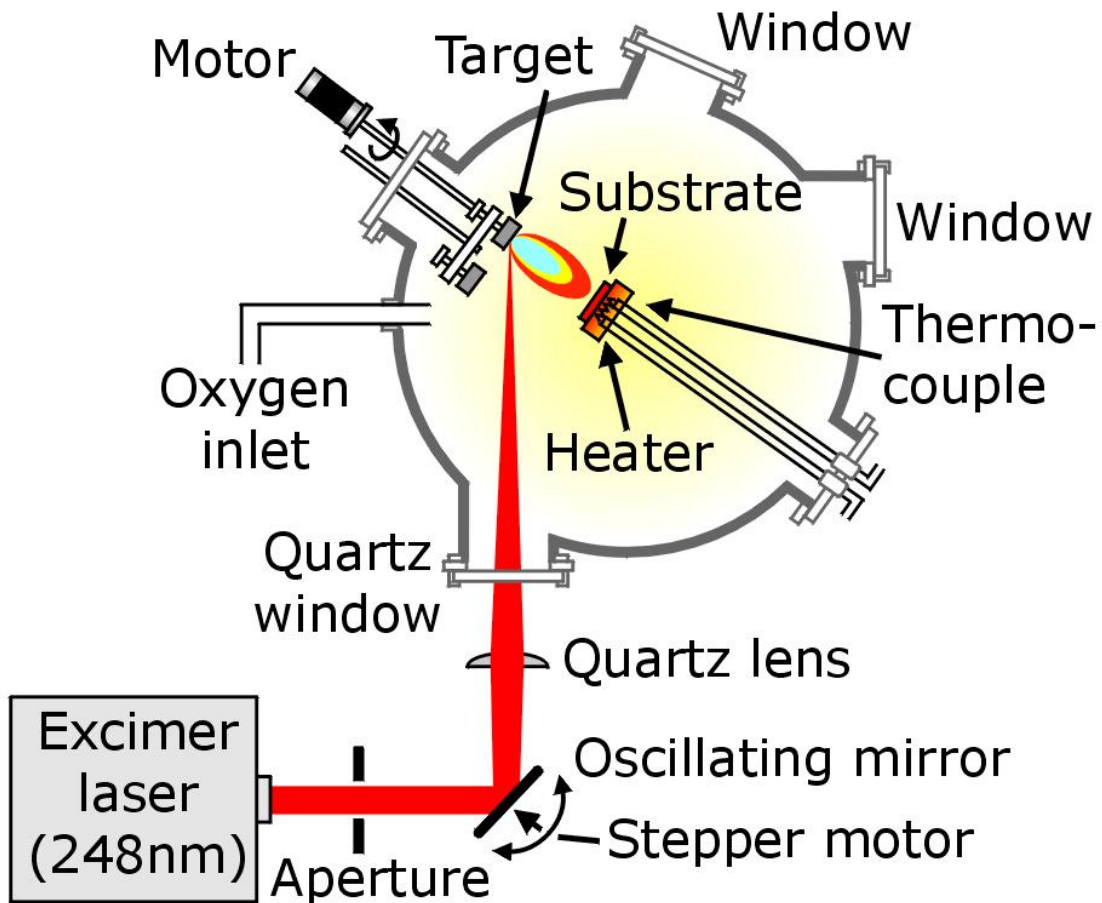
Figure 2.1: Schematic diagram of a PLD system

At the heart of the PLD system is an excimer laser. Our PLD is based on a KrF laser operating at $\lambda = 248$nm. The laser beam is made incident on a small area on the target, to ensure a large concentration of incident laser energy. This is done by a simple optical system shown in figure 2.2, that consists of a converging lens and a set

of mirrors. One of these mirrors is motorized to be able to rasterize the beam on the target.
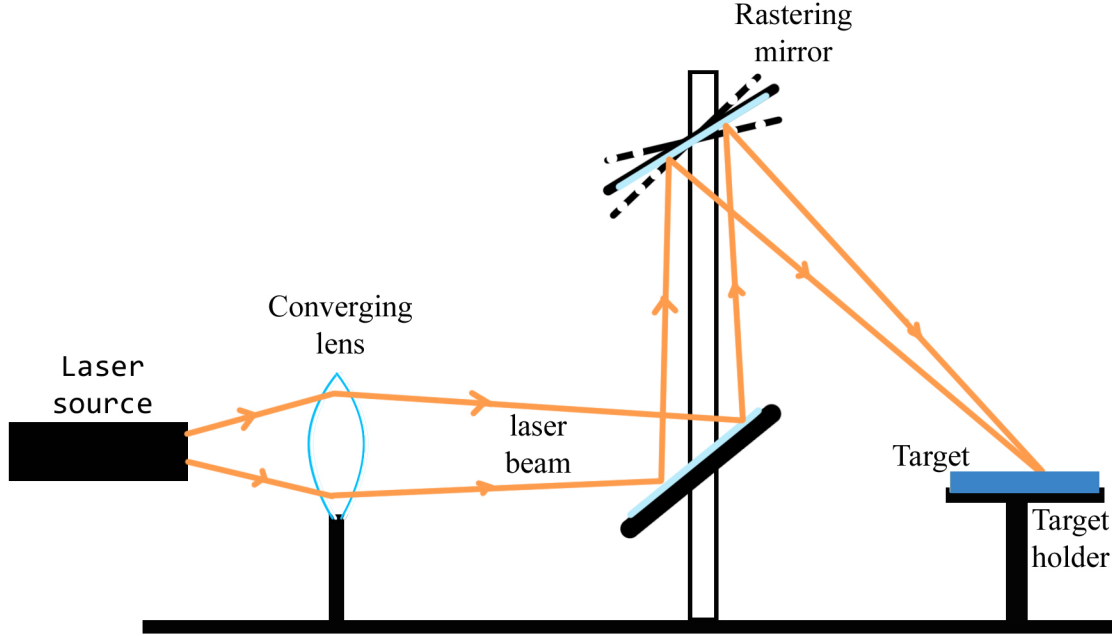
Figure 2.2: Optics used in our PLD system

In our system there is a moving carousel that can hold up to three targets at the same time. This is very helpful in obtaining layered structures. The substrate holder is placed directly over the target being irradiated. The substrate holder is mobile and is controlled by a motor that can raise the holder up or down. This is important, as I will show later in the chapter, because the target-substrate distance dictates film structure and morphology.

The target itself is usually in the form of a small solid disk. Besides the z-motion of the substrate each of the target holders as well as the substrate holder are capable of rotating. Together with the rastering of the beam over the target, this assures both a uniform film deposition over the substrate as well as uniform using up of the target.

As mentioned earlier, the main advantage of the PLD over the other conventional

physical deposition system lies in the decoupling of the vacuum hardware and the evaporation power source. This allows film deposition to occur in different reactive and non reactive environments, over a large range of pressures as well gas-types. The deposition occurs inside a chamber that is connected to a vacuum pump. After evacuation the chamber may be filled with a desired gas to a controlled pressure level. Gas pressure is monitored by pressure gauges while flow rates are controlled by flow meters.

Besides the variability in deposition environments and target to substrate distance our PLD system allows us to fabricate films over a larger parameter space that includes variables such as pulse energy, pulse rate, deposition temperature and the total number of pulses. The ability to set these parameters and have reproducible films over and over again is a big advantage compared to sol-gel methods traditionally used to fabricate porous thin films.

2.3   Short time scale description: plasma growth

In the very short time scale (≤ 200 μs) range the dominant effect is due to the plume dynamics with respect to the background gas. Wood *et al.*(21) with great detail came up with a model for the plume expansion into the background gas dependent on multiple scattering and hydrodynamical principles considering only on elastic collisions. According to them the plume is made up of plasma that consists of charged ions and neutral species of the ablated material that act identically as long as the plume growth is concerned. The high ionization energy of the background gas (oxygen in this case) ensures that the there are no charged species besides those from the target material. Together, this lends to the argument that the important collisions are those between the plume and the background gas and the kinetics and scattering processes due to the charged and neutral species are virtually the same.

In an earlier paper Geohegan *et al.* (22) further divide the short-time-scale plume

in the presence of a background gas into "fast" and "slow" components. The "fast" component is said to be from mostly the ionic species and is similar to that observed in vacuum, however the ground state and neutral species are slowed down in the presence of the background gas.

To experimentally observe the changes in plume dynamics, I photographed plume growth in the presence of background gas as a function of pulse energy, background gas pressure and target-to-substrate distance were observed. The experimental setup consisted of a cylindrical lens (f_L=5500 mm) focusing the apertured 248 nm beam from a Questek 2960 KrF-excimer laser (28 ns FWHM pulse width) to a horizontal line (2.0 cm^3 X 0.075 cm) on the face of a TiO$_2$ (99.99%) pellet at an incidence angle of 30°. Optical detection utilized a 1.33 m spectrometer (McPherson 209, 1800 g/mm holographic grating) outfitted with an intensified, gated diode array (Princeton Instruments IRY-700RB, 5 ns resolution) and photomultiplier tube (Hamamatsu R955). Fast unfiltered imaging was performed with a gated, (ICCD), lens-coupled camera system (Princeton Instruments) with variable gain, 200 to 820 nm response, and variable gating above 5 ns.

Figure 2.3 shows the luminescence from the plume observed for laser pulses with two different energies (pulse energy = 200 mJ and 300 mJ) in the presence of a background gas. At higher energies the plume travels faster and reaches a further "terminal distance" than the plume from lower energy pulse for the same target material traveling through the same background gas. At higher pulse energy ejected species from the target have larger momentum and kinetic energy. These are then expected to need a larger number of scattering events to be slowed down.

Similar trends are observed with change in background pressure. As shown in figure 2.4, at low pressures (vacuum and 30mTorr) the plume easily reaches the substrate in less than 10μs, but at 100mTorr it barely reaches the substrate in 50μs while at 300mTorr
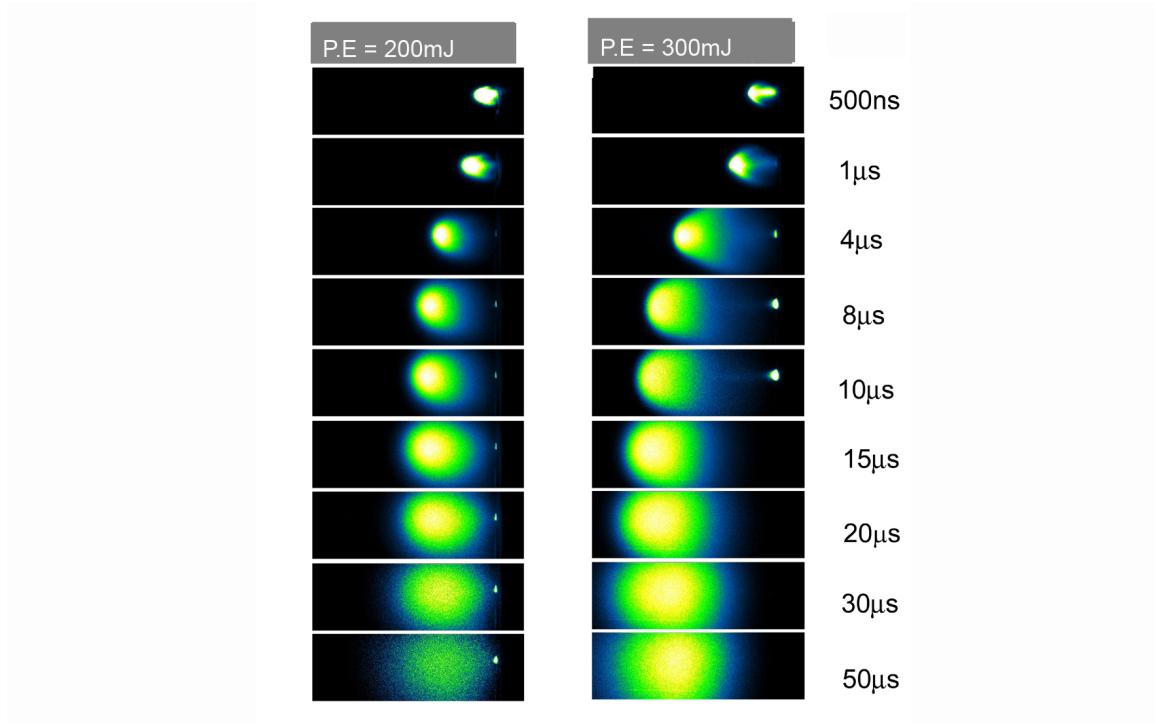
Figure 2.3: ICCD photographs of the visible plasma emissions at different times after KrF laser pulse with different pulse energies is incident on the TiO_2 target

the slowing down of the plume causes very little of the plume to be able to reach the substrate. Further slowing down of the species in the plume causes a larger concentration of the slow-moving species to continue to exist in the target-substrate distance. This may in turn lead to formation of particles due to inter-atomic collisions. At higher background gas pressures there is a larger number of background gas molecules, which in turn means that species in the plume undergo a larger number of scattering events.

Over a few hundreds of microseconds even for high-energy pulses in low background pressures the luminescence from the plume dies down. From this time to the time of the next pulse the slow-moving species that did not reach the substrate collide among themselves in the target-substrate distance and form particles that become the building blocks for the nanoparticulate films. Before I talk about the inter-particle and particle-gas molecule interactions let us take a look at what is already known of particle formation
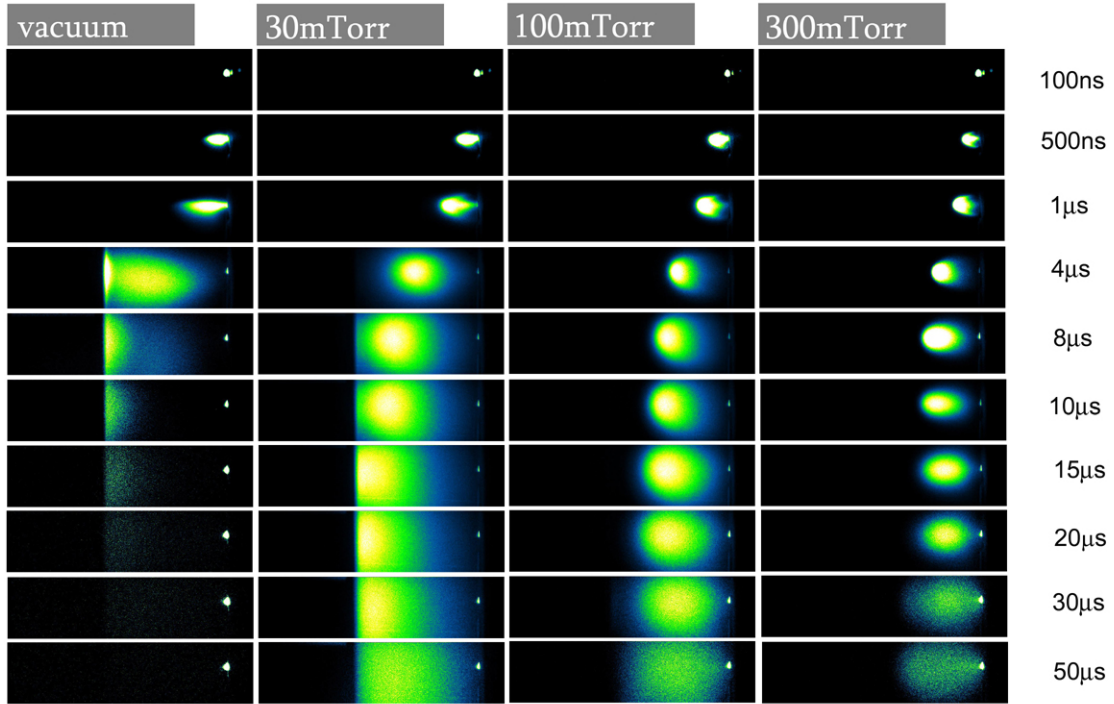
Figure 2.4: ICCD photographs of the visible plasma emissions in the presence of different background pressures of Oxygen at different times after KrF laser pulse is incident on the TiO_2 target

in a laser-ablated system.

2.4 Particle growth

Particulate formation during film growth was one of the main reasons impeding pulsed laser deposition from becoming more widely used as a thin film growth method. The combination of research leading to a greater understanding of the particulate growth as well as newer applications that require nanoparticle-based film structures have renewed interests in using laser ablation as a deposition method.

In order to understand film structures, it would be a good thing to start with how particles are affected by different laser parameters. Particles formed by laser ablation may be broadly categorized into three types. Each particle may be distinguished by

whether it originally started in the solid, liquid or vapor phase. Particles starting either in the solid or liquid phase are usually much larger, in the sub micron range, compared to vapor-phase particles which usually range from a few to tens of nanometers in size. Further, particles formed in the solid or liquid phase are usually irregularly shaped and do not travel very far from the target in the presence of background gases. The particles that originated in the vapor phase are only formed in high background gas pressure and are usually spherical. In our case the high background pressure as well as relatively large target-to-substrate distance allows us to neglect the particles formed outside the vapor phase for our simulations (to be presented later).

Particle size, number density and trajectories are dependent on a number of laser parameters. For a chosen target material and laser wavelength the most important parameter for variations in particulate characteristics is the laser fluence. The laser fluence may be controlled by either changes in the laser energy or changes in the laser spot size. It has been shown that no particles are formed below a threshold energy, and then the number of particles increases with laser energy until the number levels off(1). The leveling off at higher energies is due to saturation in the ablation process(23).

Background gas pressure is another laser parameter that needs to be studied in order to understand particulate formation during laser ablation. The use of background gases may be characterized as active or passive. Passive use is usually to compensate for deficiency in certain components. Metal oxides and have been shown to be oxygen deficient when laser deposition is done in high vacuum compared to when the films are grown in the presence of background oxygen(17). However the presence of background gases does much more than just stoichiometric correction as far as particulate growth is concerned. An increase in the background pressure causes an increased number of collisions between the vapor phase particles and the background gas molecules. This in turn decreases the mean free path of the particles as well as increases the number of

particle-particle collisions because the particles continue in the target-substrate region for a longer amount of time. Matsunawa *et al.*(24) have shown that with increased background pressure there is a larger variation of particle sizes with a shift of the distribution towards larger particles. They also showed a larger concentration of smaller particles closer to the substrate which supports the earlier argument.
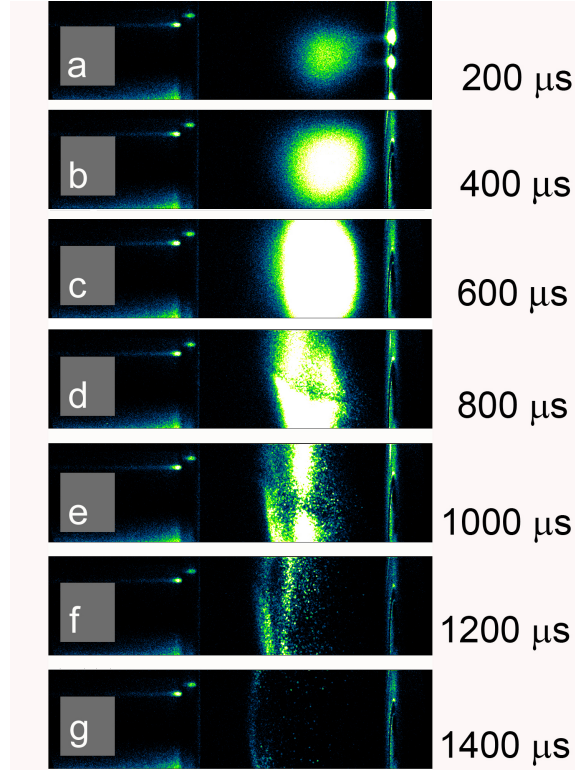
Figure 2.5: Particle formation and evolution due to a single laser pulse ablating target material.

The particle formation and motion in the target-substrate region is shown in figure 2.5. Initially particles are injected close to the substrate. These high-energy particles then expand into the cooler region that is occupied by the background gas. As they expand into this region they suffer collisions with the gas molecules as well as among themselves, which then slows down the expansion process. Inter-particle collisions are usually inelastic and cause larger particles to form. Particles which have suffered lesser

collisions are smaller and have conserved more of their forward momentum. This causes the smaller particles to move towards the substrate faster while the larger slow-moving particles form the tail. This may be the reason for the larger concentration of smaller particles closer to the substrate (24). Over a long period of time these particles will reach a terminal distance from the target. This is the distance at which the initial forward momentum that was imparted to the particles by the laser pulse is completely lost because of scattering events.

2.5   Multiple Pulse mode
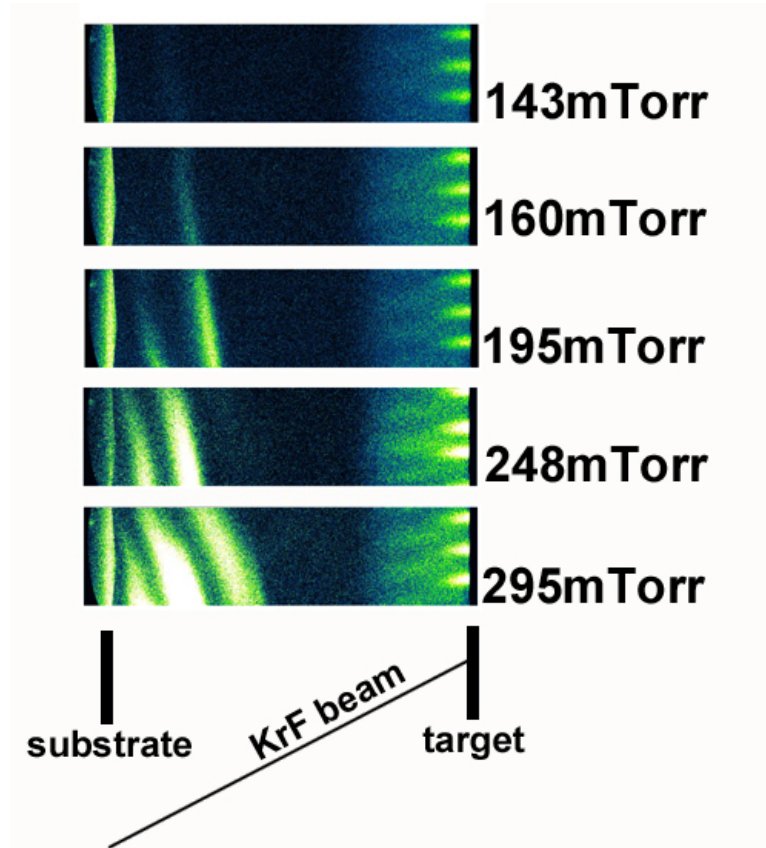
Figure 2.6: Inter-pulse particle interaction for PLD operating in "multiple pulse" mode. Visible differences can be noted for different background oxygen pressures.

In a PLD system there is a train of pulses time-separated from each other by the inverse of the pulse rate, each of which introduces new atomic, molecular and particle species in the target-substrate region. Particles formed from individual pulses continue to exist in the target-substrate distance over very long periods of times (seconds). This forces particles from subsequent pulses to interact with those from the previous ones. The amount of interaction will depend on deposition parameters like pulse energy and background gas pressure. For higher pulse energies, particles will need larger scattering events to lose all of their initial energy. This in turn means they travel faster and reach a greater distance from the target by the time the new species is introduced. This reduces the interaction between particles from different pulses. The effect of background pressure is the opposite. Increased background gas pressure translates to a larger number of collisions, which in turn means a faster slowing down of the particles. This forces a larger amount of interaction with particles from the subsequent pulses, as shown in figure 2.6.

2.6   Model

Computer models to study similar structures are common and include the diffusion-limited aggregation(25) and deposition diffusion aggregation(26). For this model I use a modified diffusion-limited aggregation approach. Before going on to explain the results obtained it is necessary to explain the basis of this model, the different parameters that I have used and what they represent in the physical sense, table 2.1.

For every laser pulse ablating the material a given number of particles <variable name = injection amount> is injected in the region between the target and the substrate. These particles move randomly with an initial overall preferred direction <variable name = y bias> towards the substrate. The number of injected particles as well as the initial momentum and kinetic energy is dependent on the incident pulse energy. As these
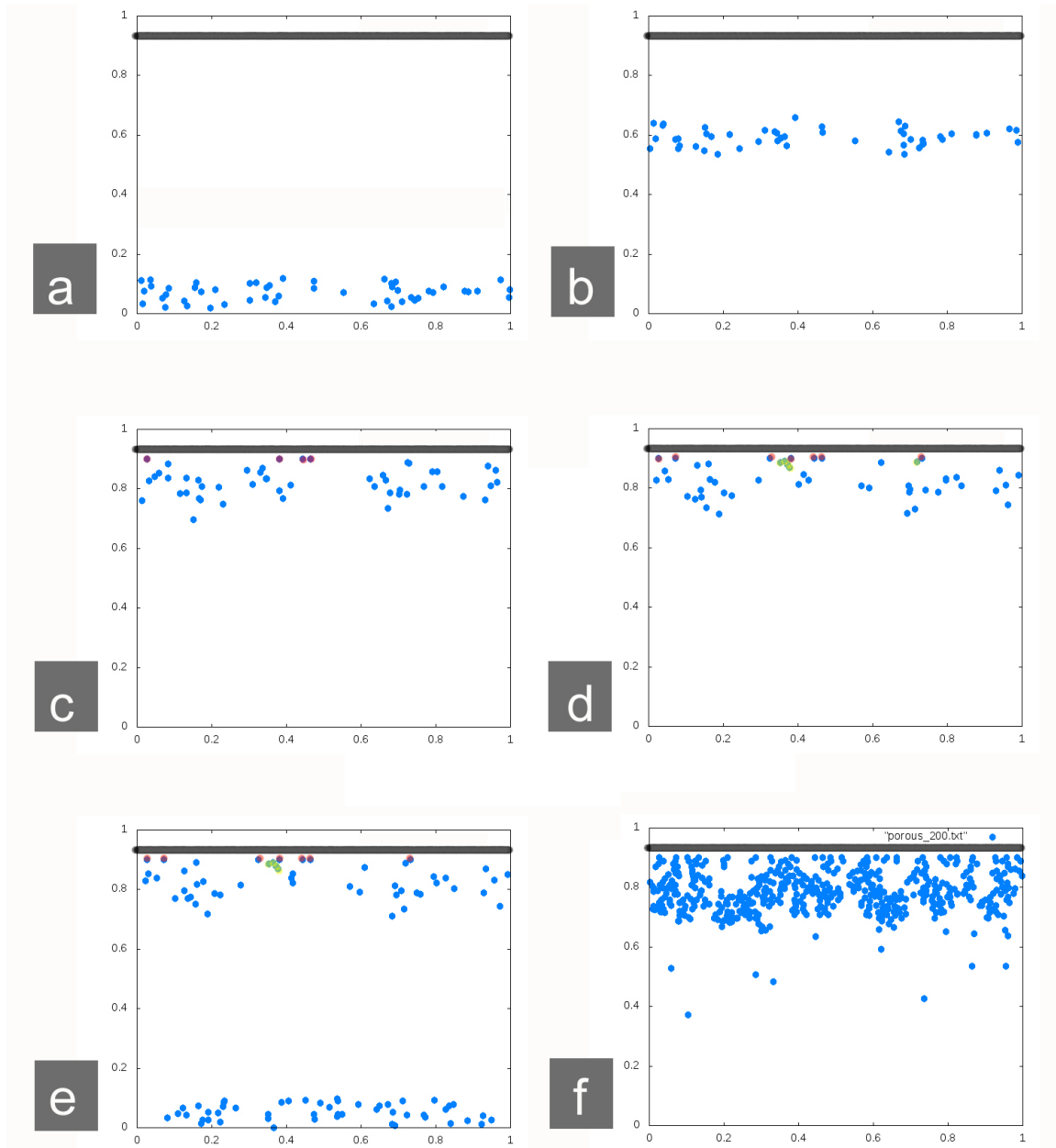
Figure 2.7: (a) Particles are injected in the target-substrate region. (b) Particles move towards the substrate through a modified random walk with a preferential direction along the positive y direction. (c) As the particles travel, they collide with gas molecules, causing the particles to lose energy. By the time they have approached the substrate, a significant portion of their initial energy might be lost. Particles that actually reach the substrate get immobilized (shown as red dots). (d) More particles land on the substrate giving rise to more seeds. Other particles with low-enough energy may collide with the seed particles and then get immobilized (shown as green dots). (e) New particles are injected in the target-substrate region because of a subsequent laser pulse ablating the target. (f) The final structure is obtained after multiple repetitions of steps (a)-(e).

particles undergo this motion they have a probability of colliding with the background gas molecules (which will depend on the background gas pressure). For every scattering event there is a loss of forward momentum <variable name = y bias depletion>. Once these mobile particles reach the substrate they become immobile <particles.mobile = true ⇒ particles.mobile = false> to form the first layer. This is not necessarily a uniform layer but more like seeds on the substrate. The subsequent particles may land on the bare substrate or on one of these seeds. Mobile particles that collide with immobile particles may or may not get stuck depending on the amount of energy (dependent on y_- bias that still remains in the particle after $y\_bias\_$ depletion) that they are incident with. If they collide with the stuck particle with energy greater than a threshold energy <variable name = threshold energy> they lose some energy, which depends on the material cohesiveness <variable name = stickiness> , and bounce back to their previous position and continue with their random motion. For lower-energy particles, striking a stuck particle causes them to get stuck <particles.mobile = true ⇒ particles.mobile = false>. Figure 2.7 depicts this sequence of steps.

2.7 Film Growth and Characterization

In order to compare our model to nanostructured PLD-films, I grew metal oxide films from the corresponding targets using a KrF excimer laser (248 nm) focused with a 60 degree incidence angle into the chamber and rastered over the target. The resulting plume was directed towards the substrate held above the target. Both the target and the substrate were continuously rotated at 40 rpm and 20 rpm, respectively, for uniform deposition. Prior to deposition, the PLD chamber was evacuated to a base pressure of 6 x 10 $^{-6}$ Torr. Variable parameters for the pulsed laser deposition system and the corresponding operating ranges are noted in table 2.2

Films made by varying these parameters are then observed using a scanning electron

microscope (SEM) or transmission electron microscope (TEM). Scanning electron microscope images are obtained using a Hitachi S-4700 operated at an accelerating voltage of 2 kV. Cross sectional images from SEM micrographs are obtained by cleaving the Si substrate and then using a L-mount. Transmission electron microscope images were obtained in the normal transmission (TEM) mode using JEOL 2010F-FasTEM using 200kV accelerating voltage. In order to obtain single nanostalks to be observed using TEM, films were scraped off the Si substrate and added to ethanol. These were then sonicated for 30 minutes and were then put on the TEM grid.

2.8   Comparing simulation to experimental results

2.8.1   Y-bias to pulse energy

To start off I modulate the "y-bias" parameter. The term "y-bias" may be considered as a misnomer as instead of a constant bias during the motion of the particles, this variable refers to the forward momentum the particles start with. This initial forward momentum is provided by the pulse energy. Therefore any change seen in the simulated structures obtained by changing "y-bias" should be similar to changes seen in experimental structures due to changes in laser pulse energy.

In these simulations every particle in the region will perform a modified random walk with a preferential direction. This directionality is provided by the "y-bias" (or forward momentum) parameter. Each particle starts of with a given "y-bias" which will dictate its subsequent motion. In figure 2.8 I show the effect of modulating "y-bias" in this model with all other parameters held constant and the corresponding structures obtained.

In the simulations which show structure progressions from lowest to highest y-bias, we can observe a very porous, spread out structure at lowest bias figure 2.8 (a) to a

Figure 2.8: Comparison of simulated and experimental structures. Simulated structures are obtained by changing "y-bias" parameter (lowest at (a) to highest at (d)). Simulations show trends of decreased porosity with increased "y-bias". In a physical sense "y-bias" corresponds to the pulse energy. Structures obtained by changing pulse energies (lowest at (a) to highest at (d)) show similar trends. Film parameters obtained from the simulations are plotted as a function of "y-bias".

very compact structure at highest bias (d). At y-bias values in between we see vertically aligned structures which look like trees. The experimental versions of these structures are obtained by changing the deposition parameter of pulse energy (shown in the second panel). The structures do show similar trends of increased porosity as shown in the simulated figures. There are however certain differences that can be explained in terms of experimental conditions. The range of pulse energies obtainable for our pulsed laser deposition system is relatively small (200 mJ to 300 mJ) and therefore does not allow us to explore the extreme film structures. Secondly from the scale bars it might be noted that thicker films are obtained at higher pulse energies opposite to that noted for simulations done at different y-biases. This is due to pulse energy influencing not only the y-bias but also the number of particles injected into the system from the target. Larger pulse energies introduces a larger number of particles which in turn causes thicker films. For the simulations, one of the parameters was changed at a time in order to isolate trends coming from individual parameters.

Increased pulse energy will cause a larger number of injected particles, which does not cause the structural geometry to change much besides making the films thicker as shown in the figure.

To quantify the results from simulations I introduce the terms seed number, average path length, porosity. In this code every immobile particle is given a path number. The path number is a measure of how far an immobile particle is from the substrate. The initial particles that land on the substrate have a path number zero, and are called seeds. The total number of particles with path number equal to zero is the seed number. Particles that land on these particles then have a path number 1, which is one higher than that of the particles they stuck to and this continues. The average path length from the outermost particles to the substrate is then the average path number. The definition of the porosity of the film is the ratio of the total empty space area up to the

film height to the area covered by the immobile particles.

2.8.2   Y-bias depletion to background gas pressure

Once the particle with a given initial "y-bias" has been injected in the target-substrate region it will start performing the modified random walk. However, for every step in the random walk it will lose part of its initial forward momentum because of the "y-bias depletion". In a physical sense this corresponds to what might be expected to occur in the presence of a background gas. During growth processes in the presence of an increased background gas pressure, particles will collide more with the gas molecules and will lose energy faster. This in turn means they will have less of their forward momentum remaining by the time they reach the substrate if they can get that far.

Similar to y-bias changes, the structure can also be modulated using y bias depletion. Figure 2.9 shows that at the lowest y-bias depletions the films obtained are very compact, and they become increasingly porous with increase in the value of this parameter with the possibility of obtaining vertically-aligned structures within a range of its values. In this case the number of injected particles is not affected by the parameter changed (background gas pressure). Our system also allows us to vary the range of background gas pressure from high vacuum to one atmosphere and this allows us to obtain structures that vary from extremely compact to highly porous as seen in figure 2.9. Further, the increased porosity also causes film thicknesses to be larger for films deposited at higher background gas pressures. A larger spreading of the structure from a single seed, as shown in figure 2.10, is also noted at higher background pressure. Simulations are shown to have similar trends.
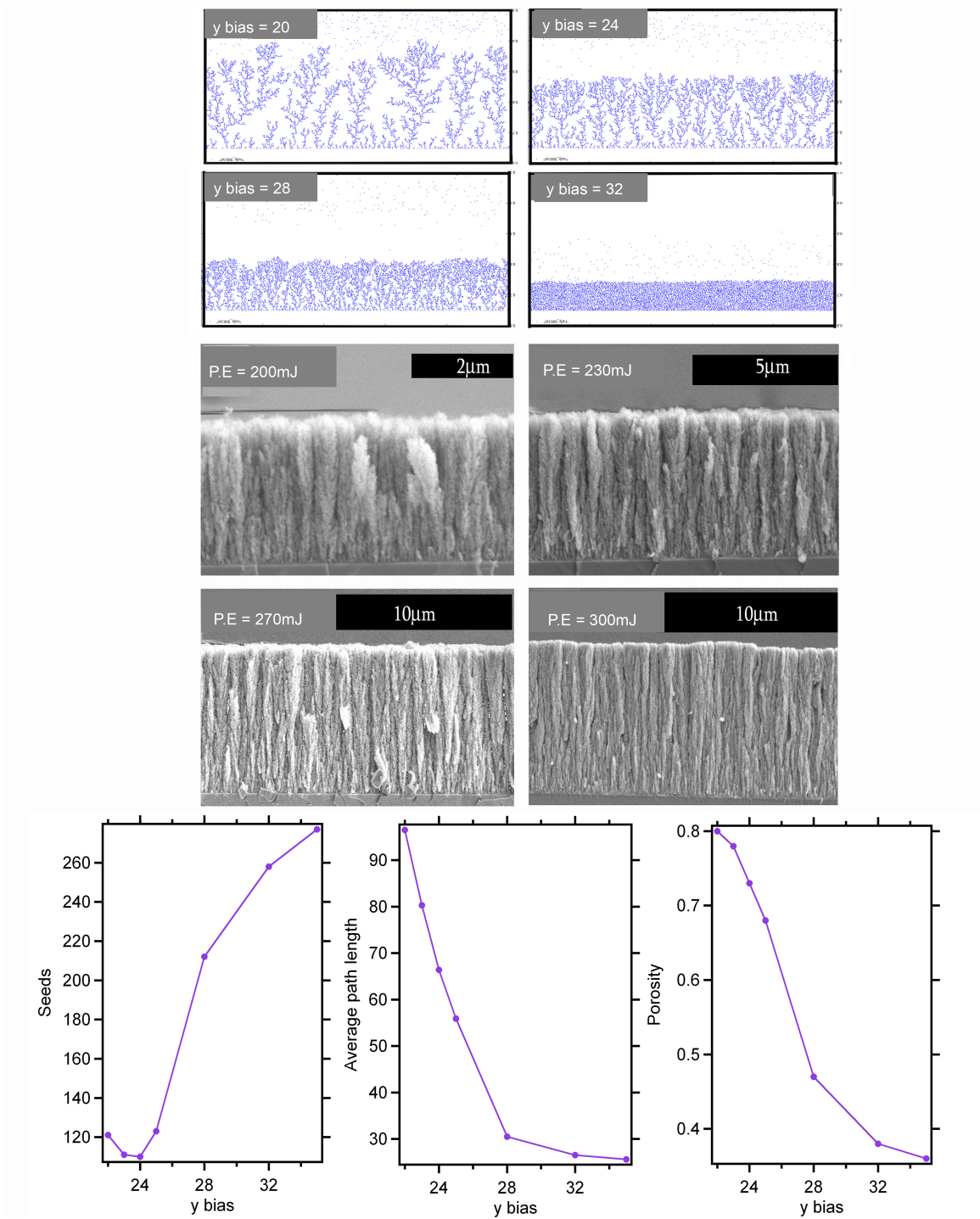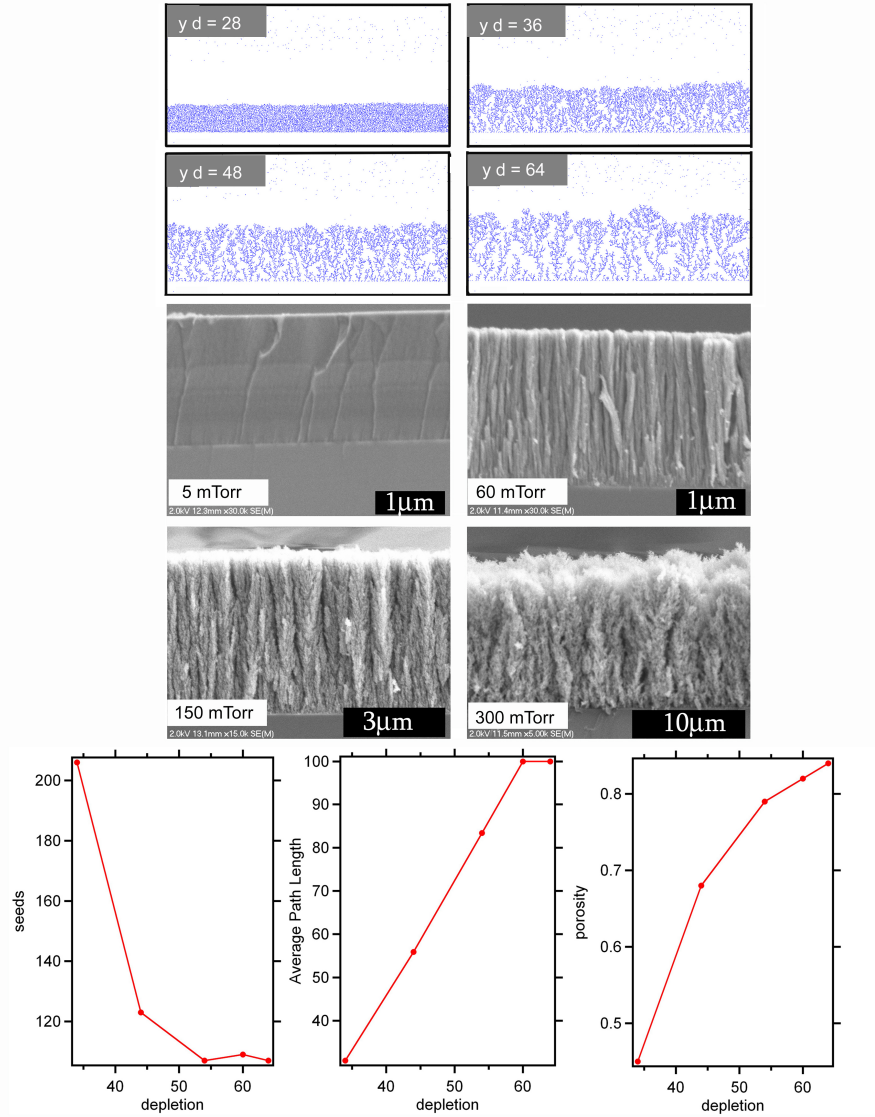
Figure 2.9: Comparison of simulated and experimental structures. Simulated structures are obtained by changing "y-bias depletion" parameter (lowest at (a) to highest at (d)). Simulations show trends of increased porosity with increased "y-bias depletion". In a physical sense "y-bias depletion" corresponds to the background gas pressure. Structures obtained by changing background gas pressure (lowest at (a) to highest at (d)) show similar trends. Film parameters obtained from the simulations are plotted as a function of "y-bias depletion" denoted as d.
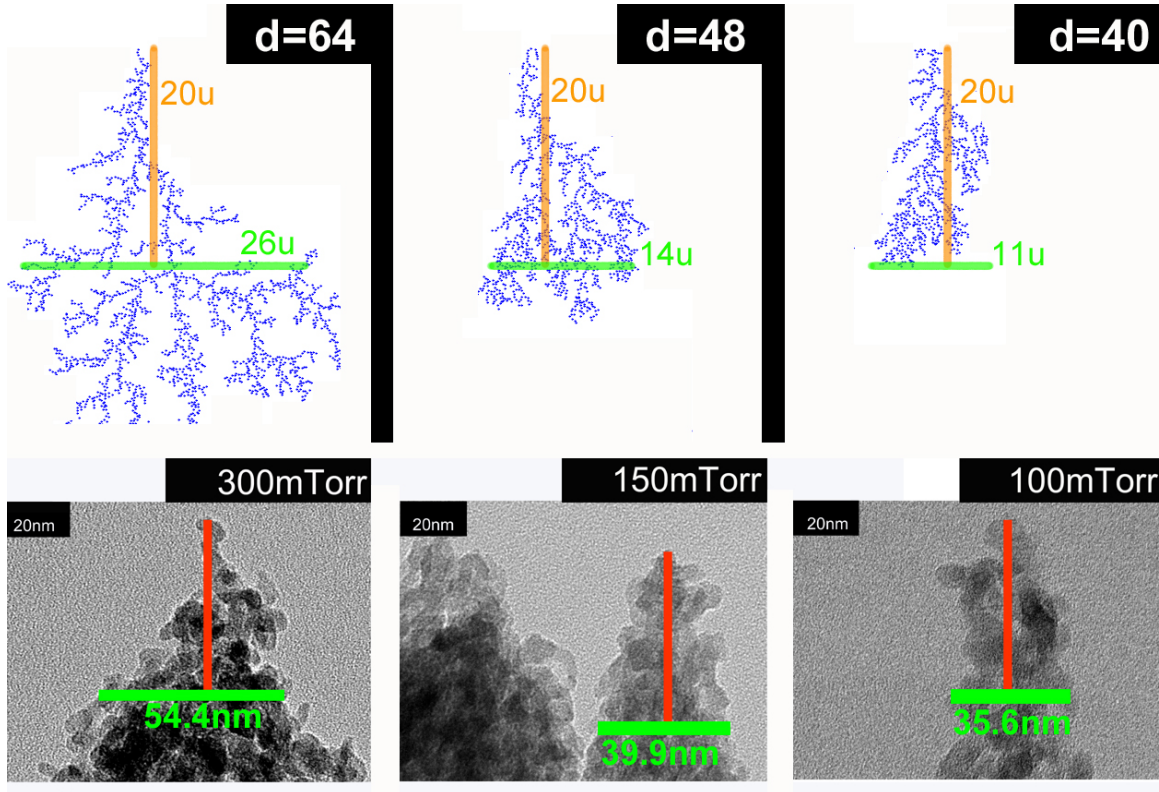
Figure 2.10: Comparison of spreading of structures. In the top panel is the simulated structures at different depletion settings (y-bias depletion = d). The spreading is compared by measuring the lateral dimension of the simulated structure 20 units away from the seed. In the panel below similar observations are made for structures fabricated at different background gas pressures. Lateral dimensions are measured for the fabricated structures at a distance of 50 nm from the seed.

2.8.3 Substrate height to target-to-substrate distance

Similar trends are also noted for different target-to-substrate distances as shown in figure 2.11. At smaller target-to-substrate distances the particles have more energy left when they arrive at the substrate due to the lower number of scattering events. This allows them to form a more compact structure because they do not get stuck to the other immobile particles immediately. Using a patterned substrate for this part also shows that the growth is perpendicular to the substrate. This lack of directionality of film deposition with respect to initial plume direction is understandable in terms of particles

lowest

lowest+24mm

lowest+12mm

lowest+38mm
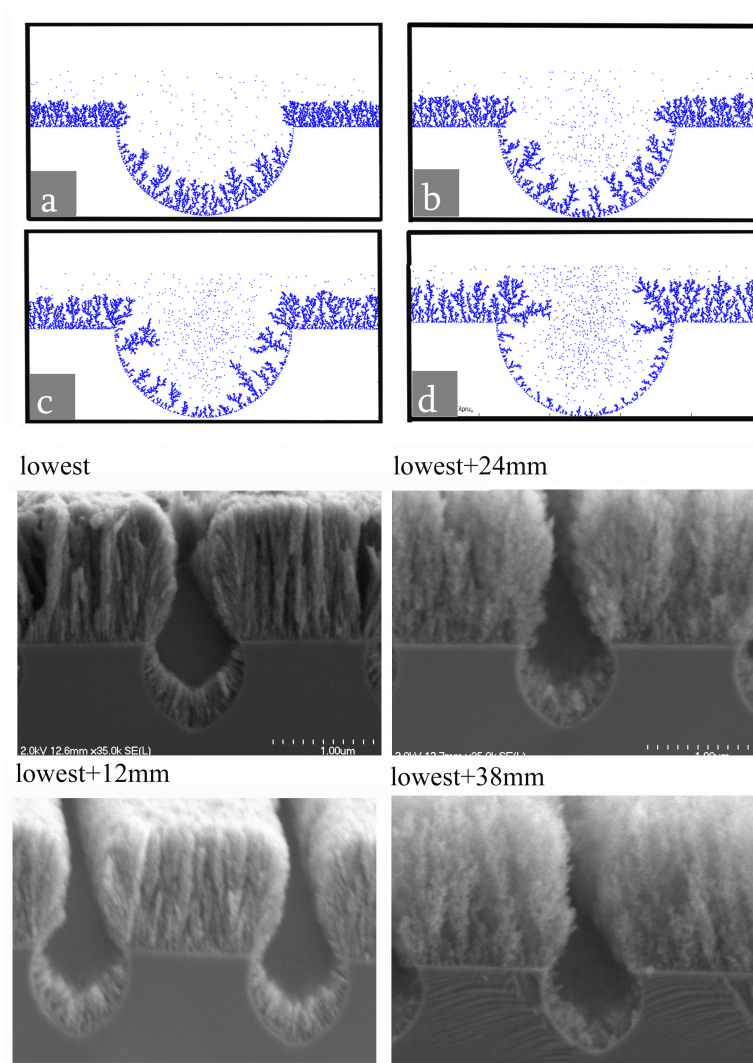
Figure 2.11: Comparison of simulated and experimental structures. Simulated structures are obtained by changing "substrate height" parameter (lowest at (a) to highest at (d)). Simulations show trends of increased porosity with increased "substrate height". In a physical sense "substrate" corresponds to the target-to-substrate distance. Structures obtained by changing this distance (lowest at (a) to highest at (d)) show similar trends. Further, using a patterned substrate allows us to see if the growth is dependent on the plume direction or the direction of the substrate surface. Growth perpendicular to the circular surface for both experimental and simulated structures confirms that the particles get stuck after the directionality due to the initial energy is lost.

becoming immobile only when they have lost enough forward momentum by means of

repeated scattering events.

2.8.4   Remaining parameters: number of pulses, pulse rate

Other externally-controllable parameters during deposition include the total number of laser pulses used and the pulse repetition rate. Neither of these parameters has much effect on the structural geometry. This is due to the fact that they do not control the directionality or energy with which the particles reach the substrate. Simulated structures obtained by changing "number of steps" and "injection period" confirm these assumptions.

2.9   Conclusions

Nanostructured films deposited using laser ablation have a unique structure that is due to the combined effect of plasma, single particles and the continuous collision of particles as they travel in the target to substrate region. The structures obtained vary from very compact thin films (grown predominantly by plasma deposition) to very porous thin films (in the presence of mostly particles). Somewhere in the regime between these extremes it is possible to get structures that resemble tree-like vertically aligned structures.

Parameters that affect the forward momentum of the particles when they reach the substrate will also affect the nanostructure of films deposited by pulsed laser deposition. The final forward momentum of the particles when they reach the substrate will depend on the initial forward momentum (from pulse energy), the amount of loss in forward momentum due to scattering (from background gas pressure) and the total number of scattering events (target to substrate distance). Particles reaching the substrate with low forward momentum form porous structures while those with larger forward momentum form compact structures.

This knowledge now allows us to tailor structures from a very compact structure to a porous open structure. Besides these extremes it is also possible to obtain vertically-

aligned structures. These vertically-aligned structures are especially useful in photo-voltaic applications in general and DSSCs in particular as will be theoretically explained in chapter 3 and experimentally verified in chapter 4.

Variable name	variable explained
number of particles	number of particles injected into the system initially.
number of steps	total number of scattering events being considered.
injection period	number of scattering events between injections (pulse rate)
injection amount	number of particles injected for each pulse (same as number of particles)
min radius	minimum particle radius
max radius	maximum particle radius
origin x, y min	particles are injected into a random region, close to target and move towards the substrate: minimum of this range in x,y-direction
origin x, y max	particles are injected into a random region, close to target and move towards the substrate: maximum of this range in x,y-direction
x step size	step size for random walk along x direction
y step size	step size for random walk along y direction
x bias	if any direction is preferred during random walk the bias along x direction can be controlled
y bias	the initial forward momentum to the particles. Physically controlled by pulse energy.
x bias depletion	for every scattering event there is a probability of collision that causes loss in directionality.
y bias depletion	for every scattering event there is a probability of collision that causes loss in directionality. In our model this initial directionality is due to pulse energy, which is depleted because of collisions with gas molecules
substrate height	target-substrate distance
threshold energy	the maximum energy a particle can have for it to be able to collide with a stationary particle and get stuck
material stickiness	amount of bias depletion on colliding with a stationary particle.

Table 2.1: Variables used in our code to simulate film growth and there explanation

Parameter	start	end
Pulse energy (mJ)	200	300
Pulse rate (hZ)	1	100
Background gas pressure (mTorr)	1×10^{-5}	1000
Background gas flow (sccm)	1	20
Target substrate distance (mm)	50	88

Table 2.2: The operating ranges for various parameters for the laser system

References

1. Blank, D., IJsselsteijn, R., Out, P., Kuiper, H., Floksura, J., and Rogalla, H. (1992) High Tc thin films prepared by laser ablation: Material distribution and droplet problem. <u>Materials Science and Engineering B(Switzerland)</u> 67–74

2. Barr, W. (1969) The production of low scattering dielectric mirrors using rotating vane particle filtration. <u>Journal of Physics E: Scientific Instruments</u> **2**, 1112

3. Dubowski, J. (1986) Epitaxial growth of thin semiconductor films by pulsed laser evaporation, damage and vaporation of CdTe and InSb targets induced with Nd: YAG laser. In <u>Proc. Soc. Photo-Opt. Instrum. Eng.</u>, volume 668, 97

4. Gaponov, S., Gudkov, A., Luskin, B., Luchin, V., and Salashchenko, N. (1981) Formation of semiconductor films from a laser erosion plasma scattered by a heated screen. <u>Soviet Physics-Technical Physics</u> **26**, 598–600

5. Kennedy, R. (1992) A new laser ablation geometry for the production of smooth thin single-layer YBa2Cu3O7-x and multilayer YBa2Cu3O7-x/PrBa2Cu3O7-x films. <u>Thin Solid Films</u> **214**, 223–228

6. Cheung, J. and Sankur, H. (1988) Growth of thin films by laser-induced evaporation. <u>Critical Reviews in Solid State and Material Sciences</u> **15**, 63–109

7. Dijkkamp, D., Venkatesan, T., Wu, X., Shaheen, S., Jisrawi, N., Min-Lee, Y., McLean, W., and Croft, M. (1987) Preparation of Y-Ba-Cu oxide superconductor thin films using pulsed laser evaporation from high Tc bulk material. <u>Applied Physics Letters</u> **51**, 619–621

8. Wu, X., Dijkkamp, D., Ogale, S., Inam, A., Chase, E., Miceli, P., Chang, C., Tarascon, J., and Venkatesan, T. (1987) Epitaxial ordering of oxide superconductor thin films on (100) SrTiO3 prepared by pulsed laser evaporation. <u>Applied physics letters</u> **51**, 861–863

9. Fork, D., Fenner, D., Connell, G., Phillips, J., and Geballe, T. (1990) Epitaxial yttria-stabilized zirconia on hydrogen-terminated si by pulsed laser deposition. <u>Applied physics letters</u> **57**, 1137–1139

10. Fork, D., Fenner, D., Barton, R., Phillips, J., Connell, G., Boyce, J., and Geballe, T. (1990) High critical currents in strained epitaxial YBa2Cu3O7-δ on si. Applied Physics Letters **57**, 1161–1163

11. Fork, D., Ponce, F., Tramontana, J., and Geballe, T. (1991) Epitaxial MgO on Si (001) for Y-Ba-Cu-O thin-film growth by pulsed laser deposition. Applied physics letters **58**, 2294–2296

12. Auciello, O., Barnes, T., Chevacharoenkul, S., Schreiner, A., and McGuire, G. (1989) Laser ablation deposition of titanium nitride films on silicon substrates at room temperature. Thin Solid Films **181**, 65–73

13. Lo, A., Sun, C., Tseng, W., and Kuo, C. (2009) Process and properties of the carbon nanotube assisted LiCoO thin-film battery electrode by pulsed laser deposition. Journal of Vacuum Science & Technology B: Microelectronics and Nanometer Structures **27**, 3067

14. Bae, J., Hong, J., Han, W., Choi, Y., and Snyder, R. (2009) Superior field emission properties of ZnO nanocones synthesized by pulsed laser deposition. Chemical physics letters **475**, 260–263

15. Zhang, H., Feng, P., Makarov, V., Weiner, B., and Morell, G. (2009) Synthesis of nanostructured SiC using the pulsed laser deposition technique. Materials Research Bulletin **44**, 184–188

16. Ray, E., Hampton, M., and Lopez, R. (2009) Simple demonstration of visible evanescent-wave enhancement with far-field detection. Optics letters **34**, 2048–2050

17. Ghosh, R., Baker, M., and Lopez, R. (2010) Optical properties and aging of gasochromic WO3. Thin Solid Films **518**, 2247–2249

18. Sauvage, F., Di Fonzo, F., Li Bassi, A., Casari, C., Russo, V., Divitini, G., Ducati, C., Bottani, C., Comte, P., and Graetzel, M. (2010) Hierarchical TiO2 photoanode for dye-sensitized solar cells. Nano letters

19. Ghosh, R., Brennaman, M., Uher, T., Ok, M., Samulski, E., Mcneil, L., Meyer, T., and Lopez, R. (2011) Nanoforest Nb2O5 photoanodes for dye sensitized solar cells by pulsed laser deposition. ACS Applied Materials & Interfaces

20. Bailini, A., Di Fonzo, F., Fusi, M., Casari, C., Bassi, A., Russo, V., Baserga, A., and Bottani, C. (2007) Pulsed laser deposition of tungsten and tungsten oxide thin films with tailored structure at the nano-and mesoscale. Applied surface science **253**, 8130–8135

21. Wood, R., Chen, K., Leboeuf, J., Puretzky, A., and Geohegan, D. (1997) Dynamics of plume propagation and splitting during pulsed-laser ablation. Physical review letters **79**, 1571–1574

22. Leboeuf, J., Chen, K., Donato, J., Geohegan, D., Liu, C., Puretzky, A., and Wood, R. (1996) Modeling of dynamical processes in laser ablation. Applied surface science **96**, 14–23

23. Smith, G., Chen, L., and Chuang, M. (1992) Effects of processing parameters on KrF excimer laser ablation deposited ZrO films. In Materials Research Society Symposium Proceedings, volume 235, 843–848

24. Matsunawa, A., Katayama, S., Susuki, A., and Ariyasu, T. (1986) Laser production of metallic ultra-fine particles. Trans. JWRI **15**, 233–244

25. Witten Jr, T. and Sander, L. (1981) Diffusion-limited aggregation, a kinetic critical phenomenon. Physical Review Letters **47**, 1400–1403

26. Jensen, P., Barabási, A., Larralde, H., Havlin, S., and Stanley, H. (1994) Deposition, diffusion, and aggregation of atoms on surfaces: A model for nanostructure growth. Physical Review B **50**, 15316

Chapter 3

Dye Sensitized Solar Cells: Overview of methods, materials and analysis techniques

3.1 Introduction

One of the grand challenges for the human race is to be able to keep up with the constantly growing energy needs of our species, while at the same time ensuring that we protect our environment. In order to be to able to achieve this goal there is an immediate need for us to shift from our dependence on fossil fuel. The obvious choice is to move to an energy source that is inexhaustible and clean at the same time. The Sun with its proven track record of providing enough energy to run all natural processes on our planet throughout its existence is an excellent candidate. However, in order to tap into this source we need to find a way to harness this energy. Although there already exists techniques and products to do this, there still exists certain difficulties that have stood in the way of solar energy overtaking or even making a significant dent in this fossil fuel driven world.

Current techniques to tap the Sun's inexhaustible energy source to produce electricity may be roughly divided into four categories: (a) Multijunction solar cells, (b) crystalline Si cells, (c) thin film solar cells and (d) emerging organic/ hybrid photovoltaics. As is

Best Research-Cell Efficiencies
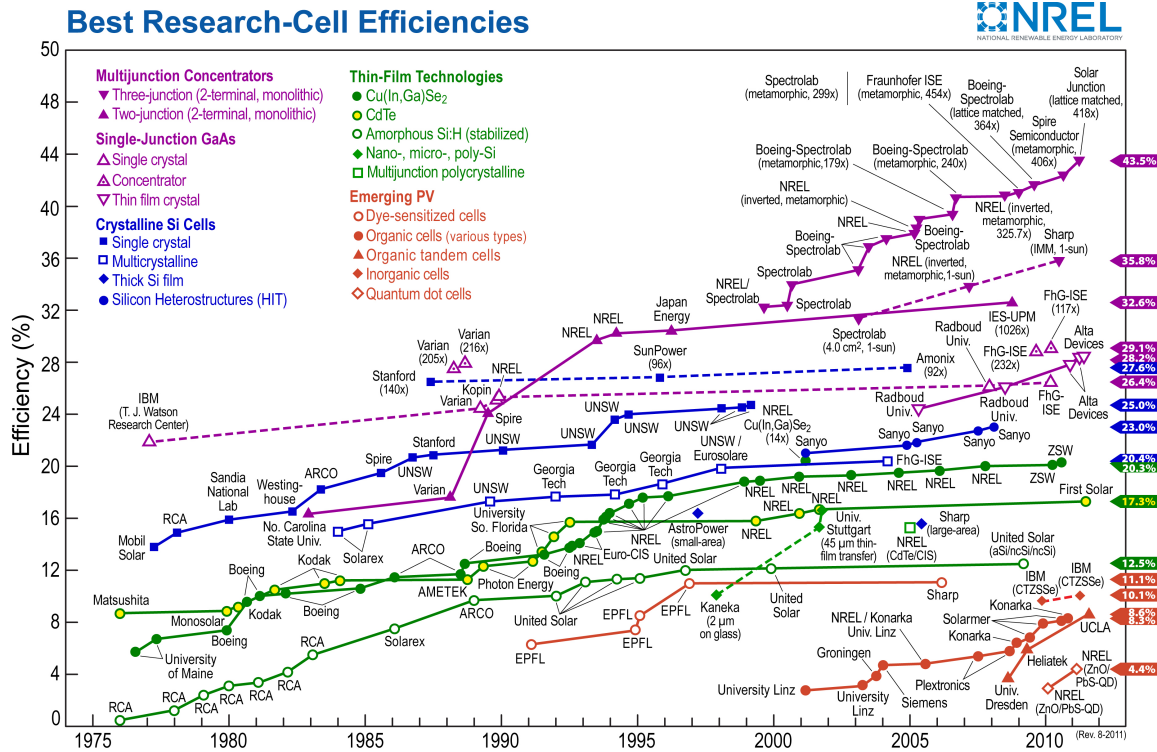
Figure 3.1: Efficiency of different solar techniques and their evolution over the years.

obvious from figure 3.1 the battle for efficiency is being won by multijunction concentrators followed by c-Si and thin film based techniques. However, in order for solar energy to be able to become competitive overall, efficiency is not the only parameter that needs to be optimized. The biggest hurdles in the path of the above-mentioned techniques in replacing fossil fuels remain the high costs and highly energy-consumptive methods of preparation. Additionally certain widely-used materials for these techniques are not only toxic (e.g. CdTe) but are also not overly abundant.

On the other hand although emerging photovoltaics do not boast the high efficiencies of the other techniques, they do provide the advantages of being inexpensive, easy to fabricate and being made of materials that are relatively abundant. Of the various devices that are included in this field, the highest efficiencies have been recorded for dye sensitized solar cells (DSSC).

Although the idea of sensitizing photoelectrodes itself is not new, (1) being able to use it as a viable solar cell was only demonstrated in 1991 by Brian O'Regan and Michael Grätzel(2). Since then there has been a great amount of research in the field which has seen an improvement of over all power conversion efficiency increase from 7% to its current value of around 13% (3).

3.2   Working principles of a DSSC

Despite the great amount of research in optimizing different parameters, the extremely simple architecture of DSSCs has remained pretty much unchanged since 1991. A DSSC consists of the following components: (a) a glass substrate for support, (b) a transparent conducting oxide (TCO) on the substrate, (c) a semiconductor film, (d) sensitizer dye adsorbed on the semiconductor film, (e) an electrolyte with a redox mediator, and (f) a counter electrode that can regenerate the redox mediator. The layout of the different components in a typical DSSC is shown in figure 3.2 (a). Figure 3.2 (b) shows the different energy levels that dictate the photophysical behaviour of the cell.
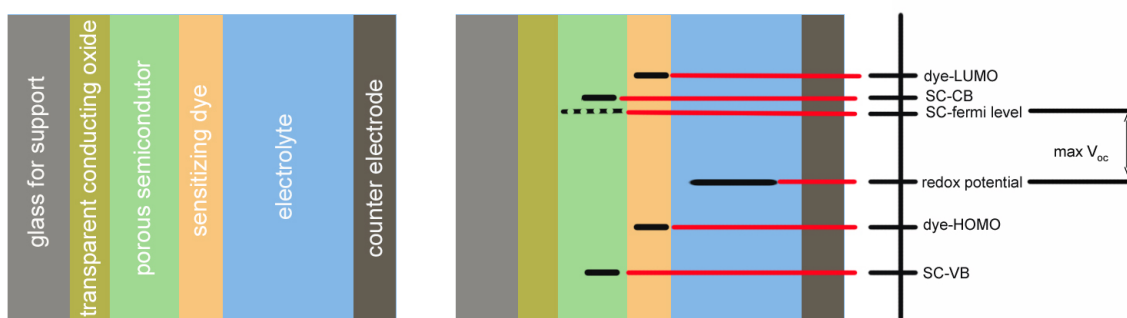
Figure 3.2: (a) Schematic diagram showing different parts of a DSSC, (b) Energy levels for the different parts of s DSSC

The photovoltaic process responsible for the functioning of the DSSC occurs at the interface of the semiconductor anchored dye and the electrolyte. Once the light is ab-

sorbed by the dye, it excites an electron from its highest occupied molecular orbital (HOMO) level to its lowest unoccupied molecular orbital (LUMO) level, thus oxidizing the dye. This is quickly followed by the injection of the excited electron into the conduction band (CB) of the semiconductor. The dye itself is brought back to its normal state by gaining an electron from the redox electrolyte. The injected electron is transported through the semiconductor to the TCO by doing an amount of work equal to the energy difference between the CB of the semiconductor and the redox potential of the electrolyte.
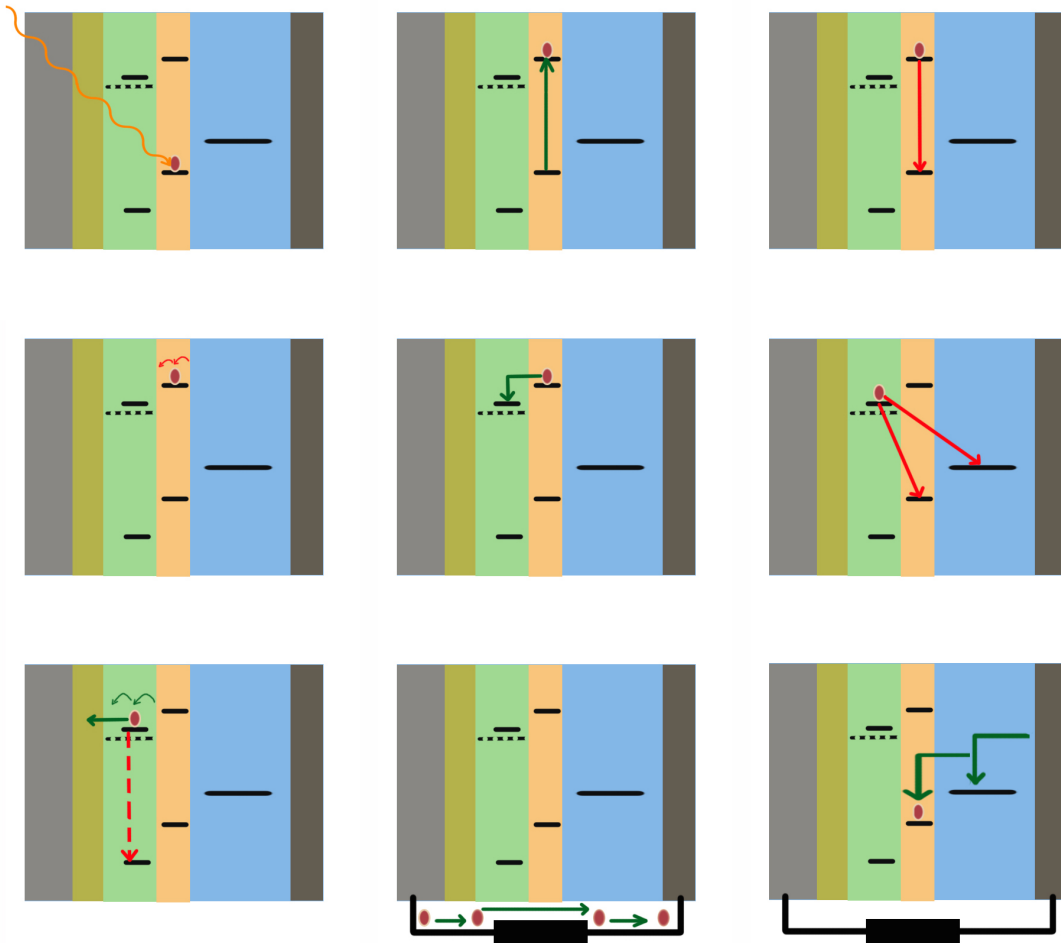
Figure 3.3: A stepwise description of the working of a DSSC

In principle the functioning of a DSSC maybe divided into eight distinct processes (4) shown in figure 3.3.

1. Photon absorption and excitation: Light is absorbed by the dye. This is dictated by the absorption window, the light intensity in that window and the absorption coefficient (α) of the dye. The absorbed energy from this light excites electrons from the HOMO level to the LUMO level of the dye. figure 3.3 (a)

2. Radiative recombination: Direct relaxation of the dye back to its ground state in which the excited electron loses its energy by some radiative process and goes back to the HOMO from the LUMO level. figure 3.2 (d) This usually has a time scale in the nanosecond regime. Rate constant = k_2

3. Exciton diffusion: The excited electrons may then jump from the LUMO level of one dye molecule to another. figure 3.2 (e). This may be reduced by ensuring only uniform monolayer coverage.

4. Interfacial charge transfer: Excited electrons from the dye-LUMO are injected into the semiconductor-CB. figure 3.2 (f). For an efficient DSSC this should happen in a picosecond time scale. Rate constant = k_4

5. Electron back transfer: Excited electrons from the semiconductor-CB may be captured by the oxidized species of the electrolyte. figure 3.2 (g). Rate constant = k_5

6. Interfacial charge recombination: Excited electrons from semiconductor-CB may get captured by the oxidized dye molecules. figure 3.2 (h). Rate constant = k_6

7. Electron transport: The excited electrons travel through the network of semiconductor particles. figure 3.2 (i). This electron transfer from particle to particle happens through a series of trapping and de-trapping steps. Some of the electrons

may also be lost to the lower-energy states of the semiconductor by non-radiative processes like phonon relaxation.

8. Electrolyte to dye electron transfer: Electrons from the electrolyte constantly replenish the dye-HOMO level, figure 3.2 (j).

The main driving force for the efficient working of a DSSC is the very fast interfacial charge transfer. When the electron is in the dye-LUMO, of the two processes that are possible, (2) and (4) from above, the rate constants ($k_4/k_2 \sim 1000$) overwhelmingly favors charge injection. Once they have been injected into the semiconductor CB, rate constants ($k_5/k_6 \sim 100$) favor electrons being lost to the electrolyte over being lost to the dye. In light of these rate constants the steps (2) and (6) may be ignored for most optimized systems(4).

3.3 Quantitative understanding of effects of different variables

In order to have a very basic understanding of the effects of the different parameters on the functioning of a dye sensitized solar cell we use a mathematical model based on the work of Wurfel(5). The code used for the simulation can be downloaded from www.physics.unc.edu\$\sim$rudresh\dssccode.nb.

The first parameter we vary is the position of the conduction band (E_{cb}) of the photoanode. Since I^-/ I^{3-} is the redox couple predominantly used for these systems we keep that constant. In keeping with this convention we fix the I^-/ I^{3-} redox level at -4.95 eV. E_{cb} is varied from -4.0 eV to -4.9 eV. From the I-V curves obtained (shown in figure) it can be noted that the only effect the change in E_{cb} has is that of changing the V_{oc}. This is understandable because the change in E_{cb} changes only the position of the quasi-Fermi level in the lit state inside the photoanode material. Once electrons have

37

been injected to this E_{cb} the transfer and collection of those electrons is independent of this energy level.
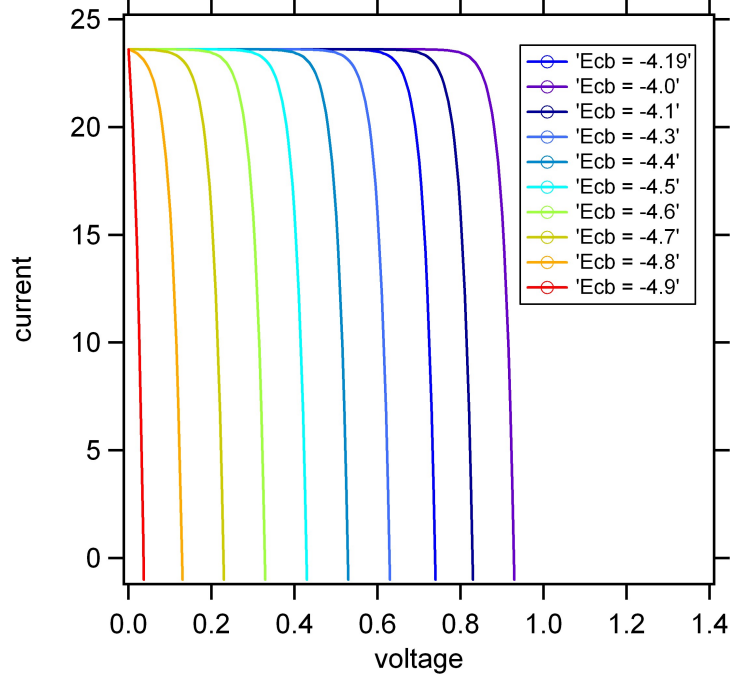
Figure 3.4: IV curves for different positions of conduction band edge, E_{cb}, of materials used as photoanaodes.

Once we know that electrons can be injected into E_{cb}, we can think of the other possibilities. The next step is to know how electron concentration in the E_{cb} affects device behavior. The electron concentration in E_{cb} will depend on the injection efficiency of the molecules and the total number of electrons in the LUMO of the dye. This will in turn depend on the absorption coefficient of the dye and the light intensity. For our simulations we consider only one light intensity and unity light efficiency (similar to what is expected for TiO_2 based dye sensitized solar cells). We consider all the other steps using a single parameter α in our simulations.

From the IV curves we see that unlike the changes caused by changes in E_{cb}, changes in α cause shifts both in V_{oc} and I_{sc}. This maybe explained by the fact that with an increase in α we have an increase in the electron concentration in the conduction band
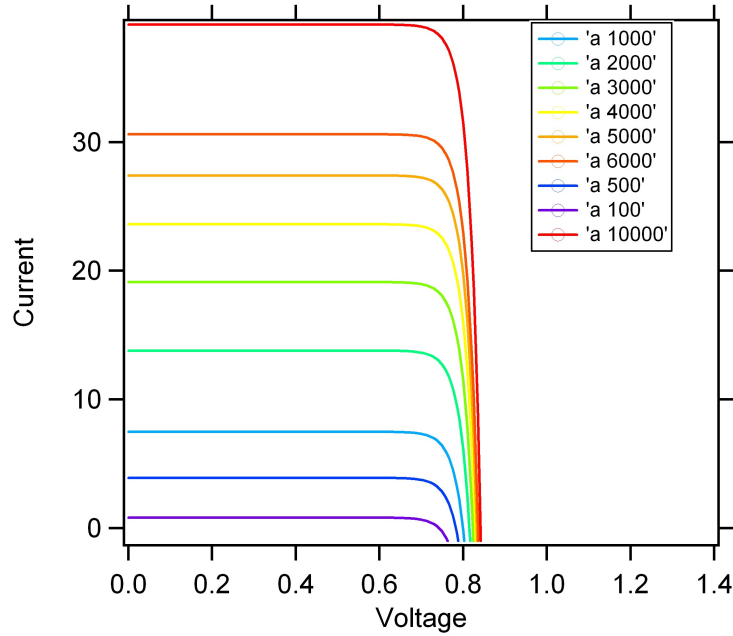
Figure 3.5: IV curves for different values of α.

of the photoanode. This increase in electron concentration pulls the Fermi level upward and therefore is observed as an increased V_{oc}. The increased conduction band electrons are also observed as a larger photocurrent.

The trends of V_{oc} and I_{sc} shown in the graphs also reiterate this. Initially with an increase in α there is a large change in the position of the quasi-Fermi level (and therefore the V_{oc}) but as the quasi Fermi level gets closer and closer to the position of E_{cb}, the value of V_{oc} saturates off. A similar trend, though slower, is seen for I_{sc}. Initially with an increase in α there is a larger increase in the number of photo-generated electrons. However once the system has absorbed all the light there is no further increase in the number of photo-generated electrons.

The electrons in the conduction band may either recombine with the electrolyte with a rate constant K_{rcb} or diffuse through the photoanode with a diffusion coefficient D_{cb}. The IV curves due to changes in K_{rcb} are shown in the figure. Like changes in α, changes in K_{rcb} cause shifts in I_{sc} as well as in V_{oc}. Below a threshold K_{rcb} value all the

electrons can go through the photoanode and reach the conductive substrate. Lowering K_{rcb} further does not cause any increase in I_{sc}. However the lower K_{rcb} in this regime causes the electrons to populate the conduction band for longer, causing a positive shift in E_{cb} and therefore a higher V_{oc}.

At higher K_{rcb} electrons are lost faster and not all the photo-generated electrons can reach the conductive substrate. This is observed as a lower I_{sc}. In order for improved device performance K_{rcb} needs to be reduced.
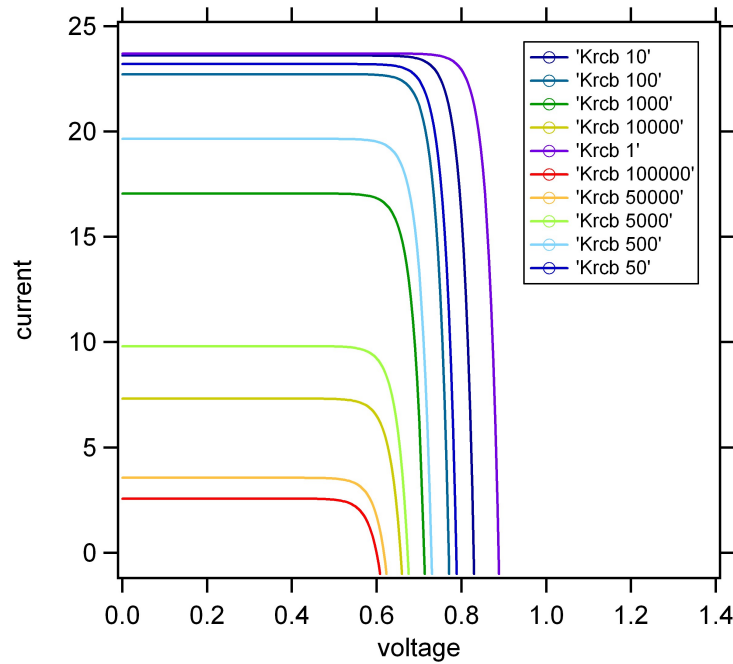
Figure 3.6: IV curves for different recombination rates, K_{rcb}, for materials used as photo anodes.

The diffusion coefficient D_{cb} does not cause any changes in V_{oc}. However it does cause a rapid drop in I_{sc} at corresponding diffusion lengths smaller than the film thickness. At diffusion length values comparable to and larger than the film thickness all electrons can pass through and therefore no further changes in photocurrent are observed.

Change in film thicknesses has two possible effects. Increase in thickness causes a larger amount of dye loading which means a larger light absorption which translates to a
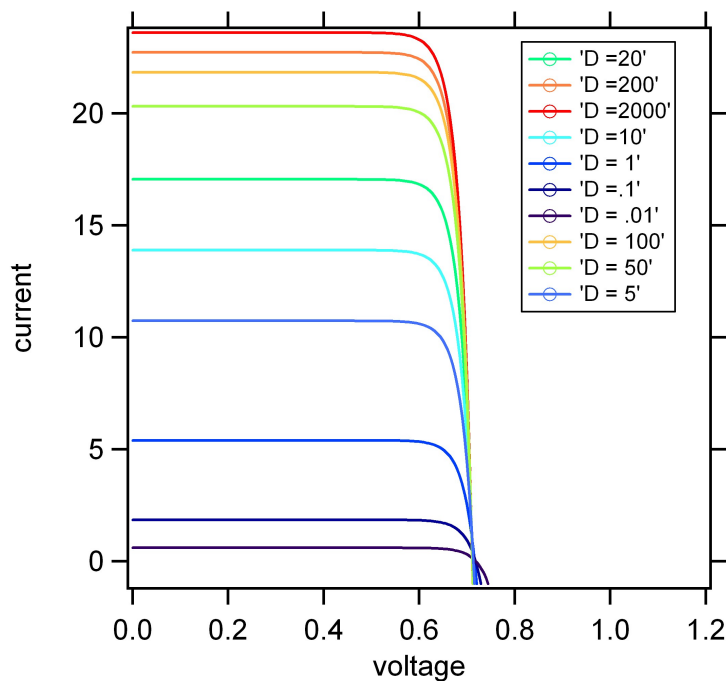
Figure 3.7: IV curve as diffusion coefficients, D_{cb}, is varied

larger number of photo-generated electrons. However with a very thick film there is also a larger amount of electrons lost due to recombination. This shows up as a saturation in the photocurrent at a given film thickness with no gains by making it any thicker.

For an optimized device, a high V_{oc} and high I_{sc} are desired. This may be obtained for a photoanode with high conduction band (lower than the LUMO of the dye), high light absorption (controlled by the absorption coefficient of the dye as well as the amount of dye loading), low recombination rate, high diffusion constant, a thickness optimized for efficient light absorption and an overall device architecture that lowers resistive losses. In the next section I describe how these choices are made.

3.4 Choice of materials

In the last section I discussed the rationale for choosing certain properties for an efficient device. In this section I talk about the commonly-chosen materials and how further
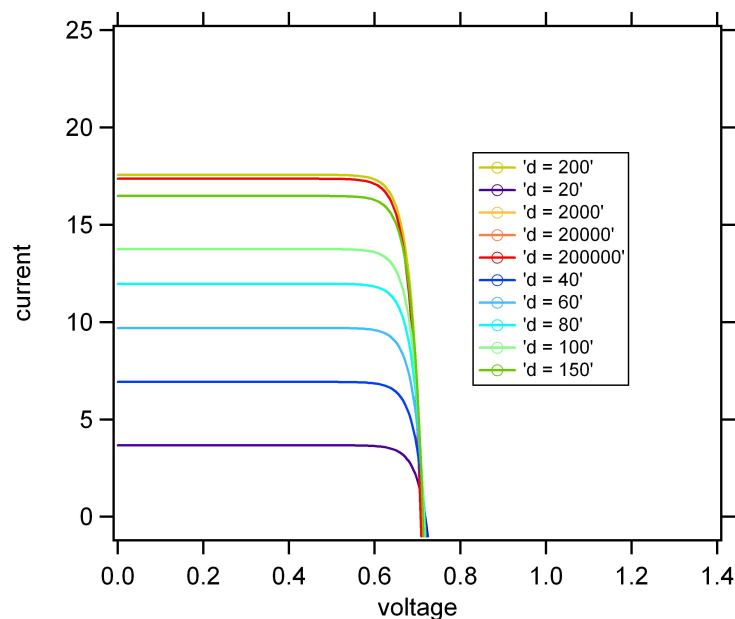
Figure 3.8: IV curves as film thicknesses, d, is changed.

improvements are possible.

3.4.1 Choice of transparent conductive oxide

Conductive substrates are required for charge transfer out of the cell. The usual transparent conducting oxides are indium doped tin oxide or fluorine doped tin oxide.

3.4.2 Choice of photoanode material

The major breakthrough in using dye sensitized films for solar cells came in 1991 with the use of a mesoporous network of TiO_2 as the photoanode. Since then a variety of other materials, including other binary metal oxides (ZnO(6),(7), Nb_2O_5(8),(9)), ternary oxides ($SrTiO_3$(9),(10)), doped metal oxides (Ta(11) or Nb(12) doped TiO_2) or core shell structures (ZnO coated SnO(13)) have also been tried. In recent years work has focussed on not only the proper choice of material but also the optimization of the morphology of the films. These efforts have included work on random nanoparticle arrays, organized

nanotubes(14) and single crystal nanorods(15).

In spite of the works on other materials and structures, TiO_2 nanoparticle-based films still dominate the DSSC device landscape. Although different crystalline forms (rutile, brookite, anatase) of TiO_2 exist naturally, the larger band gap and higher Ecb of the anatase phase makes it the favorite for DSSC applications. The usual fabrication processes of TiO_2 films are based on sol-gel or hydrothermal routes starting from hydrolysis of a titanium precursor such as titanium(IV) alkoxide using water as a catalyst in an acid or base, followed by hydrothermal growth and crystallization. Control of the shape, size and properties may be accomplished by tuning the rate of hydrolysis, temperature, and water content.

Although much work has been done in growing TiO_2 films this way, the advances of this method cannot be readily translated when trying to develop other materials. A lack of clear understanding of the growth processes prevents the tailoring of morphologies of films. Together, these factors make controlled investigations of different materials and different structures for DSSCs a difficult process.

3.4.3   Choice of chromophore

The first step in the conversion of light to current in DSSCs involves the absorption of light by the chromophore. The absorption of light by the dye starts off a series of reactions (shown below) that act as the functioning steps of a DSSC.

$$dye + h\nu \rightarrow dye^*$$

$$dye^* \rightarrow dye^+ + e^-(injected)$$

$$dye^+ + 3/2I^- \rightarrow dye + 1/2I_3^-$$

$$I_3^- + 2e^- \rightarrow 3I^-$$
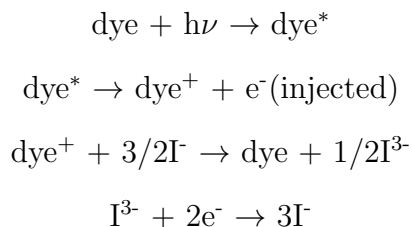
In order for a DSSC to be highly efficient it must start with a dye that satisfies certain requirements. These requirements are:

1. To have high quantum yields of the excited state electron transfer process the dye needs to be well attached to the semiconductor. This is done by a carboxylate or phosphonate binding group.

2. The dye-LUMO should be higher than the CB-semiconductor. The main driving force for the charge injection process is the energy difference between these two levels.

3. The dye-HOMO should be lower than the redox potential for the electrolyte.

4. It must have a high absorption coefficient over large part of the solar spectrum.

5. It must be robust enough to undergo a large number of reduction oxidation cycles without degradation.

Although different types of dyes (based on metal complexes, porphyrins, phthalocyanines and metal-free organics) have been developed over the years, metal complex dyes have been in the forefront of research. These dyes usually consist of a central metal (Ru) ion with ligands attached to it, at least one of which acts as an anchoring group.

For metal complex based dyes the light absorption in the visible part of the solar spectrum is due to a metal-to-ligand charge transfer (MLCT). This makes the choice of the metal complex an extremely important step. Ru-based dyes with large absorption coefficients(16), long excited lifetimes, electrochemical stability(17) and aligning of energy levels to those with anatase TiO_2 have therefore been at the forefront of research in dyes.

Changing of the ligands also plays an important part in tuning the photophysical and electrochemical processes and in turn results in changes in their photovoltaic behavior. Since its discovery in 1993(18), the N3 dye shown in figure (3.9) and its protonated versions (N719 and N712) have remained the benchmark against which other metal complex based dyes have been measured. Amongst the three, the completely protonated
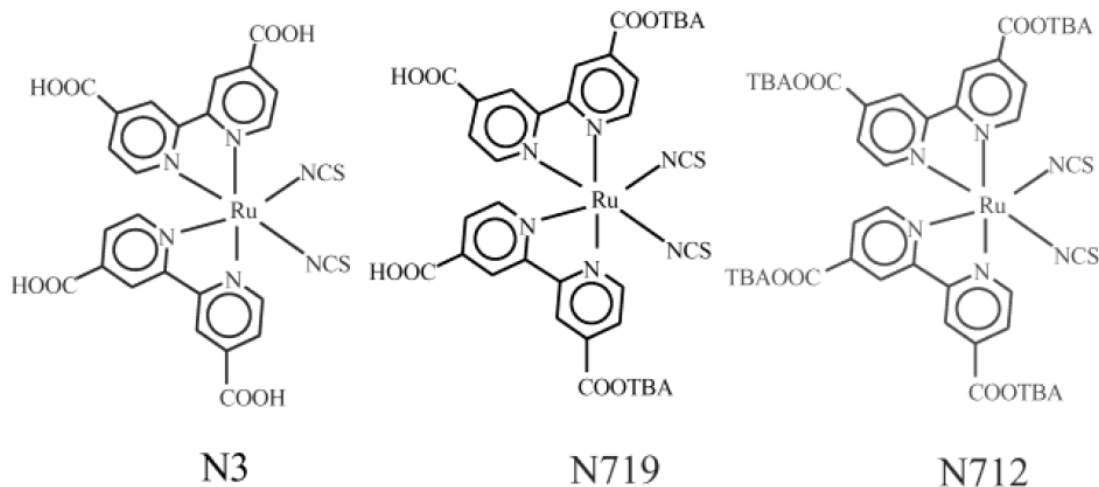
Figure 3.9: The structures for the most commonly used variation of Ru-based dyes, N719, N712 and N749.

N3 dye postively charges the TiO$_2$ surface causing an increase in the photocurrent but a drop in the open circuit voltage. With the completely deprotonated N712, the reverse happens due to negatively charging the TiO$_2$ surface. The best photvoltaic performance is seen for the doubly protonated N719 dye (power conversion efficiency above 8%).

Further improvements over N719 were made in 1997 with the introduction of N749 or "black dye"(19). The introduction of black dye pushed the power conversion efficiency of DSSCs to above 10%. The main gain of N749 over N719 was the larger absorption in the red part of the solar spectrum as shown in the action spectrum of devices sensitized by the two dyes (figure 3.10).

Further device improvements are constantly being sought by tailoring of dyes. The latest efficiency increases have utilized multiple dyes at the same time. Initial efforts included combining N749 with an organic dye, D131,(20) which raised power conversion efficiencies to above 11%. The latest results show a power conversion efficiency of higher than 12% using a variation of the porphyrin dye YD2 called YD2-o-C8(3), both structures are shown in figure 3.11.
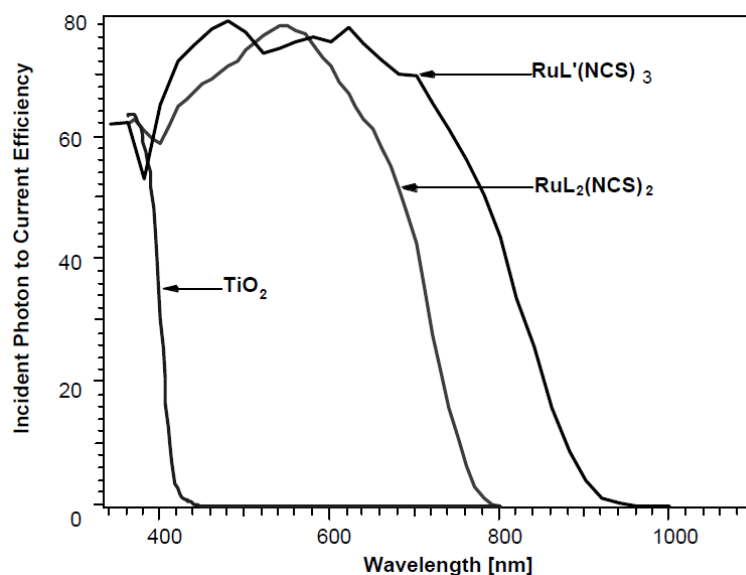
Figure 3.10: The IPCE for bare TiO$_2$ compared to those sensitized with N719 and N749.
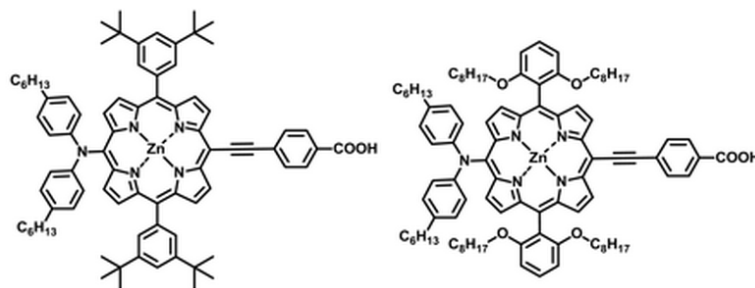
Figure 3.11: Chemical structures of porphyrin based dyes(a)YD2 and (b)YD2-o-C8

3.4.4 Choice of electrolyte

Electrolytes for DSSCs consists of redox components, a solvent to dissolve the components and additives that enhance the overall device performance. In their original work on DSSCs Grätzel and O' Regan used an electrolyte that was based on ethylene carbonate and acetonitrile (80:20) (v:v) with 0.5 M tetrapropylammonium iodide and 0.04 M iodine. A lot of research has since then been conducted on designing electrolytes that are better suited to device performance.

The requirements for electrolyte solvents for DSSCs are:

46

1. chemically stable,

2. low viscosity to minimize transport problems,

3. good solvent for redox components,

4. does not dissolve dye or semiconductor,

5. compatible with sealing material.

The most commonly used electrolytes still use a variation of LiI and I_2 in acetonitrile. Using various additives in the electrolyte has caused improved device performance. The most commonly used additive is 4-tert-Butylpyridine (TBP). It was first used by Grätzel *et al.* in 1993, producing a much enhanced V_{oc}(18). Using intensity-modulated-voltage-spectroscopy (IMVS) it was shown that addition of TBP causes a shift of the E_{cb} of TiO_2 to higher energies(21). Further, addition of TBP has also been shown to increase electron lifetime(22). The other commonly-used additive guanidinium thiocyanate shifts the TiO_2 E_{cb} to lower values but still increases the electron lifetime(23). Besides TBP a large number of other pyridines and N-heterocycles (24),(25) have also been tried as additives. The main improvement has been noted in V_{oc} due to the decreased recombination rates.

Although a large amount of work has been done in understanding the workings of the electrolyte and its interactions with TiO_2 substrate and the dyes, a lot more needs to be done in order for a clear picture to emerge.

In very recent times cobalt$(2^+/3^+)$-based redox shuttles are gaining in popularity(26). The advantage of the cobalt shuttle with respect to the iodine based couple is the lower over potential for the dye reduction process. Work done by Hupp *et al.* is also helping in understanding the reduction mechanism better than that for the I^{3-}/I^- couple which reacts via mechanisms that remain unclear but involve transfer of multiple electrons.

3.4.5 Choice of counter-electrode material

Counter electrodes usually consist of a thin catalytic layer of Pt on the conductive substrate. The Pt layer decreases the charge-transfer resistance compared to that of the bare FTO substrate for the standard iodide/ triiodide couple. Other cheaper alternatives to the Pt electrode include carbon-based(27) and organic polymer-based (PEDOT(28),)(29) counter electrodes. However it seems the most likely alternative to the Pt counter electrode is cobalt sulfide (CoS)(30), which has already shown to be able to outperform Pt electrodes.

3.5 Device fabrication protocol

Once we have chosen our materials, its time to fabricate the different parts of our device.

3.5.1 Preparing substrates

Preparing of substrates includes cutting of the conductive glass into 1.5 cm x 2.5 cm pieces. This is then followed by cleaning of the substrates. Cleaning is done by sonicating substrates in acetone for 8 minutes followed by sonicating in isopropyl alcohol for 8 minutes. The substrates are then ozone cleaned for 8 minutes. For substrates to be used for counter electrodes, cleaning is preceded by sand blasting a hole (r $\sim$ 2 mm) in the substrate for introduction of electrolyte later.

3.5.2 Preparing photoanodes

Photoanodes consisting of Fluorine-doped Tin oxide (FTO) glass coated with the required material are fabricated by pulsed laser deposition (PLD) from the corresponding target (2" diameter, 1/8$^{\text{th}}$" thickness from Kurt J Lesker, at least 99.9% purity) with a KrF excimer laser (λ=248 nm, pulse energy in the range of 200mJ to 300 mJ, pulse

frequency of 10hz to 100 Hz) focused with a 60 degree incidence angle into the chamber and rastered over the target. The resulting plume was directed at FTO glass held at a height ranging from 5 cm to 9 cm above the target. Both the target and the FTO substrate were continuously rotated at 40 rpm and 20 rpm, respectively, for uniform deposition. Prior to deposition, the PLD chamber is evacuated to a base pressure of 6 x 10^{-6}Torr. PLD takes advantage of the high energy of the ablated species to allow film growth even at high gas background pressures, a feature not shared with other physical sputtering methods.

3.5.3 Preparing counter electrode

Platinum counter electrodes are obtained starting from a 5 mM H_2PtCl_6 solution in ethanol. 1 ml of the solution is dropped on a pre-drilled FTO substrate. It is then heated at 500C for 15 minutes, followed by another 1 ml drop and another fifteen minutes of heating at the same temperature.

3.5.4 Preparing dye solution

Two dyes (N3 and N719) were used for sensitizing photoanodes.

For the N3 dye solution, $2x10^{-4}$M $Ru(dcbpyH)_2(NCS)_2$ (N3) was added in C_2H_5OH (ethanol) solution and then sonicated.

For the N719 dye solution, $3x10^{-4}$M N719 dye was added to a mixture of acetontrile:tert-butanol (1:1) (v:v) solution and then sonicated.

Photoanodes were derivatized with dye using the "hot slide" technique where the films were heated to 500 C for 30 minutes immediately prior to derivatization by the complex. The films were submerged in solution overnight.

3.5.5 Preparing electrolyte solution

I have used three different electrolytes for the DSSCs used in the next chapter. The concentration of the different components in the different electrolytes is as shown below. Electrolyte solutions were made in 20-ml batches. Each cell needed 1 ml of electrolyte.

Electrolyte 1: 0.5 M LiI, 0.05 M I_2 in dried acetonitrile.

Electrolyte 2: 0.1 M LiI, 0.05 M I_2, 0.6 M dimethyl propyl imidazolium iodide, and 0.5 M tert-butylpyridine in dried acetonitrile.

Electrolyte 3: 0.05M LiI, 0.03M I_2, 1M dimethyl propyl imidazolium iodide, 0.5 M tert-butylpyridine and 0.1M guanidinium thiocyanate in dried acetonitrile: valeronitrile (85:15) (v:v).

3.5.6 Putting it together

The process of putting together a sandwich cell consists of the following steps.

1. The photoanode and cathode are aligned with a Surlyn$^©$ spacer (25μm thick).

2. The three parts are put together and then heated at 150 C for 7 seconds. This makes the sandwich structure.

3. A drop of electrolyte is then put on top of the opening on the counter electrode. The air in the space between the electrodes is evacuated. The electrolyte can now get into that region.

4. A small glass slide is used to seal off the structure so that electrolyte cannot evaporate.
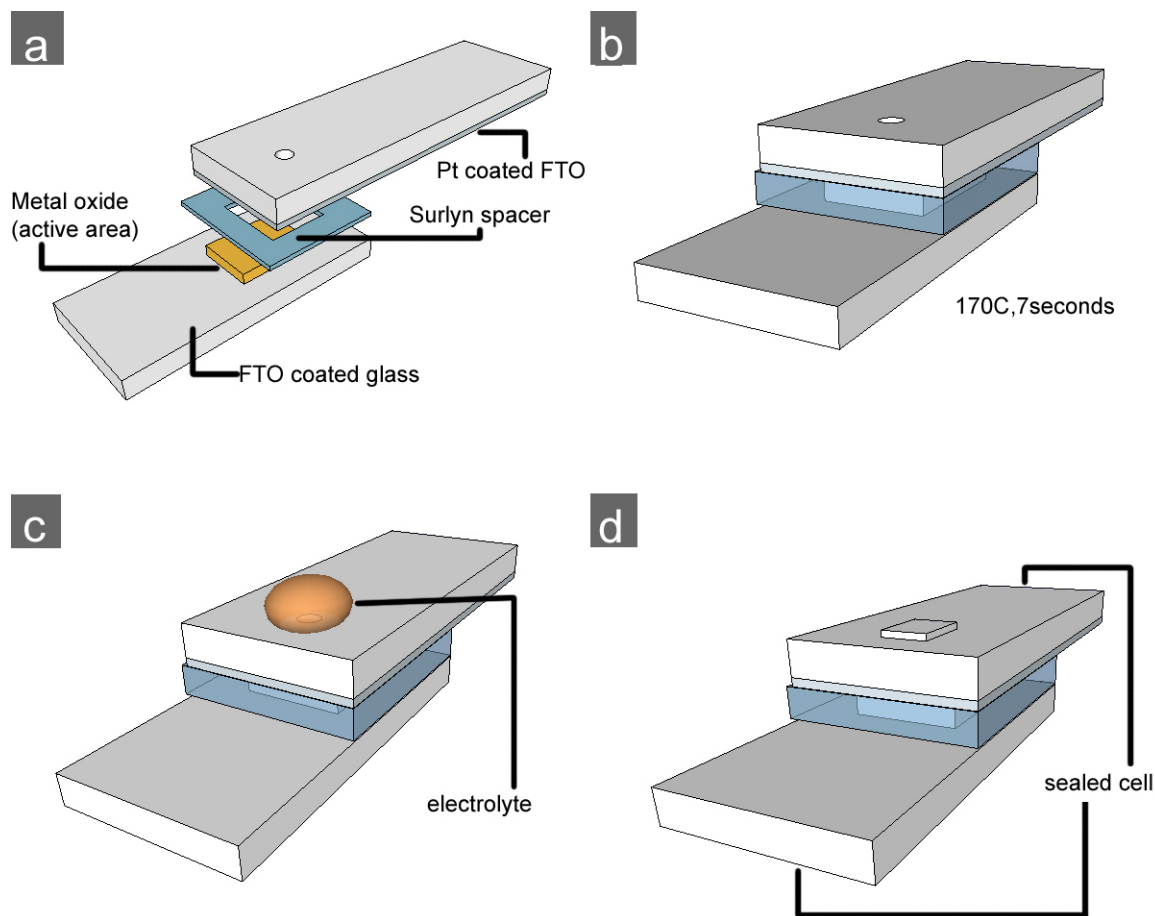
Figure 3.12: The different steps involved in the device fabrication process.

3.6 Characterization

3.6.1 Morphology

Scanning Electron Microscopy

SEM imaging of films was done using a Hitachi S-4700 Cold Cathode Field Emission Scanning Electron Microscope. The usual operating conditions during imaging were 2 kV and 10 μAmps. Cross sectional imaging was done using a L-mount.

Transmission Electron Microscopy

Transmission electron microscope images were obtained in the normal transmission (TEM) mode and scanning (STEM) mode using a JEOL 2010F-FasTEM using 200kV accelerating voltage. Elemental mapping was done using the STEM mode using the INCA EnergyTEM 250 TEM microanalysis system with imaging capabilities.

3.6.2 Chemical and Structural

X-ray Photoelectron Spectroscopy

Chemical composition and metal oxidation states were obtained using x-ray photoelectron spectroscopy (XPS) on a Thermo K-alpha system using an Al-Kα monochromated source.

X-ray diffraction

The crystalline structures of our photoanodes were obtained using x-ray diffraction using a Rigaku MultiFlex X-ray Diffractometer, with a Cu Kα radiation, at 40 kV-40 mA at a scan speed of 4º /min.

Raman

Raman measurements were made using a Dilor XY Triple spectrograph with a liquid nitrogen cooled CCD detector, using a 514.5 nm wavelength argon ion laser at 200 mW.

Spectral Electrochemistry

Electrochemistry is combined with UV-vis measurements in spectral electrochemistry. The onset of accumulation of charges can be related to the conduction band of the metal oxide. This is reflected as a change in the UV-vis spectra obtained and gives us a method of ascertaining the conduction band edge (31).

3.6.3 Absorbance

The first step in the functioning of a DSSC is the absorption of light by the dye attached on the metal oxide surface. A quantitative measurement of this step is obtained in terms of Light Harvesting Efficiency (LHE) or absorptance. There are various ways of making these measurements.

The first way is to desorb the dye off the surface and obtain the absorption spectrum of the solution into which the dye has desorbed. Knowledge of the extinction coefficient and the length of the liquid column through which light has to pass lets us know the concentration of dye in the solution. Multiplying by the total volume of the solution gives us the number of moles of dye that has been desorbed from the metal oxide surface. Assuming uniform loading of dye through the volume of the metal oxide we can then calculate the absorbance of the dye-metal oxide system. In this method light-matter interactions that might occur due to morphological changes are ignored as well as absorbance due to patterned and layered structures cannot be well quantified.

The second method to obtain absorbance is to obtain the UV-vis spectrum for the light passing through the dye- metal oxide film normalized to the incident light. This method is an improvement over desorbing the dye off the film because the effects of film morphology are taken into account. In this case it is assumed that all the light that is not transmitted through the film is absorbed by the film. This in turn means reflected and scattered portions of light are ignored.

The third method, which involves an integrating sphere, considers reflectance, transmittance and scattering effects while calculating absorbance values. This method is especially helpful in cases where film morphologies form a pseudo-waveguiding structure and there is a large effect from "scattered" components.
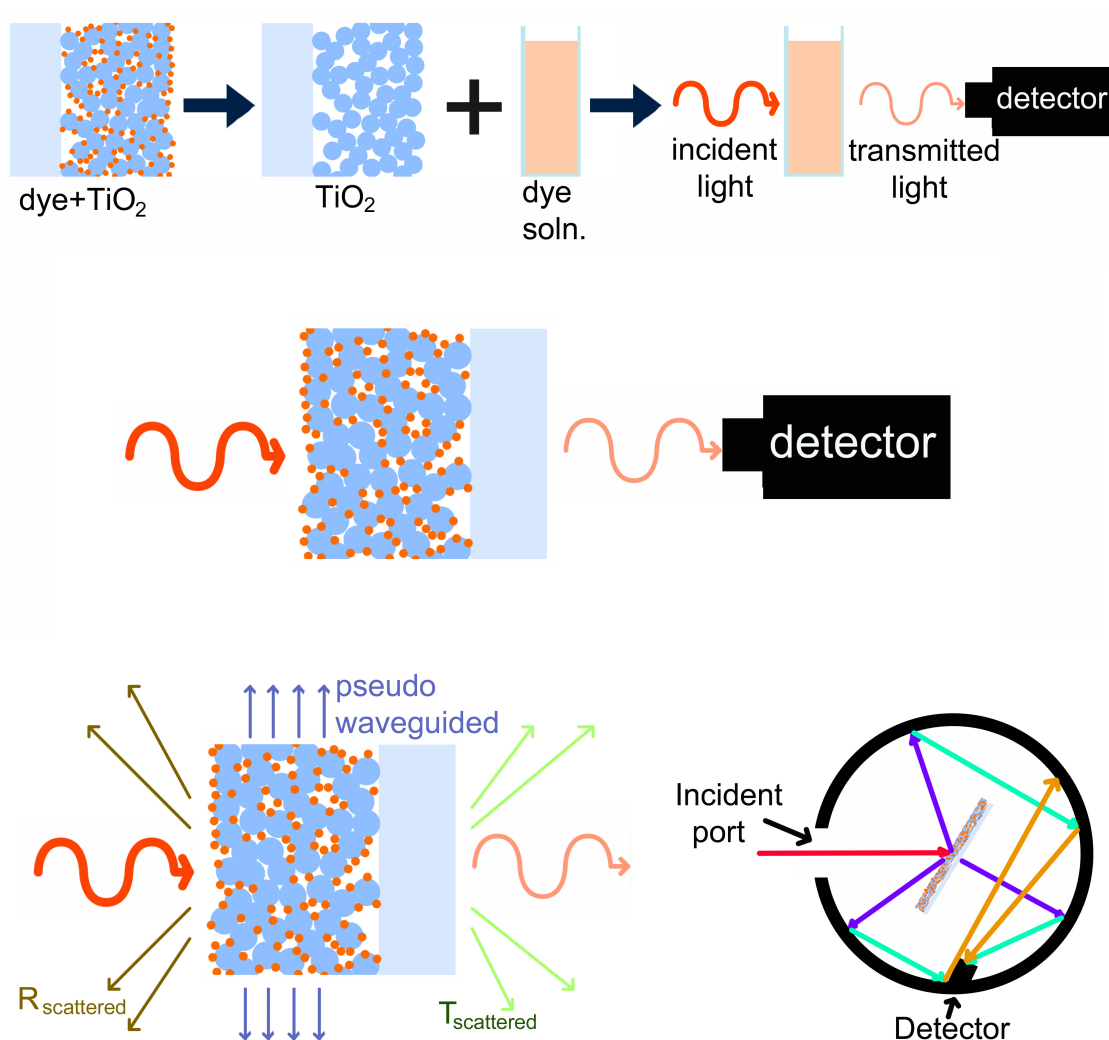
Figure 3.13: The different ways of measuring absorbance by the dye loaded on a photoanode.

3.6.4 Incident Photon to Current Efficiency

In order to learn about the spectral response of a DSSC it is necessary to measure the incident photon to current efficiency(IPCE) of the cell. A monochromator is used to obtain single wavelengths from a white light source. The photocurrent at each wavelength

is measured to obtain the action spectra. The ratio of the photocurrent obtained to the incident power at the given wavelength dictates the corresponding IPCE. The equation used is:

$$IPCE = \frac{1240J_{sc}(mAcm^{-2})}{\lambda(nm)P_{in}(mWcm^{-2})}$$
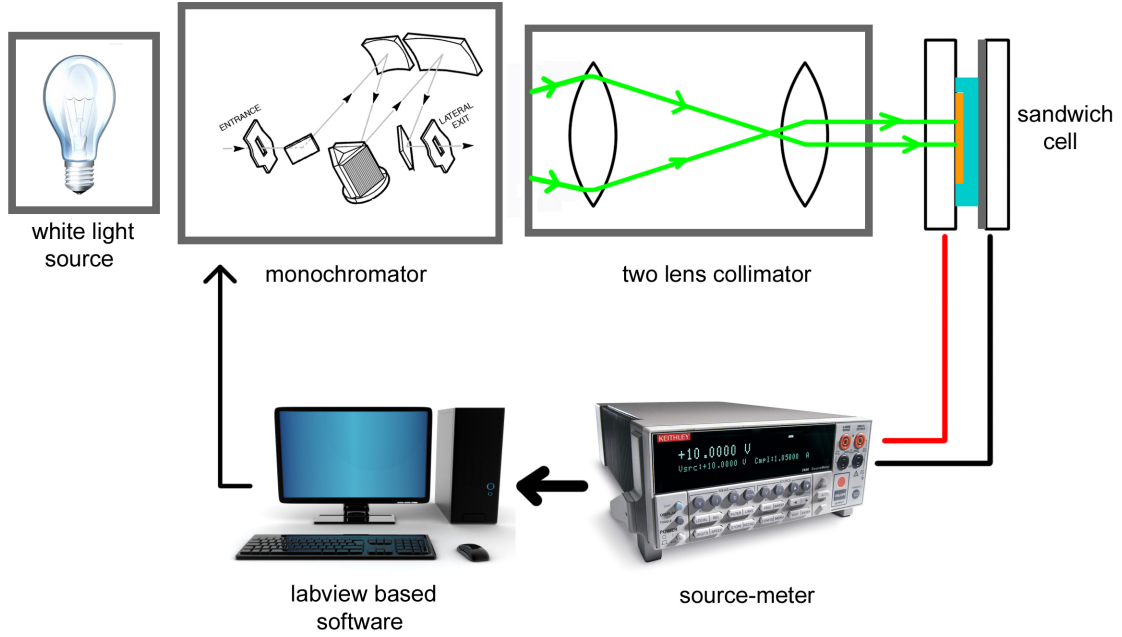
Figure 3.14: A schematic diagram of the IPCE measurement setup.

Our experimental setup is shown in the figure above. It consists of a light source (75W Xe Oriel 6251) that goes through a monochromator (Oriel Cornerstone 260). The light then goes through a two-lens collimating setup before being made incident normal to the DSSC. A Keithley2400 source-meter is used to measure photocurrent which is then input into a labview program.

3.6.5 Current Voltage

In order to obtain the power conversion efficiency of a DSSC, it is necessary to obtain the current-voltage curve under illumination. From the curve, the current density under short circuit conditions (J_{sc}) and the voltage under open circuit conditions (V_{oc}) can be noted. The maximum power output (P_{max}) is noted from the maximum of —V x J—. The power conversion efficiency, η, of the DSSC is then:

$$\eta = \frac{P_{max}}{P_{input}}$$

In most cases the input power is set to 1sun at AM1.5. This corresponds to $100mW/cm^2$. P_{max} may also be written in terms of J_{sc} and V_{oc}.

$$P_{max} = J_{sc}V_{oc}FF$$

Here FF stands for fill factor. Fill factor is a measure of the square-ness of the J-V curve. In physical terms it tells us how close the behavior of the DSSC is to an ideal diode. FF will differ from 1 (ideal diode) due to power losses because of non-ideal contacts, current leaks and other losses. Therefore η may also be written as:

$$\eta = \frac{J_{sc}V_{oc}FF}{P_{input}}$$

Ideally J-V curve measurements should be done in both dark and illuminated states. Although dark currents do not provide us with information about the efficiency of the cell under normal operating conditions, they can still provide us with information about recombination rates and other important factors.

3.6.6 Electrochemical Impedance Spectroscopy

Electrochemical Impedance Spectroscopy (EIS) is a very useful tool in understanding the movement of charges through the whole device. EIS measurements are done by applying a steady voltage that is then perturbed by a small sinusoidal voltage. The nature of the current (amplitude, phase and frequency) due to this voltage is then measured. The impedance is defined as the ratio of the current to the voltage and is a complex number. This impedance may be modeled as an equivalent circuit.

The equivalent circuit consists mostly of resistors and capacitors. Every interface (metal oxide - electrolyte, FTO - metal oxide, FTO - electrolyte, Pt - electrolyte) gives rise to a resistance to charge transfer and causes a charge accumulation region (giving rise to capacitances). Further even during diffusive transfer processes through the porous network, the charges face resistance which is usually modeled as a combination of resistances and a Warburg element as shown in figure 3.15. The following parameters can be obtained using EIS: (a) series resistance, (b) charge transfer resistance of the counter electrode, (c) diffusion resistance of the electrolyte, (d) the resistance of electron transport and recombination in the TiO_2, and (e) the chemical capacitance of the porous TiO_2 electrode.

The electrochemical impedance spectrum is shown in either the form of Nyquist plots or Bode plots. The Nyquist plots are more common and show Z-imaginary plotted against Z-real. For a DSSC this appears as a set of three semi-circular plots put together corresponding to the different parts of the device, as shown in figure 3.15. The Bode plot shows the magnitude of the total impedance as a function of the frequency.

3.6.7 Open Circuit Voltage Decay

The open circuit voltage is a measurement of the quasi-Fermi level, which is dictated by the density of electrons in the conduction band. In the OCVD measurement, the
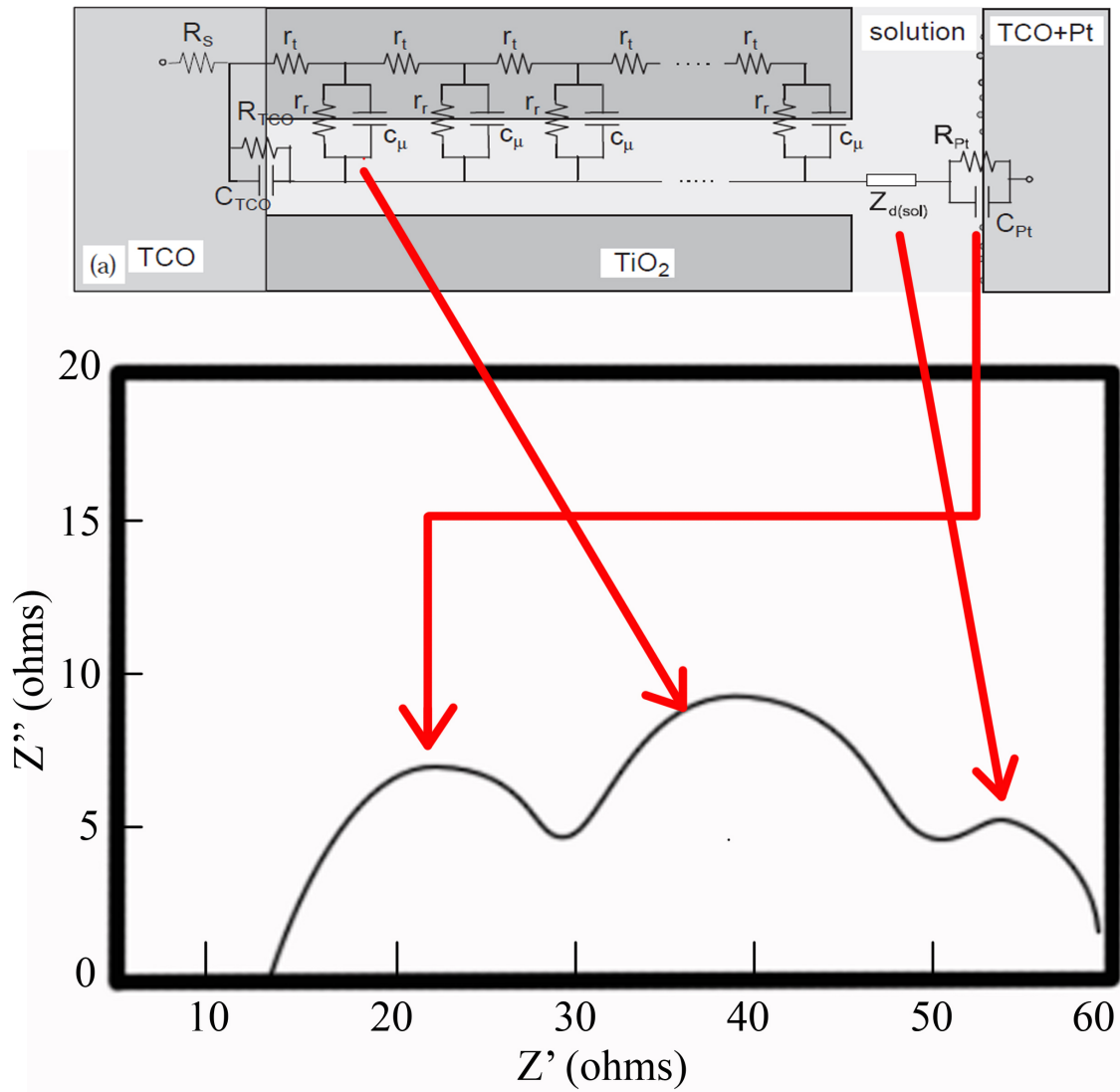
Figure 3.15: Transmission line model used for DSSCs. Typical Nyquist plots for a DSSC and their connection to the different interfaces of a DSSC.

change in V_{oc} is monitored in the dark, after a period of illumination. In this dark state there is a loss of photoelectrons and reduction in the V_{oc} due to electron recombination processes. The rate of decay of V_{oc} therefore is a direct measure of the recombination rate.

References

1. Moser, J. (1887) Notiz über verstärkung photoelektrischer ströme durch optische sensibilisirung. Monatshefte für Chemie/Chemical Monthly **8**, 373–373

2. O'regan, B. and Gratzel, M. (1991) A low-cost, high-efficiency solar cell based on dye-sensitized colloidal ti02 films. Nature **353**, 737–740

3. Yella, A., Lee, H., Tsao, H., Yi, C., Chandiran, A., Nazeeruddin, M., Diau, E., Yeh, C., Zakeeruddin, S., and Grätzel, M. (2011) Porphyrin-sensitized solar cells with cobalt (ii/iii)–based redox electrolyte exceed 12 percent efficiency. Science **334**, 629–634

4. Jose, R., Thavasi, V., and Ramakrishna, S. (2009) Metal oxides for dye-sensitized solar cells. Journal of the American Ceramic Society **92**, 289–301

5. Würfel, U., Wagner, J., and Hinsch, A. (2005) Spatial electron distribution and its origin in the nanoporous tio2 network of a dye solar cell. The Journal of Physical Chemistry B **109**, 20444–20448

6. Rensmo, H., Keis, K., Lindström, H., Södergren, S., Solbrand, A., Hagfeldt, A., Lindquist, S., Wang, L., and Muhammed, M. (1997) High light-to-energy conversion efficiencies for solar cells based on nanostructured zno electrodes. The Journal of Physical Chemistry B **101**, 2598–2601

7. Rao, T. and Bahadur, L. (1997) Photoelectrochemical studies on dye-sensitized particulate zno thin-film photoelectrodes in nonaqueous media. Journal of the Electrochemical Society **144**, 179

8. Hoshikawa, T., Kikuchi, R., Sasaki, K., and Eguchi, K. (2002) Impedance analysis of electronic transport in dye-sensitized solar cells (e). ELECTROCHEMISTRY-TOKYO- **70**, 675–680

9. Lenzmann, F., Krueger, J., Burnside, S., Brooks, K., Grätzel, M., Gal, D., Rühle, S., and Cahen, D. (2001) Surface photovoltage spectroscopy of dye-sensitized solar cells with tio2, nb2o5, and srtio3 nanocrystalline photoanodes: Indication

for electron injection from higher excited dye states. The Journal of Physical Chemistry B **105**, 6347–6352

10. Burnside, S., Moser, J., Brooks, K., Grätzel, M., and Cahen, D. (1999) Nanocrystalline mesoporous strontium titanate as photoelectrode material for photosensitized solar devices: increasing photovoltage through flatband potential engineering. The Journal of Physical Chemistry B **103**, 9328–9332

11. Liu, J., Yang, H., Tan, W., Zhou, X., and Lin, Y. (2010) Photovoltaic performance improvement of dye-sensitized solar cells based on tantalum-doped tio¡ sub¿ 2¡/sub¿ thin films. Electrochimica Acta **56**, 396–400

12. Lü, X., Mou, X., Wu, J., Zhang, D., Zhang, L., Huang, F., Xu, F., and Huang, S. (2010) Improved-performance dye-sensitized solar cells using nb-doped tio2 electrodes: Efficient electron injection and transfer. Advanced Functional Materials **20**, 509–515

13. Kay, A. and Grätzel, M. (2002) Dye-sensitized core-shell nanocrystals: improved efficiency of mesoporous tin oxide electrodes coated with a thin layer of an insulating oxide. Chemistry of materials **14**, 2930–2935

14. Jennings, J., Ghicov, A., Peter, L., Schmuki, P., and Walker, A. (2008) Dye-sensitized solar cells based on oriented tio2 nanotube arrays: Transport, trapping, and transfer of electrons. Journal of the American Chemical Society **130**, 13364–13372

15. Galoppini, E., Rochford, J., Chen, H., Saraf, G., Lu, Y., Hagfeldt, A., and Boschloo, G. (2006) Fast electron transport in metal organic vapor deposition grown dye-sensitized zno nanorod solar cells. The Journal of Physical Chemistry B **110**, 16159–16161

16. Kuang, D., Ito, S., Wenger, B., Klein, C., Moser, J., Humphry-Baker, R., Zakeeruddin, S., and Grätzel, M. (2006) High molar extinction coefficient heteroleptic ruthenium complexes for thin film dye-sensitized solar cells. Journal of the American Chemical Society **128**, 4146–4154

17. Kuang, D., Klein, C., Ito, S., Moser, J., Humphry-Baker, R., Evans, N., Duriaux, F., Grätzel, C., Zakeeruddin, S., and Grätzel, M. (2007) High-efficiency and stable mesoscopic dye-sensitized solar cells based on a high molar extinction

coefficient ruthenium sensitizer and nonvolatile electrolyte. Advanced Materials **19**, 1133–1137

18. Nazeeruddin, M., Kay, A., Rodicio, I., Humphry-Baker, R., Müller, E., Liska, P., Vlachopoulos, N., and Grätzel, M. (1993) Conversion of light to electricity by cis-x2bis (2, 2'-bipyridyl-4, 4'-dicarboxylate) ruthenium (ii) charge-transfer sensitizers (x= cl-, br-, i-, cn-, and scn-) on nanocrystalline titanium dioxide electrodes. Journal of the American Chemical Society **115**, 6382–6390

19. Nazeeruddin, M., Péchy, P., and Grätzel, M. (1997) Efficient panchromatic sensitization of nanocrystallinetio2 films by a black dye based on atrithiocyanato–ruthenium complex. Chem. Commun. 1705–1706

20. Ogura, R., Nakane, S., Morooka, M., Orihashi, M., Suzuki, Y., and Noda, K. (2009) High-performance dye-sensitized solar cell with a multiple dye system. Applied Physics Letters **94**, 073308

21. Schlichthörl, G., Huang, S., Sprague, J., and Frank, A. (1997) Band edge movement and recombination kinetics in dye-sensitized nanocrystalline tio2 solar cells: a study by intensity modulated photovoltage spectroscopy. The Journal of Physical Chemistry B **101**, 8141–8155

22. Boschloo, G. and Hagfeldt, A. (2001) Spectroelectrochemistry of nanostructured nio. The Journal of Physical Chemistry B **105**, 3039–3044

23. Kopidakis, N., Neale, N., and Frank, A. (2006) Effect of an adsorbent on recombination and band-edge movement in dye-sensitized tio2 solar cells: Evidence for surface passivation. The Journal of Physical Chemistry B **110**, 12485–12489

24. Huang, S., Schlichthörl, G., Nozik, A., Grätzel, M., and Frank, A. (1997) Charge recombination in dye-sensitized nanocrystalline tio2 solar cells. The Journal of Physical Chemistry B **101**, 2576–2582

25. Zhang, C., Dai, J., Huo, Z., Pan, X., Hu, L., Kong, F., Huang, Y., Sui, Y., Fang, X., Wang, K., et al. (2008) Influence of 1-methylbenzimidazole interactions with li+ and tio2 on the performance of dye-sensitized solar cells. Electrochimica Acta **53**, 5503–5508

26. Yum, J., Baranoff, E., Kessler, F., Moehl, T., Ahmad, S., Bessho, T., Mar-

chioro, A., Ghadiri, E., Moser, J., Yi, C., et al. (2012) A cobalt complex redox shuttle for dye-sensitized solar cells with high open-circuit potentials. Nature Communications **3**, 631

27. Murakami, T., Ito, S., Wang, Q., Nazeeruddin, M., Bessho, T., Cesar, I., Liska, P., Humphry-Baker, R., Comte, P., Péchy, P., et al. (2006) Highly efficient dye-sensitized solar cells based on carbon black counter electrodes. Journal of the Electrochemical Society **153**, A2255

28. Bay, L., West, K., Winther-Jensen, B., and Jacobsen, T. (2006) Electrochemical reaction rates in a dye-sensitised solar cell–the iodide/tri-iodide redox system. Solar energy materials and solar cells **90**, 341–351

29. Saito, Y., Kitamura, T., Wada, Y., and Yanagida, S. (2002) Application of poly (3, 4-ethylenedioxythiophene) to counter electrode in dye-sensitized solar cells. Chemistry Letters **31**, 1060–1061

30. Wang, M., Anghel, A., Marsan, B., Cevey Ha, N., Pootrakulchote, N., Zakeeruddin, S., and Gra?tzel, M. (2009) Cos supersedes pt as efficient electrocatalyst for triiodide reduction in dye-sensitized solar cells. Journal of the American Chemical Society **131**, 15976–15977

31. O'Regan, B., Grätzel, M., and Fitzmaurice, D. (1991) Optical electrochemistry i: steady-state spectroscopy of conduction-band electrons in a metal oxide semiconductor electrode. Chemical physics letters **183**, 89–93

Chapter 4

Optimizing Dye Sensitized Solar Cells: different approaches

4.1 Introduction

Since Grätzel's first report((1)) in 1991 of a 7.1% efficient dye-sensitized solar cell (DSSC) based on nanocrystalline TiO_2 and a fast regenerative photoelectrochemical process, many researchers have sought to improve its performance and overcome its limitations. Today the power conversion efficiency of DSSCs has been improved to 12.5%,((2)) but their efficiencies are still 55-75% of the theoretical maximum, depending on the dye used.((3)) Repeating what we already mentioned in the last chapter, DSSCs((4)) are made from a photoanode, counter electrode coated with colloidal platinum, and a redox electrolyte, e.g. I^{3-}/I^-, operating regeneratively. The photoanode is composed of a few-micron-thick film of interconnected metal oxide semiconductor nanoparticles coated with light harvesting molecules deposited on a transparent conductive substrate, typically indium tin oxide (ITO) or fluorine-doped tin oxide (FTO) coated glass. The mesoporous nanoparticle film increases the effective surface by 10^3 over a planar surface, dramatically enhancing light absorption while still allowing semiconductor-electrolyte contact throughout the entire film.

In order to improve the efficiencies of DSSCs, we draw upon our knowledge of their

functioning as mentioned in the last chapter. In this chapter I describe the different methods attempted, the results obtained and the conclusions drawn from each of these efforts.

4.2 Directional structures vs random nanoparticle network: Laser ablated TiO$_2$ versus sol gel fabricated TiO$_2$

The most successful DSSCs are made from nanocrystalline TiO$_2$ but overall performance is limited by three main factors. First, increasing the film thickness beyond 10μm to maximize light harvesting diminishes the device efficiency due to slow trap-limited electron diffusion. For TiO$_2$, the transport of charge within this disordered nanostructure is dominated by diffusion ((5), (6), (7)) and is thought to be a consequence of a high dielectric constant and small nanocrystal size such that photogenerated charge carriers are screened from significant electric fields by the electrolyte. This limits the effective electron diffusion length to about 10μm ((8), (9)) and results in an efficiency-limiting trade-off between light absorption and carrier extraction. Secondly, the thick percolating network of TiO$_2$ nanoparticles drastically increases the opportunity for electron recombination with oxidized redox carriers on or near the electrode surface. Thirdly, the network of channels surrounding the nanoparticles is tight and convoluted all across the active area, limiting dye regeneration by slowing the movement of electrolyte ions. Thinner TiO$_2$ nanoparticle films minimize the drawbacks of the percolating network, reduce dark current losses, and increase overall cell efficiency(6) but ultimately limit the fraction of the incident light absorbed, which precludes the use of thinner photoactive layers.

The random nanoparticle network (schematic shown in figure 4.1) is clearly not ideal

but is widely used because it provides the needed surface area and is easily synthesized from standard sol gel methods. Crystalline compact thin film structures provide the best mobility parameters for charge transport but their low surface areas give unacceptably poor dye loading. Columnar nanorods (schematic shown in figure 4.2) retain most of the transport characteristics of a single crystal but surface areas remain insufficient.((10), (11), (12))
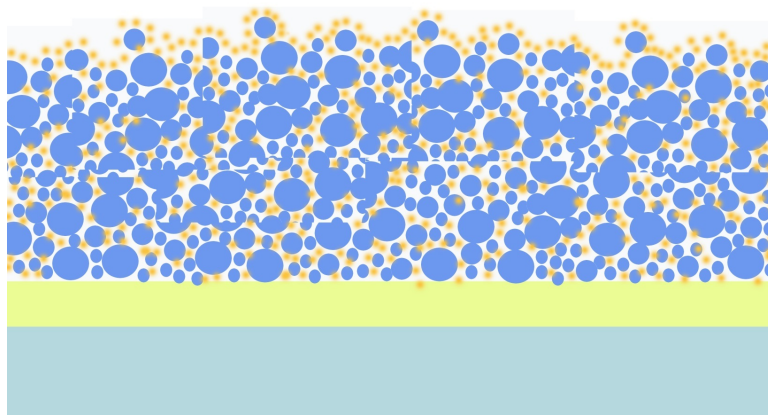
Figure 4.1: Random nanoparticle networks provide large surface areas for improved dye loading. However, this also increases possible charge losses.

An optimized structure would therefore be able to combine the best features of both of these structures. In theory therefore a structure similar to the one shown schematically in figure 4.3 would be extremely suitable for DSSC applications.

The ability to tailor structures using a PLD system gives the freedom to try and obtain such structures and evaluate their device behaviors. This new structural motif for the photoanode was independently grown by us as well by the Grätzel group((13)) at around the same time. In the results discussed later I compare the behavior of this new structure to that of the conventional sol-gel nanoparticle based devices. Further I have studied the influence of oxygen background pressure in dye-loading and photo-conversion
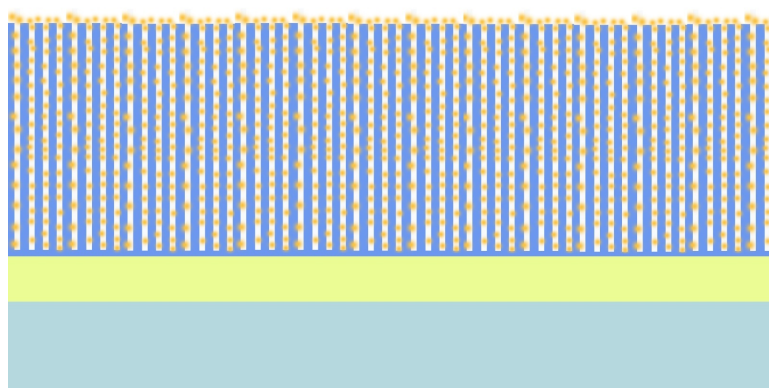
Figure 4.2: Nanorod-based structures improve charge transfer. This comes at the cost of efficient dye loading due to decreased surface area.
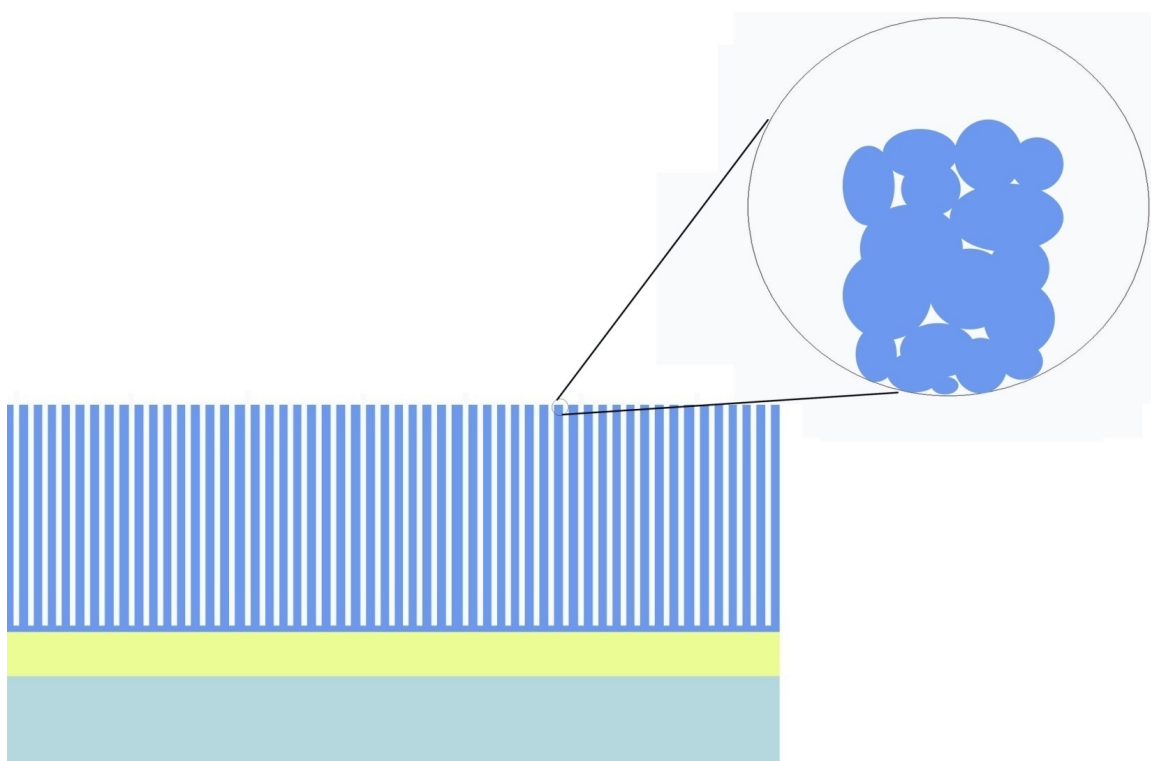
Figure 4.3: An optimized structure combines the high surface area provided by the nanoparticle network with the directionality of a nanorod-based photoanode.

properties of this new TiO_2 nanostructure. I show that the absorbed-photon-to-current efficiencies (APCE) improve to values above 90% over most of the dye absorption range for oxygen pressures around 8 Pa. The bundled anode also presents an enhanced surface surface area around 1.4 times larger than that of traditional anodes. While others have used PLD ((14), (15), (16), (17)) to fabricate TiO_2 photoanodes, this tailoring of film structures using background oxygen pressure might open a path to a marriage of the best properties of random nanoparticle networks with those of oriented single crystal nanotubes and rods.
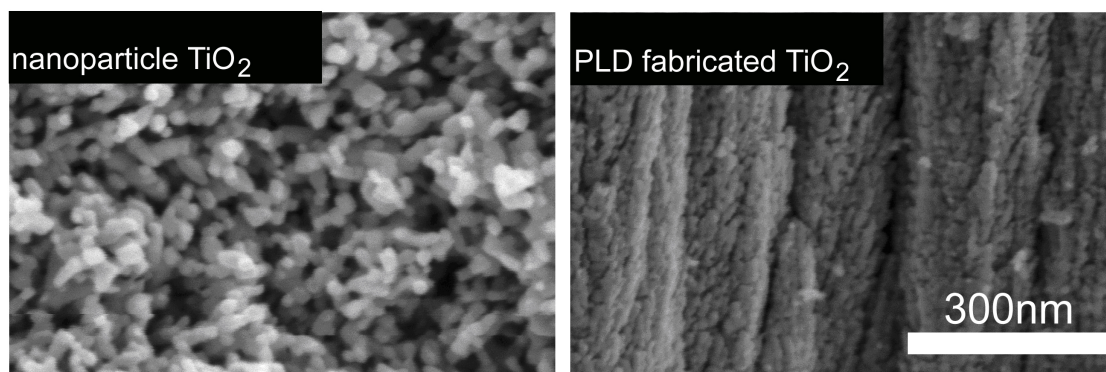
Figure 4.4: Films based on the conventional sol-gel method produce a porous non-oriented structure. Tailored structures to optimize device performance like the one shown to the right can be obtained using PLD.

4.2.1 Experiment

Photoanodes were fabricated by ablating a TiO_2 target with a KrF excimer laser (λ=248nm) operated at a pulse energy of 300 mJ and 40 Hz repetition rate. The laser beam was focused with a 60 deg incidence angle into the chamber and rastered over the target (pulse fluence 0.5 mJ/cm^2). The plume obtained was deposited on fluorine-doped tin oxide (FTO) coated glass substrates that were held on the substrate holder at a 5 cm distance above the target. In order to assure uniform deposition both the target and the substrates were continuously rotated at 40 rpm and 20 rpm, respectively. The PLD

chamber was evacuated to a base pressure of 6×10^{-6} Torr before deposition. During deposition a background pressure of oxygen was maintained in the range of 30 mTorr to 250 mTorr. Films obtained were then annealed at 500C for an hour in air. All films were fabricated using 60000 shots.

The films were derivatized by soaking them in a 2×10^{-4} M solution of N3 dye Ru(4,4-$(COOH)_2$bpy)$_2$(NCS)$_2$ (made according to literature procedures; 4,4-$(COOH)_2$bpy is 4,4-dicarboxylic acid-2,2- bipyridine) ((18)) in ethanol solution overnight.

Scanning electron microscopy using a Hitachi S-4700 operated at an accelerating voltage of 2 kV was used to obtain structural and morphological information about the films.

Absorpance values were obtained using a Cary5000 uv-vis spectrophotometer. The integrating sphere (DRA2500 accessory) of the setup was utilized to obtain the reflectance (R) and transmittance (T) and account for non specular scattering. Data for the TiO_2 films before and after they were sensitized using the N3 dye. Absorbtance (A) values were calculated using equation A+R+T=1. Net absorbance values, A_{dye}, due to the dye were obtained as the difference of the absorbance values of the TiO_2 films before and after being sensitized. Absorbtance values (A_λ) were derived from absorbance values obtained using $A_\lambda = \log (1/1-A_{dye})$.

Device characterization was done using standard Grätzel cell conditions (0.5 M LiI, 0.05 M I_2 in acetontrile).

4.3 Results and discussions

At low background O_2 pressures (less than 1 Pa), PLD-TiO_2/FTO films obtained are dark and non-transparent with a stoichiometry of 1Ti:(2-x)O, as verified by X-ray photoelectron spectroscopy (XPS). Films deposited at slightly higher background O_2 pressures, e.g. between 1 and 4 Pa, are very compact and transparent but with very low

porosity. Increasing background O_2 pressures above 4 Pa led to a new deposition regime where the porosity increases and the film is segmented in a collection of domains made of separated oxide columns. The domains are spaced by film fractures whose width spans a range of scales (see fig 2a) that depend upon the precise background gas pressure used during film growth. Cross-sectional views of films deposited at O_2 pressures between 8 and 16 Pa show that vertically aligned, extremely porous structures are the building blocks of the films (fig 4.5). Films fabricated with 33 Pa background O_2 pressure reach an extreme in this growth mode resulting in morphologies similar to traditional nanoparticle films although the packing of particles appears to be less dense.
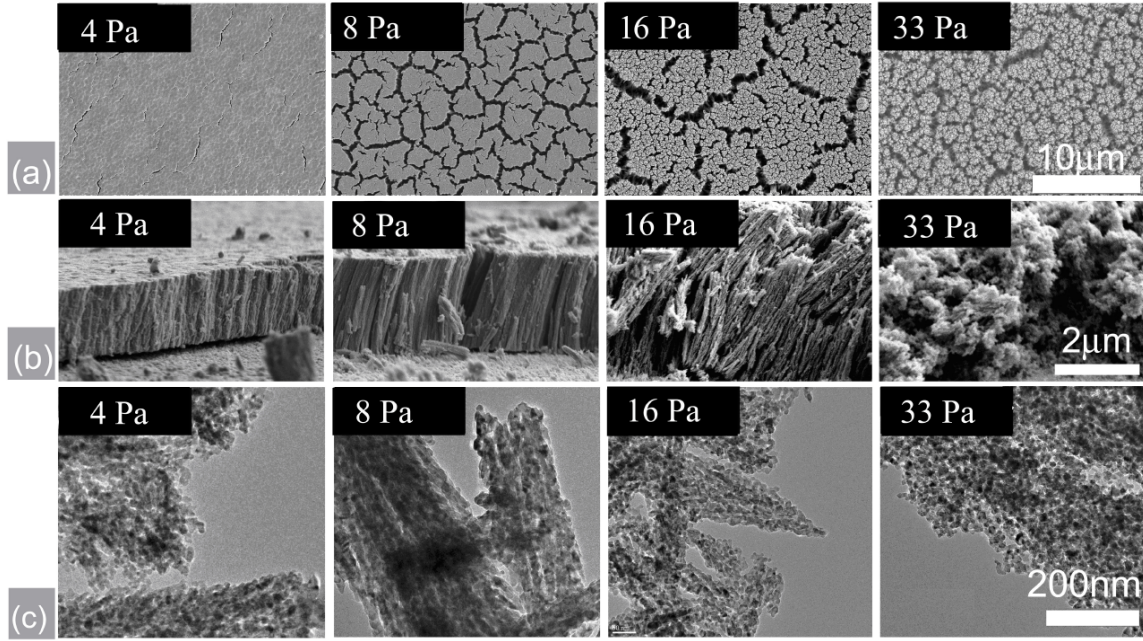
Figure 4.5: The top row shows the top view of the films using a SEM, second row shows the cross view of the same films while the third row shows TEM micrographs of the same structures.

The mechanism by which the background pressure can have such a deterministic effect on film morphology has been discussed in detail in chapter 2.

XPS analysis confirmed that the Ti:O ratio remains the same for films fabricated at background O_2 pressures between 4 and 33 Pa. For films fabricated under these

conditions, Raman scattering and X-ray diffraction analysis data verify that the PLD-synthesized TiO_2 films obtained are predominantly anatase in nature. Depending on the background O_2 pressure, the thickness of the films varied from 1.8 microns to 4.5 microns, even though a constant number of laser shots (60,000) were used during fabrication of all samples. This thickness change naturally follows from the increased void volume added in the films fabricated at higher gas pressures.
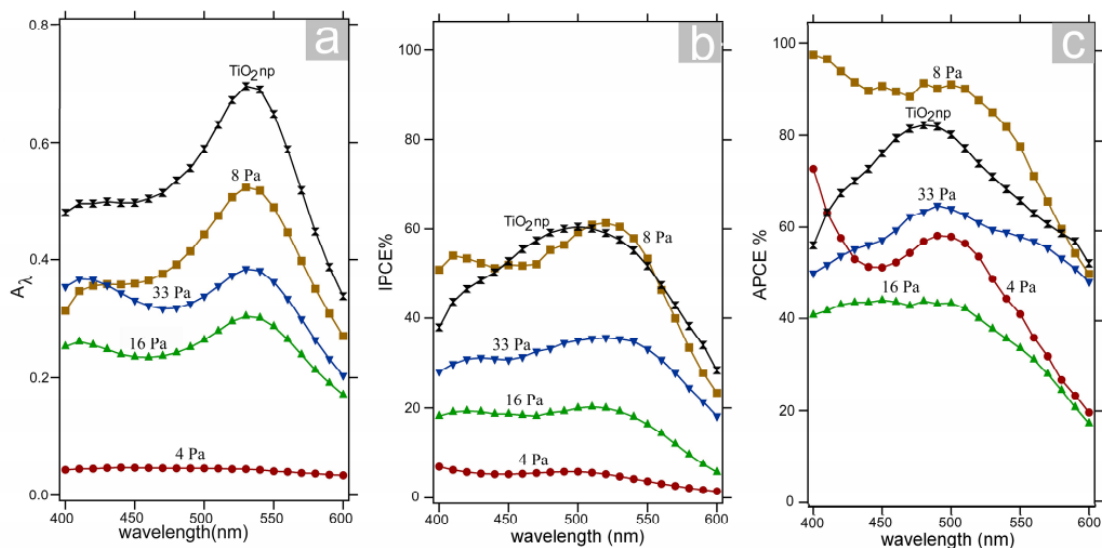
Figure 4.6: Photophysical behavior of PLD films deposited at different $P(O_2)$ compared to sol-gel films. Absorbance, IPCE and APCE values are compared.

Visible absorbance spectra for derivatized films are shown in fig 4.6(a). The extent of dye loading with O_2 pressure is not monotonic. This effect is completely reproducible and can be explained qualitatively. From fig 4.6(a) one can observe that there is negligible loading of dye for the 4 Pa film. This is expected because of the low exposed surface area of the film. The 16 Pa film follows in loading efficiency as it has the maximum number of large fractures that extend to the FTO substrate. Many have widths on the order of microns resulting in considerable wasted, transmitted light. Similar fractures appear in the 33 Pa films but the open foam-like nanoparticle structure provides an overall larger exposed surface area and higher light absorption. The 8 Pa film, which maximizes dye

loading, presents the same extended fractures to the FTO surface, however the width of these cracks are on the order of hundreds of nanometers which presumably avoids significant leaking of incident light. As a comparison (shown in figure 4.4), I fabricated a traditional sol-gel nanoparticle titania film of thickness 6.5 m. When derivatized, its light absorption was higher by only 50% compared to the 2.2 m thick 8 Pa PLD film. From the known absorbance cross section of the N3 dye molecules (1.43 x 10^7 cm ^{2} mol $^{-1}$ at 534 nm 23), the PLD 8 Pa loads 2.28 x 10^{20} molecules/cm^3 , a 2.2 x area enhancement over our nanoparticle film with loading 1.02 x 10^{20} molecules/cm^3. By comparison, the best nanoparticle films load 1.64 x 10^{20} molecules/cm^3 for a 10 m thick film absorbing 98% of light ((19)).

IPCE values for PLD-fabricated structures in fig 4.6(b) scale with absorbance as expected. Notably, IPCE values for the 6.5 m nanoparticle and 2.2 m thick 8 Pa films are comparable even though the absorbance of the former is greater by 50%. This points to an increase in electron-collection efficiency for the 8 Pa films as also shown by the APCE values near 90% in fig 4.6(c). This comparison shows that the vertical columnar structure of these films provides an improved pathway for charge transport to the conducting glass substrate, decreasing losses from random network migration.

PLD films fabricated at other pressures have less suitable nanostructures. The 33 Pa film resembles a loosely packed nanoparticle film, with a large loss of injected charges, and presents low APCE values. Much like the 8 Pa film, the 16 Pa film also consists of an array of vertical structures; however, some of these vertical structures exhibit one or more discontinuities in the form of lateral cracks which likely act as electron space traps. The 4 Pa film is functional but the compact, almost planar, structure has very little surface area for dye adsorption and the availability of continuous lateral pathways contributes to random charge transfer diffusion which further reduces its IPCE.

4.3.1 Conclusions

The combination of high surface area and improved pathways for charge injection and transfer makes structures similar to that exhibited by the PLD-TiO$_2$/FTO 8 Pa film ideal candidates for DSSC applications. There is flexibility in PLD synthesis with O$_2$ pressure, pulse energy, pulse rate, target to substrate distance, deposition temperature, number of pulses and nature of the background gas as variables. Combined with these variables is access to a large array of structures of variable thickness, porosity, grain size and crystallinity. I have observed similar structures for PLD fabricated Nb$_2$O$_5$ films and their characterization is currently in progress.

4.4 Different growing conditions and morphologies for Nb$_2$O$_5$ using pulsed laser deposition

4.4.1 Choice of photoanode material: Nb$_2$O$_5$

In the last section I showed how optimizing of structures can help in the charge transfer and therefore the overall device performance. In addition to optimizing the oxide nanostructure, the use of other metal oxides and/or doped materials with higher conduction band energies ((20),(21)) should, in principle, allow further improvement in DSSCs. This is because as long as the dye can inject electrons, enhancing the conduction band level relative to the electrolyte redox/oxidation level results in higher internal photovoltage. Nb$_2$O$_5$ is an example of one such n-type transition metal oxide with a higher conduction band edge than TiO$_2$. Jose *et al.*((20)) have recently studied the suitability of this and other metal oxides as photoanodes for DSSCs. They suggest that for a chemically-stable binary oxide like Nb$_2$O$_5$, with a higher conduction band edge than TiO$_2$, it could be possible to attain higher open circuit voltages (V$_{oc}$) and photoconversion efficien-

cies. Several groups have incorporated Nb_2O_5 in nanoparticles, nanobelts, fibers, and as coating layers for TiO_2 nanoparticles in DSSCs ((22)). I report here, for the first time, construction of a Nb_2O_5 photoanode with the nanoforest structure and the results of investigations of the photoelectronic properties of this material under a variety of key growth parameters (layer thickness, background gas pressure and composition). I find that dye loading on these structures (and thus their surface area) increases with the pressure used during deposition, allowing fine control of the porosity of the structure. This is important because electron transport is highly dependent on the geometry of the three-dimensional network of particles. Increased porosity leads to decreased average coordination number and hence a higher number of dead ends (particles with only one neighbor), changing from 1% in a 50% porous film to 31% in a 75% porous film (19). Furthermore, in addition to changing just the background oxygen pressure during deposition similar to the last section, I also used a mix of gases.

Although no significant improvement in V_{oc} was observed in the tested devices, this nanostructure presents the largest photon-to electron conversion efficiency yet observed for Nb_2O_5 as a photoanode in DSSCs, (IPCE $\geq$ 40%) with APCE 90%. In addition, this pressure-controlled structure may open a path to a marriage of the best properties of random nanoparticle networks with oriented single-crystal nanotubes and rods.

4.4.2 Experimental

Photoanodes consisting of fluorine-doped tin oxide (FTO) glass coated with Nb_2O_5 were fabricated by pulsed laser deposition(PLD) with settings similar to those mentioned in section 4.2.1 from a Nb_2O_5 target (from Kurt J Lesker, 99.9% purity). To systematically study the effect of PLD parameters on the morphological and photophysical performance of the Nb_2O_5 films, I varied oxygen pressure, partial oxygen pressure in a gas mix, and number of laser shots (which controls film thickness) with one parameter changing at a
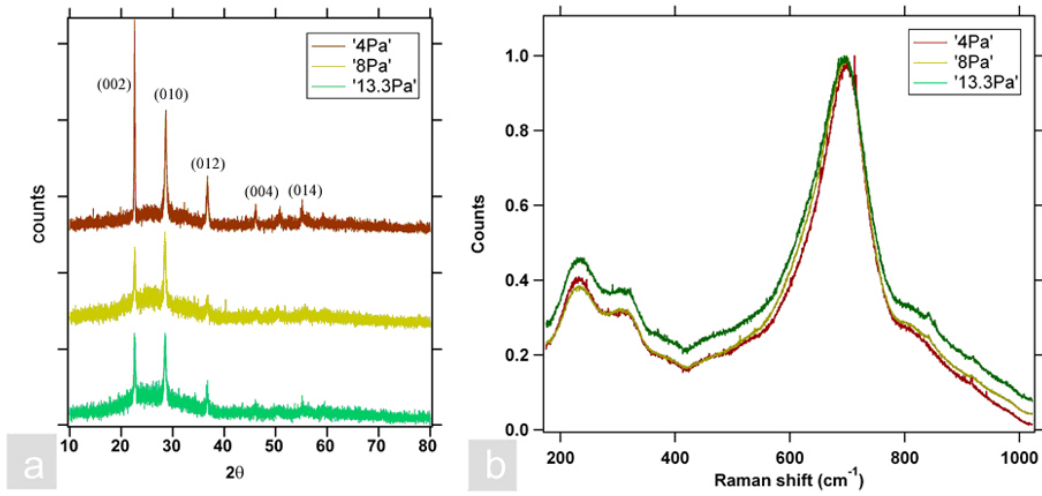
Figure 4.7: (a) X-ray diffraction and normalized (b) Raman spectra obtained for films made at different background oxygen pressures. The position and peak heights show the crystal structure (orthorhombic Nb_2O_5) of the different films grown under different gas pressures and post annealed at 500 C.

time. Because the columnar growth has been shown to be determined by the pressure of O_2 during deposition ((21)), I initially performed a pressure-variation study with a pure O_2 atmosphere. The oxygen pressure was varied from 4 to 13.3 Pa. To distinguish the pressure effect from chemical reactions involving oxygen, I varied the gas mix from pure Ar to a 1:1 mix of Ar and O_2 and again to pure oxygen. Finally, I varied the film thickness 30 nm (2k shots) to $6\mu m$ (300k shots). Following PLD growth, the films were annealed at 500 C for one hour in air.

Morphological characteristics of these amorphous films were obtained by using a Hitachi S-4700 scanning electron microscope (SEM) and a JEOL 2010F transmission electron microscope (TEM). Both top-views and cross-sectional images of the films were obtained. Raman scattering (Dilor XY Triple spectrograph, liquid nitrogen cooled CCD detector, and 514.5 nm wavelength argon ion laser at 200 mW), X-ray photoelectron spectroscopy (XPS), and X-ray diffraction (Rigaku MultiFlex X-ray Diffractometer, Cu Kα radiation, 40 kV - 40 mA, scan speed: 4 deg /min) characterizations were used to

confirm the formation of Nb_2O_5 in the orthorhombic-Nb_2O_5 phase (Figure 4.7).

Derivatization of the PLD-Nb_2O_5/FTO films was achieved by soaking them in a $2x10^{-4}$ M $Ru(dcbpyH)_2(NCS)_2$ (N3 dye) ethanol solution overnight. Surface dye loading was determined by UV visible measurements incorporating an integrating sphere (Cary 5000 fitted with DRA 2500) to collect both reflectance and transmission spectra to calculate reflectance-corrected absorbance values. To make photophysical measurements, I fabricated a sealed sandwich cell (1 cm^2) by methods described by Z-S Wang *et al.* ((23)), with a 100 μ m Surlyn$^{©}$ spacer. The redox electrolyte used was 0.1 M LiI, 0.05 M I_2, 0.6 M dimethyl propyl imidazolium iodide, and 0.5 M tert-butylpyridine in dried acetonitrile. Incident photon-to-current efficiency (IPCE) values were obtained by using a 75W Xe Oriel 6251/ Oriel Cornerstone 260 monochromator from which light was coupled through an optical fiber and made incident normal to the DSSC. Absorbed photon-to-current efficiencies (APCEs) were obtained by dividing IPCE by the fraction of light absorbed. Incident light intensity measurements were measured by using a calibrated Si-photodiode. Current measurements were conducted with a Keithley 6517A current meter. The current voltage characteristics of the cells were measured with a Keithley 2400 source meter. An AM 1.5 solar simulator (NEWPORT 1000-W Xe lamp and an AM 1.5 filter) was employed as the light source for cell efficiency characterization.

4.4.3   Results

At oxygen background pressures of less than 4 Pa the PLD Nb_2O_5/FTO films obtained are dark and nontransparent with a stoichiometry Nb_2O_{5-x}, as verified by XPS analysis (not shown). Films deposited at background oxygen pressures at and just above 4 Pa are very compact and transparent but with very low porosity. Increasing the background oxygen pressure above 4 Pa led to a new deposition regime with increased porosity and segmentation of the film into a collection of domains made of separated oxide columns.
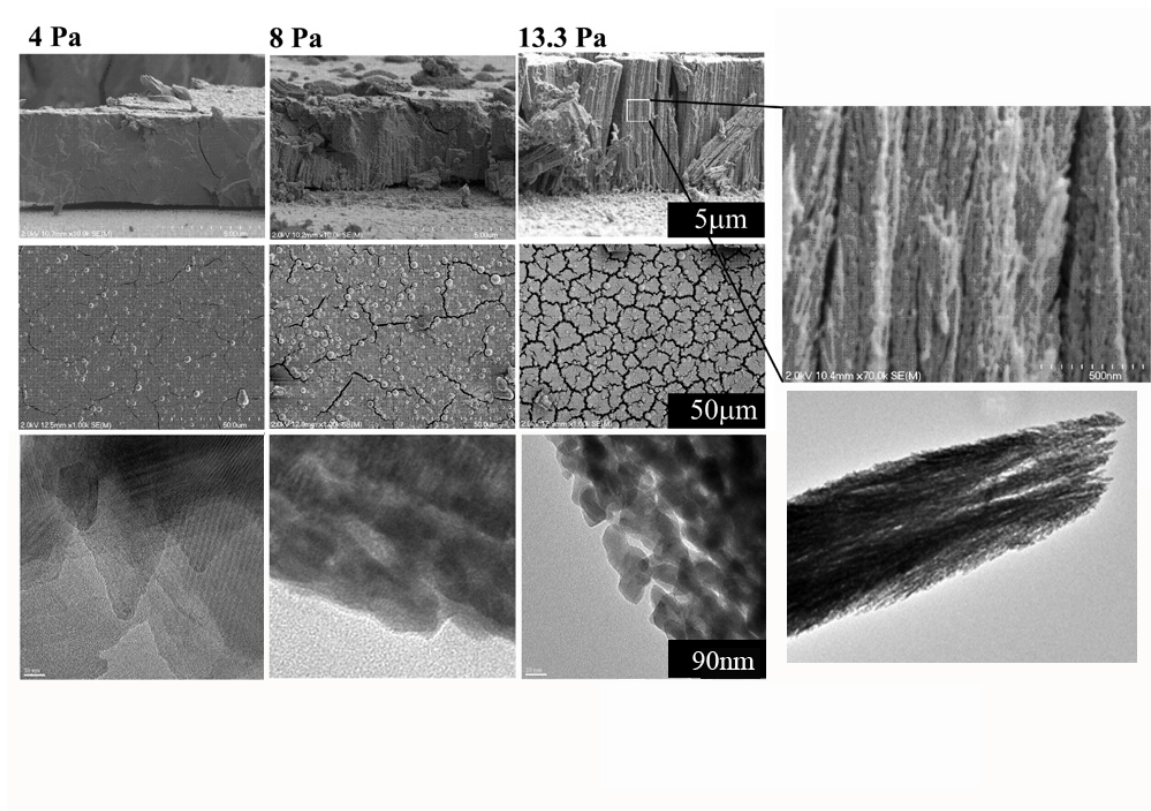
Figure 4.8: Top and cross-sectional views (SEM and TEM) of Nb_2O_5 films deposited at different background oxygen pressures.

The domains are separated by film fractures whose width spans a range of scales (see figure 4.8) that depend upon the background gas pressure used during film growth. Cross-sectional views of films deposited at oxygen pressures between 7 and 15 Pa show that vertically aligned, ordered structures are the building blocks of the films (see in particular TEM images in figure reffig:nb2o5structures). Films fabricated with higher background oxygen pressure (not shown) reach an extreme in this growth mode resulting in morphologies similar to traditional nanoparticle films with very high porosity but disordered morphology.

The photophysical behavior of the films deposited under the different background oxygen pressures is shown in figure 4.9. The light absorption due to dye loading for the 4 Pa film is very low, as expected for a compact film. At higher oxygen background

pressures, the amount of dye loading and absorbed light increase due to the presence of individual nanoparticles which enhance the exposed surface area of the film. The presence of the film cracks (top view figure 4.8) is observable at all deposition pressures. These fractures are a source of small but unwanted light scattering losses. The network of cracks could also play a role in facilitating the electrolyte diffusion, contrary to the standard nanoparticles sintered films, where the ions need to travel though tiny channels to move from the reservoir of the solution to the bottom of the oxide film. The vertically-aligned nanostructure network, which will be referred to as nanoforest, offers a network of multiscale channels from the reservoir to a very close distance to each and every dye molecule. However, although there are significant crack density differences, the APCE curves for the 8 and 13.3 Pa films (figure 4.9c) are very close to each other, suggesting their only significant dissimilarity is their dye loading capacity. The lower APCE for the 4 Pa film compared to nanoparticle- based films at higher pressures is unexpected but may be due to poor electron transport or poor injection (22) caused by film defects that are a product of growth at the edge of the parameter range for 2Nb:5O stoichiometry. Similar trends are also observed for J V characteristics, including nearly linear increases in short circuit current (J_{sc}) and overall device efficiencies with increasing background oxygen pressures. The highest V_{oc} of 710 mV and overall efficiency of 2.41% was observed for the 13.3 Pa film. These values are better((22),(23)) or comparable to those for the best niobia-based films (24) having similar area, thicknesses, and the same sensitizer.

In order to probe the full potential of the transport capabilities of these films, we varied the electrolyte to 0.5 M LiI, 0.05 M I_2 in molecular sieve dried acetonitrile. Under these conditions, the IPCE improved to 40% with $\geq$ 90% APCE, which is the highest value reported for niobia prepared by any method (figure 4.10). Koops (22) and Wu (25) observed similar photocurrent increases in TiO_2 devices with the increased concentration of Li^+ ions and absence of tert-butylpyridine, an effect which they conclude is due to
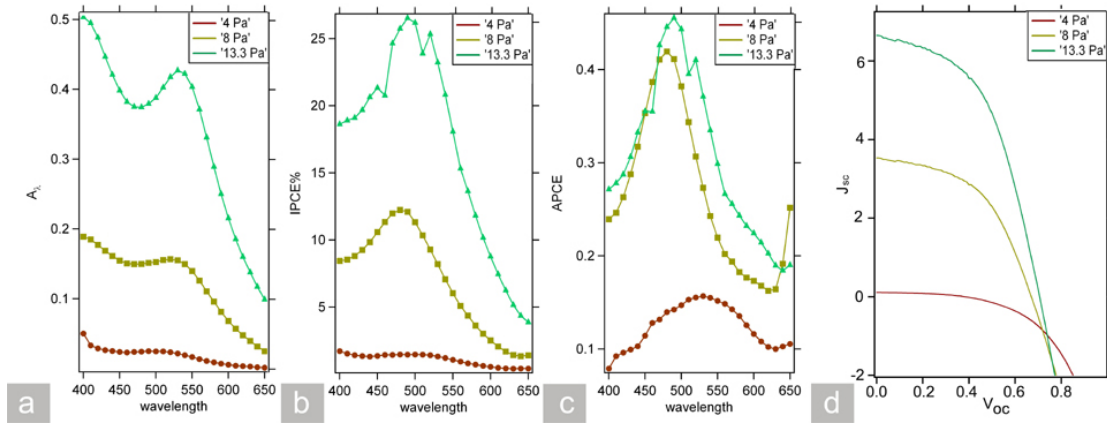
Figure 4.9: Photophysical characterization of films with N3 dye, for films deposited at different background oxygen pressures. (a) Absorbance values, (b) IPCE values, (c) APCE values, and (d) IV curves.

Parameter	4 Pa	8 Pa	13.3 Pa
Optical density at 534nm	0.02	0.15	0.46
thickness (μm)	5.1	5.2	5.9
N3 dye loading (x10^{20} molecules/cm^3)	0.017	0.130	0.328
max. IPCE value (%)	1.41	12.2	27.7
Voc (V)	0.37	0.66	0.71
Jsc (mA/cm^2)	0.106	3.53	6.65
fill factor (%)	44	50.6	49
efficiency (%) at 1 sun	0.17	1.17	2.41

Table 4.1: Device performance compared for Nb_2O_5 deposited at different $P(O_2)$.

the downward shift of the TiO_2 conduction band because of intercalation by the high charge density Li^+ ions.

To investigate the effect of gas composition on the growth of the columnar structures, the composition of the background gas was varied from pure argon to pure oxygen keeping the total background pressure constant at 10 Pa. It is obvious from the SEM micrographs shown in figure 4.11a that films prepared with no oxygen present during deposition are extremely compact and relatively crack free, similar to films grown at 4 Pa of pure oxygen. The situation is completely different in the presence of an oxygen
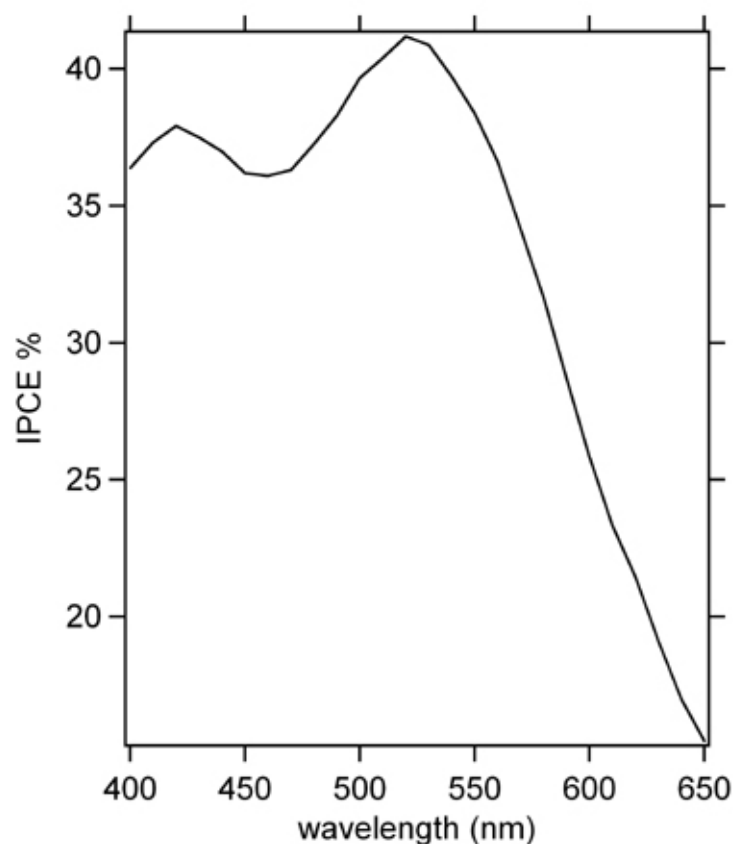
Figure 4.10: (Enhanced IPCE compared to optimal film shown in figure 4.9 due to increased Li^+ concentration for dye N3 on Nb_2O_5 in 0.5 M LiI with 0.05 M I_2. Film grown under 13.3 Pa oxygen pressure and 300k laser shots for a total 6 μm thickness.

background. Both cross-sectional and top views of films prepared in 50% Ar:50%O_2 and in pure oxygen show that those conditions result in similar crack and island dimensions, as well as columnar structures. Thus, one can conclude that some amount of background oxygen is needed to enable the forest growth, and the overall pressure required can be supplied by an inert component. After annealing in air, all traces of the background mix used during fabrication are likely to be removed and XPS studies show similar stoichiometry for all films.

Photophysical studies with the N3 dye (figure 4.11b-e) show that light absorbance, IPCE, APCE, and J V curves (all done in dried CH_3CN with 0.1M LiI, 0.05M I_2, 0.6 M dimethyl propyl imidazolium iodide, and 0.5 M tertbutylpyridine) are similar for the
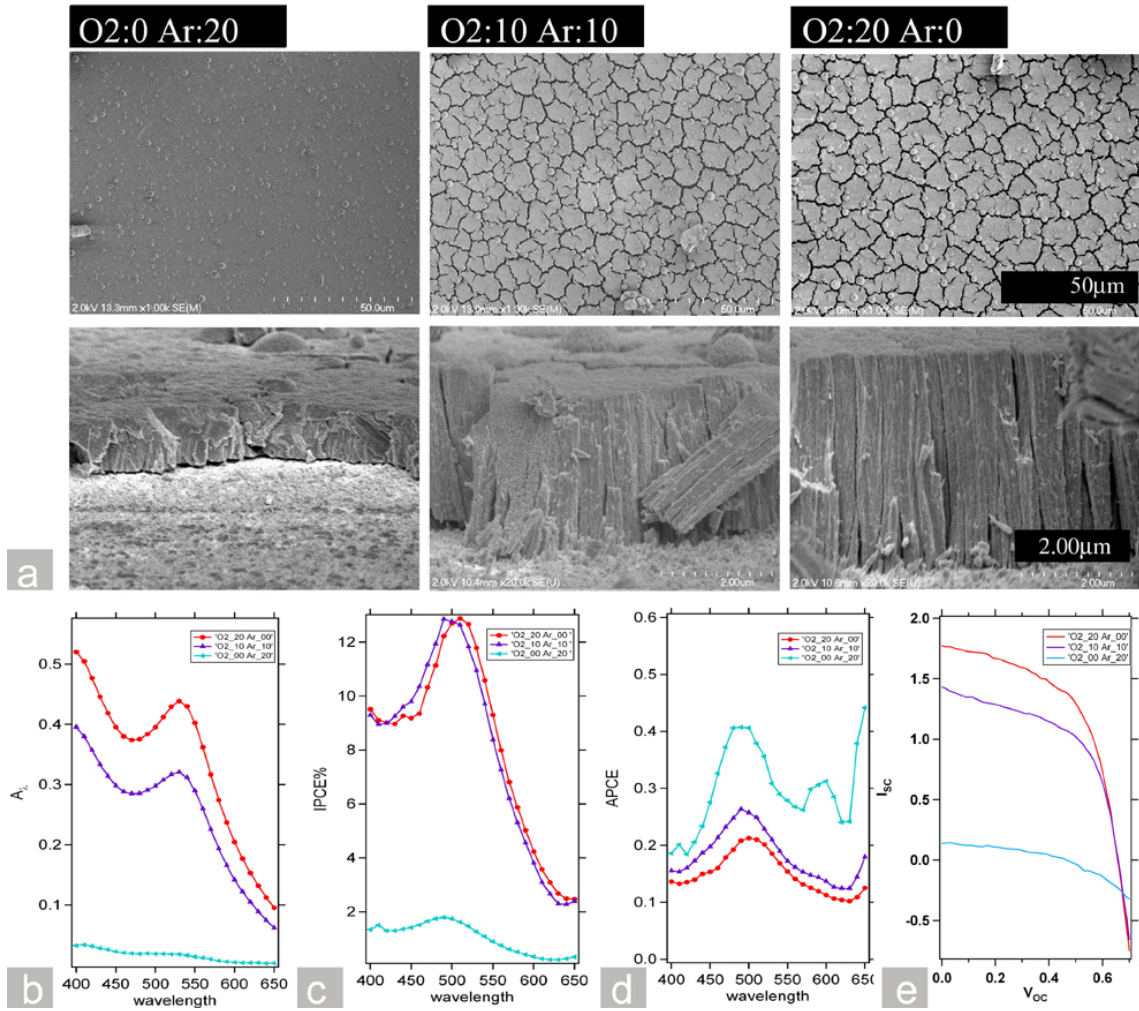
Figure 4.11: Morphological and photophysical characterization of films deposited in different gaseous environments. The plots show the behavior of pure O_2 films using red, (50:50) Ar:O_2 mix in violet and pure Ar in blue. All films were prepared with 300k laser shots at an overall 10 Pa pressure.

mixed-gas and pure-oxygen films but very different for the film made in pure Argon. These observations point to the nanostructure as the dictating factor for photophysical activity in these films.

A thickness dependence study was conducted by controlling the number of pulse shots (2k- 300k shots) used for deposition (in 13.3 Pa of pure oxygen background). Film thicknesses were varied from 40 to 6μm. The top views (figure 4.12) of films with

Parameter	pure O_2	O_2:Ar (50:50)	Ar
Optical density at 534nm	0.44	0.32	0.02
thickness (μm)	5.1	3.5	1.1
N3 dye loading ($\times 10^{20}$ molecules/cm^3)	0.363	0.385	0.077
max. IPCE value (%)	12.8	12.8	1.7
Voc (V)	0.65	0.66	0.45
Jsc (mA/cm^2)	1.76	1.43	0.14
fill factor (%)	57	54	40
efficiency (%) at 1 sun	0.65	0.51	0.02

Table 4.2: Device performance compared for Nb_2O_5 deposited at different gas mixes.

different thicknesses show differences in the bundle sizes as well as dimensions of the cracks. The widening of existing cracks, as observed in the top view, happens during annealing due to the increased stress during FTO-niobia bonding and, perhaps, due to the mismatch in thermal expansion coefficients between materials. This structural motif is similar to that observed in wetting-dewetting experiments for TiO_2 PLD grown films immersed in water and ethanol ((24)). Figure 4.13 shows that the thickness does not affect the nature of the vertical growth and the nanoforest structure appears the same independent of the number of laser shots. IPCE and JV curves are shown in figure 4.14 and they show improved device performance with increased thickness (because of higher light absorption, also shown in figure 4.14), as expected. However, we found it difficult to calculate APCE values based on the low light absorption of the thinnest films.
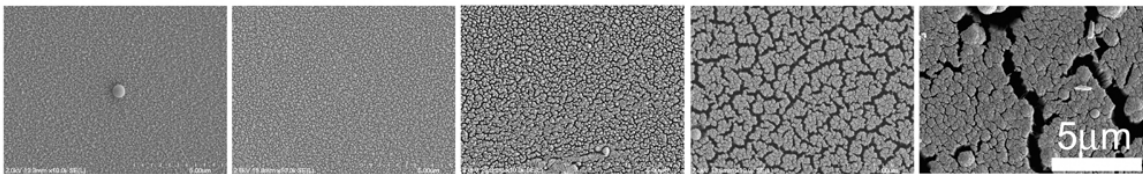
Figure 4.12: Top view of films with different thicknesses (from left to right: 2k, 10k, 20k, 60k, 300k laser shots). The increased height of the columns provides a larger torque for the increase in crack sizes.
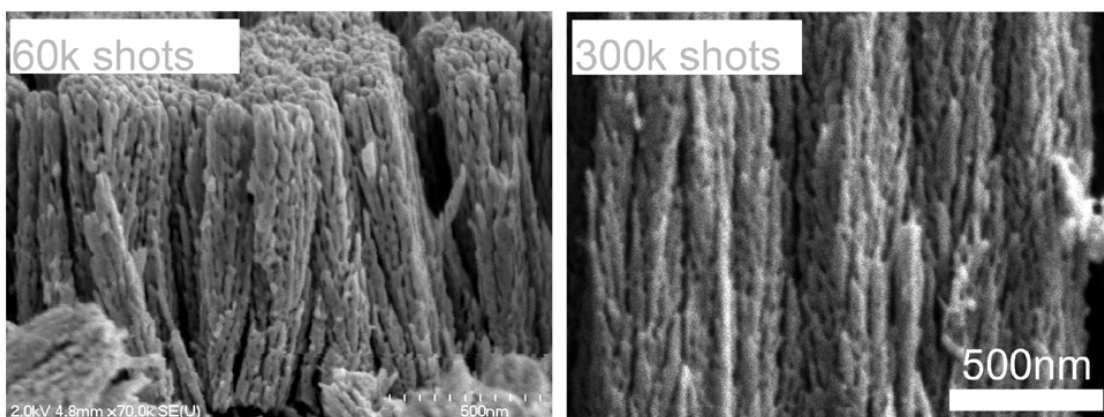
Figure 4.13: Cross-section images of films of different thicknesses controlled by the number of PLD shots. Morphology is largely thickness independent.
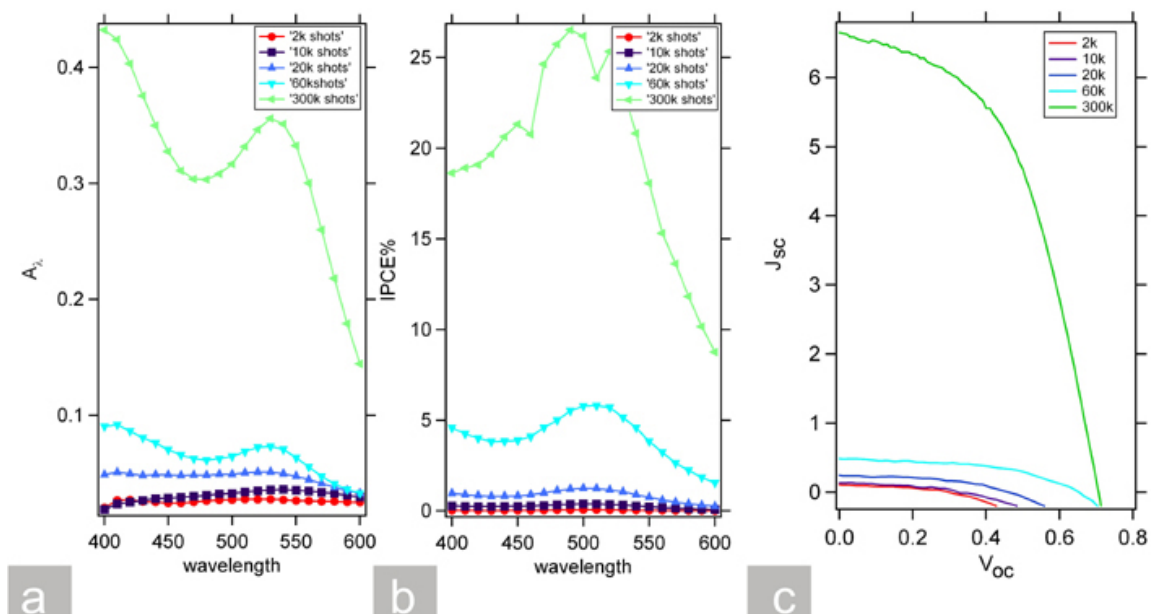
Figure 4.14: Photophysical characterization of films with different thicknesses show monotonic trends in absorbance, IPCE, and JV characteristics as function of film thickness. Films were made at 2000 (red), 10000 (violet), 20000 (deep blue), 60000 (light blue), and 300000 shots (green).

4.4.4 Conclusion

I have investigated conditions for growth of Nb_2O_5 nanoforest films by using laser ablation. Films were deposited at different background pressures, gas environments and

Parameter	300k	60k	20k	10k	2k
Optical density at 534nm	0.41	0.07	0.03	-	-
thickness (μm)	6.1	1.2	0.4	0.2	0.04
N3 dye loading (x10^{20} molecules/cm^3)	0.283	0.262	0.320	-	-
max. IPCE value (%)	25.3	5.7	1.1	0.36	0.06
Voc (V)	0.71	0.65	0.47	0.33	0.29
Jsc (mA/cm^2)	6.65	0.48	0.23	0.136	0.101
fill factor (%)	50	50	48	43	47
efficiency (%) at 1 sun	2.3	0.16	0.05	0.02	0.01

Table 4.3: Device performance compared for Nb_2O_5 deposited at different thicknesses.

with different thicknesses, and all of them have been characterized as DSSC photoanodes. Their behavior is summarized in Table 1. We found that, like Grätzels TiO_2 nanoforest, Nb_2O_5 grows in a similar vertically-aligned nanocrystalline structure under pressure-controlled pulsed laser deposition. However, this growth mode is not defined uniquely by the background pressure under deposition. We have shown that a partial pressure of oxygen is needed to develop it. Similar structures were obtained for pure oxygen and 50:50 oxygen:argon environments, both very different from films deposited in a pure argon atmosphere. The nanoparticle bundles present monotonic improvement in dye loading (4th row Table 1) and concomitant-device performance as a function of growth oxygen pressure and thickness. From the known absorbance cross section of the N3 dye molecules (1.42x10^7 cm^2 mol^{-1} at wavelength 534 nm (23)), the best PLD Nb_2O_5 films load N3 dye molecules with a 0.3 to 0.4 x 10^{20} molecules/cm^3 density, which is a factor of .75 lower than the best nanoparticle TiO_2 cell but also 1.5 times better than previously-reported Nb_2O_5 photoanodes (18,23,24). Besides some optical losses, the density and size of the film cracks do not appear to present a detrimental effect in the devices. Our results reveal the importance of pressure and gas composition during deposition. This work supports that this interesting morphology is independent to great extent of the metal oxide used. So in addition to Nb_2O_5, other oxide candidates

for photoanodes with high conduction band levels such as Ta_2O_5 and $SrTiO_3$ are likely to grow in a similar fashion, allowing their deposition in layers and doping combinations previously difficult or impossible to obtain with traditional sol gel approaches.

4.5 Comparing undoped TiO_2 and Ta doped TiO_2 grown under similar conditions

4.5.1 Choice of material: Tantalum doped TiO_2

Earlier in the chapter I tried two different methods to improve device efficiencies. In the first section we tried to use hierarchical nanostructures to improve the charge pathway. In this section we try to further improve on that work by metal doping of TiO_2 which has great promise as a means to improve V_{oc}, J_{sc} and fill factors ((25), (26)) in DSSCs. For example, significant increases in both V_{oc} ((21)) and J_{sc}((27)) have been observed upon doping TiO_2 with tantalum.

In this work we combine the best aspects of these two strategies to create hierarchical mesostructures of TiO_2 doped with tantalum (Ta-TiO_2) in an effort to improve overall device efficiency of DSSCs with the metal complex dye N719, (Di-tetrabutylammonium cis-bis(isothiocyanato)bis(2,2'-bipyridyl-4,4'-dicarboxylato)ruthenium(II)), as the chromophore.

4.5.2 Film synthesis

The Ta-TiO_2 and TiO_2 nanoforest photoanodes were obtained by pulsed laser ablation from their corresponding metal oxide targets, in similar ways to those mentioned in the last two sections. The consistency, reproducibility and thickness control of films grown by laser ablation is a significant advantage of the pulsed laser deposition system

compared to traditional sol gel techniques. Additionally, the similar growth rates for TiO_2 and Ta-doped TiO_2 ($1.7\mu m$ for every 100,000 shots) allow us the liberty of using exactly the same growth conditions to obtain structurally-identical films. Four different film thicknesses for both Ta-TiO_2 and TiO_2 were obtained by changing the total number of laser pulses (100k, 200k, 400k, 800k shots).

Both TiO_2 and Ta-TiO_2 were derivatized with N719 using the "hot slide" technique in which the films were heated to 500 C for 30 minutes immediately prior to derivatization by the complex. The films were submerged in 0.3 mM N719 dye in acetontrile:tert-butanol (1:1) solution overnight.

Dye-sensitized sandwich cells based on the N719 derivatized photoanodes were constructed following the procedures described by Z-S Wang *et al.* (17), with a Pt coated FTO counter and a 25 μm Surlyn$^{©}$ spacer. The redox electrolyte for device measurments was 0.05 M LiI, 0.03 M I_2, 1 M dimethyl propyl imidazolium iodide, 0.1 M guanidinium thiocyanate and 0.5 M tert-butylpyridine in dried acetonitrile: valeronitrile (85:15) (v:v).

4.5.3 Characterization

SEM and TEM characterization of the films were done using procedures similar to that mentioned in section 4.4.2. In addition scanning TEM (STEM) mode using a JEOL 2010F-FasTEM using 200kV accelerating voltage was also done. Elemental mapping was done using STEM mode using INCA EnergyTEM 250 TEM microanalysis system with imaging capabilities.

Chemical composition and metal oxidation states of the Ta-doped TiO_2 were obtained using x-ray photoelectron spectroscopy (XPS) on a Thermo K-alpha system using an Al-Kα monochromated source.

Absorbance measurements were done using an integrating sphere with a center mount. White light was coupled through an optical fiber and made incident on the

film. The light not absorbed was coupled out of the sphere and measured using a spectrometer.

The setup used for the IPCE measurement was the same as that described in section 4.4.2. The current-voltage characteristics and electrochemical impedance spectroscopy measurements as well as open Circuit Voltage Decay measurements were done using a Gamry500 potentiostat using Gamry Framework. An AM1.5 1 sun solar simulator (NEWPORT 1000-W Xe lamp and an AM1.5 filter) was employed as the light source for cell irradiation.

4.5.4 Results

As demonstrated earlier ((13)), the metal oxide films grown using laser ablation under background oxygen pressure present a forest-like vertically aligned nanostructure. Scanning and transmission electron microscope images of such nanoforest are shown in figure 4.15. The average particle size, found by analyzing TEM micrographs, is approximately 15 nm in diameter.

The chemical composition and electronic structure of Ta-TiO_2 were obtained by using x-ray photoelectron spectroscopy (XPS) (figure 4.15 e). The presence of the Ta 4f peak confirms the presence of Ta^{5+} in the sample. The atomic concentration of Ta, from XPS analysis, of the Ta-TiO_2 film (0.9%) is in good agreement with the concentration of the PLD target (1%). Elemental mapping, using STEM, indicates that Ta doping is uniform throughout the Ta-TiO_2 network (figure 4.15c, 4.15d).

The current-density voltage curves for Ta-TiO_2 and TiO_2 devices for films grown from 800,000 shots (13.6 μm) can be seen in figure 4.16b. The Ta-TiO_2 samples exhibit improved photocurrent in J_{sc} (15.9 mA/cm^2) over the undoped films (J_{sc} = 9.67 mA/cm^2). The trend toward larger J_{sc} for Ta-TiO_2 over TiO_2 was consistent for all film thicknesses tested. The significantly higher J_{sc} combined with only a small decrease in
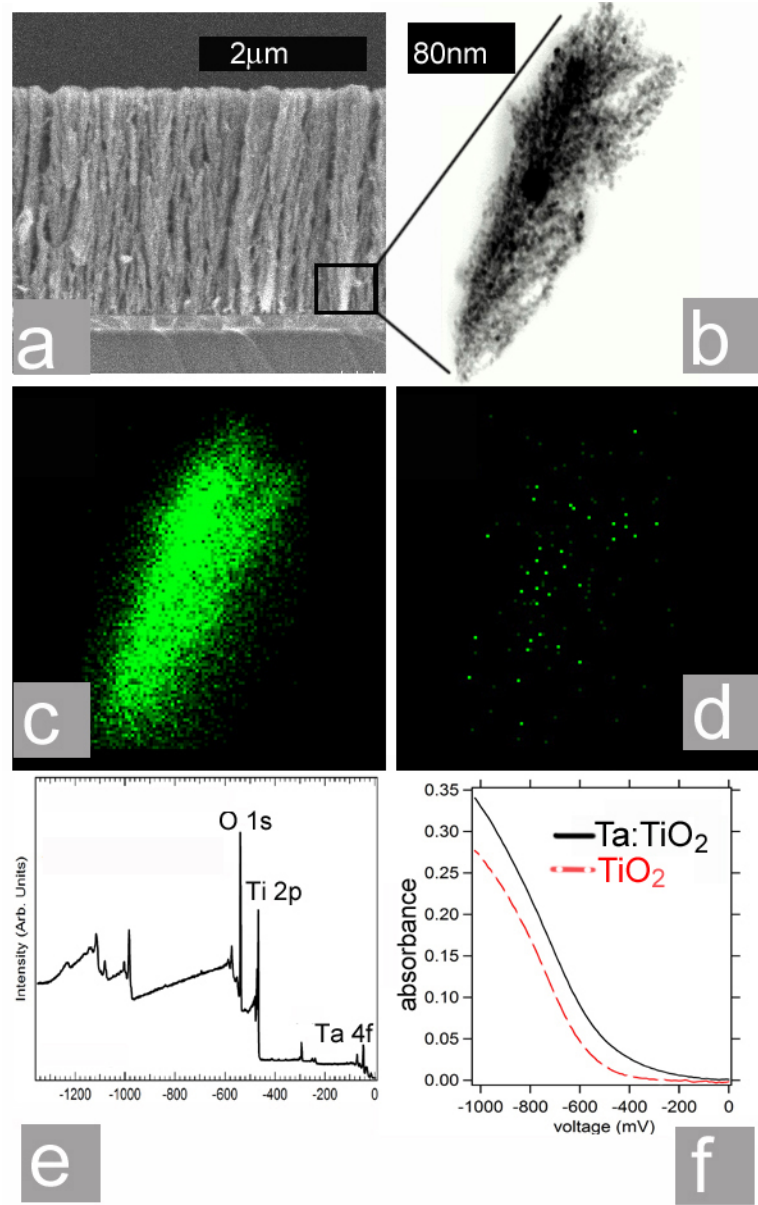
Figure 4.15: (a) Cross-sectional SEM showing nanoforest structure in Ta-TiO$_2$, (b) TEM of region close to seed of the nanostalk, (c) and (d) shows elemental mapping for Ti and Ta respectively, (e) XPS plot for Ta-TiO$_2$ film, (f) Spectral electrochemistry plot shows lower conduction band of Ta-TiO$_2$

V$_{oc}$($\sim$ 50 mV) upon doping with tantalum leads to a much-improved overall efficiency for the Ta-TiO$_2$ devices (6.69%) as compared to undoped TiO2 devices (4.9%). These trends are similar over a range of thicknesses as shown in figure 4.16 d and Table 4.4.

Parameters	TiO$_2$				Ta-TiO$_2$			
	800k	400k	200k	100k	800k	400k	200k	100k
number of laser pulses	800k	400k	200k	100k	800k	400k	200k	100k
film thickness (μ)	13.5	6.7	3.4	1.7	13.4	6.8	3.4	1.7
V$_{oc}$ (mV)	720	720	710	680	690	670	690	710
J$_{sc}$ (mA/cm^2)	9.6	6	1.9	0.7	15.9	10.4	5.1	1.7
Fill factor	.7	.68	.7	.61	.61	.58	.64	.55
Efficiency	4.8	2.9	.96	.32	6.7	3.9	2.2	.7
Dye loading(10^{-7}mol/cm^2)	.55	.42	.18	.09	.58	.44	.18	.07
J$_{sc}$/ Dye loading(mA/10^{-7}mol)	17.4	14.2	10.5	7.7	27.4	23.6	28.3	24.2

Table 4.4: Device performance comparison between devices made with undoped TiO$_2$ and Ta-TiO$_2$ electrodes.

4.5.5 Discussion

To rationalize the basis for the improved device performance of Ta-TiO$_2$ over TiO$_2$ it is important to evaluate the device components and processes in a step-wise manner. The first step in the operation of the DSSC is light absorption by the chromophore. Since dye adsorption on the films is comparable (figure 4.16a) regardless of tantalum doping, it can be concluded that difference in light absorption by the dye is not contributing to the difference in device behavior.

Once the dye absorbs a photon, the second step in the process is injection of electrons from the excited chromophore into the conduction band of the metal oxide electrodes. The driving force for electron injection is the energy difference between the excited state reduction potential for the chromophore ($E_{1/2}(Ru^{III/II^*})$) and the conduction band (CB) edge of the metal oxide. Noticeable positive shifts ($\sim$75 mV) in the CB of our Ta-TiO$_2$ samples over undoped TiO$_2$ are observed by spectral electrochemistry (figure 4.15 f). This increased driving force may enhance electron injection yields (16).

Once injected, the electrons in the conduction band can either travel through the porous network of nanoparticles to the FTO electrode or recombine. Insight into both of these processes can be obtained by using electrochemical impedance spectroscopy (EIS). The results of these measurements can be seen in the Nyquist (figure 4.17a) and Bode
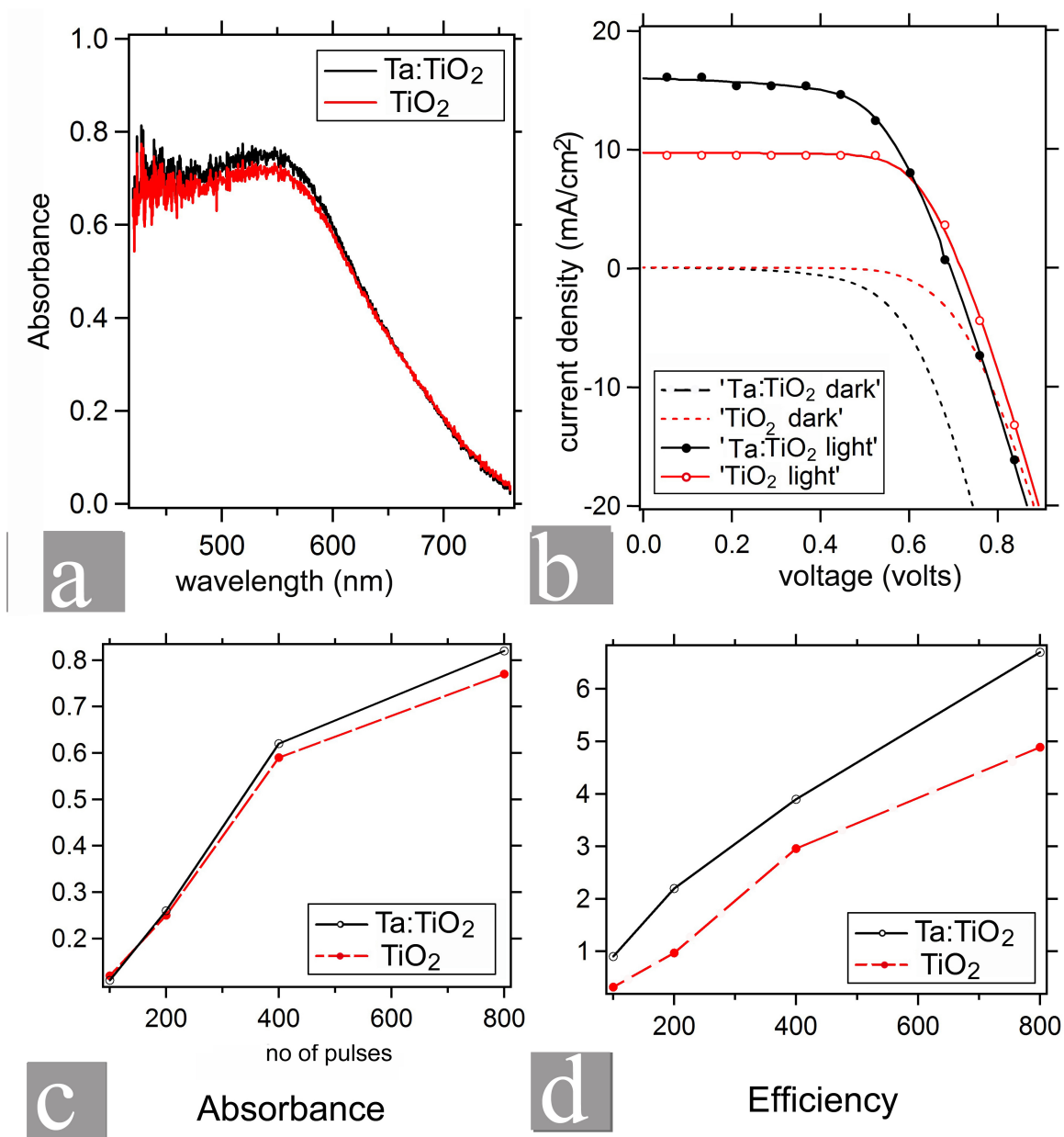
Figure 4.16: The top panel shows comparative studies of (a) Absorbance and (b) voltage - current density plots for TiO_2 and $Ta:TiO_2$ for thickest films, the bottom panel shows (c) Absorbance and (c) Efficiency comparisons between TiO_2 and $Ta:TiO_2$ for different film thicknesses.

plots (figure 4.17b). In the Nyquist plot the diameter of the central arcs for $Ta-TiO_2$ and TiO_2 are comparable, indicating similar resistances for both porous networks. However
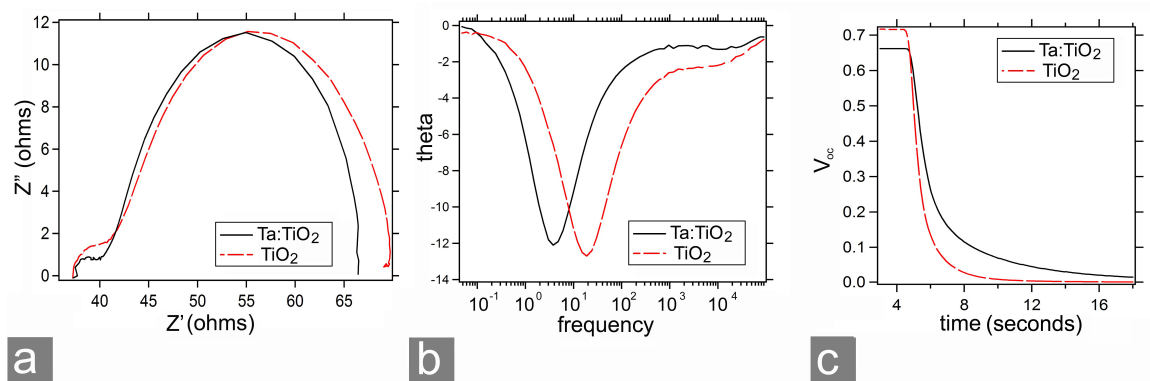
Figure 4.17: Nyquist, Bode and open circuit voltage decay plots of Ta:TiO$_2$ compared to TiO$_2$.The first plot shows the larger concentration of electrons in the conduction band for Ta:TiO$_2$ while the slower recombination rate of Ta:TiO$_2$ is evident from the Bode and OCVD plots.

the frequencies of the peak maxima for these arcs, which is more clearly depicted in the Bode plot (figure 4.17b), dissimilar. According to Adachi *et al.* (18) the frequency at the maximum corresponds to the effective rate constant (k$_{eff}$) at which diffusing electrons are lost due to recombination. The lower k$_{eff}$ noted for our Ta-TiO$_2$ samples (3.7 s^{-1}) compared to undoped TiO$_2$ (19 s^{-1}) points to a slower recombination rate and, therefore, a larger concentration of electrons in the metal oxide film.

Support for the difference in recombination rates is obtained from the open circuit voltage decay measurement (OCVD). The open circuit voltage is a measurement of the quasi-Fermi level, which is dictated by the density of electrons in the conduction band. In the OCVD measurement, the change in V$_{oc}$ is monitored in the dark, after a period of illumination. In this dark state there is a loss of photoelectrons and reduction in the V$_{oc}$ due to electron recombination processes. The slower OCVD for Ta-TiO$_2$ compared to TiO$_2$ supports the conclusions from EIS (Figue 4.17 c).

There are several trends in DSSC performance emanating from the thickness of the metal oxide films (Table 4.4). As expected, J$_{sc}$ and efficiency for both TiO$_2$ and Ta-TiO$_2$ films increase with film thickness presumably due to increased absorbance and the
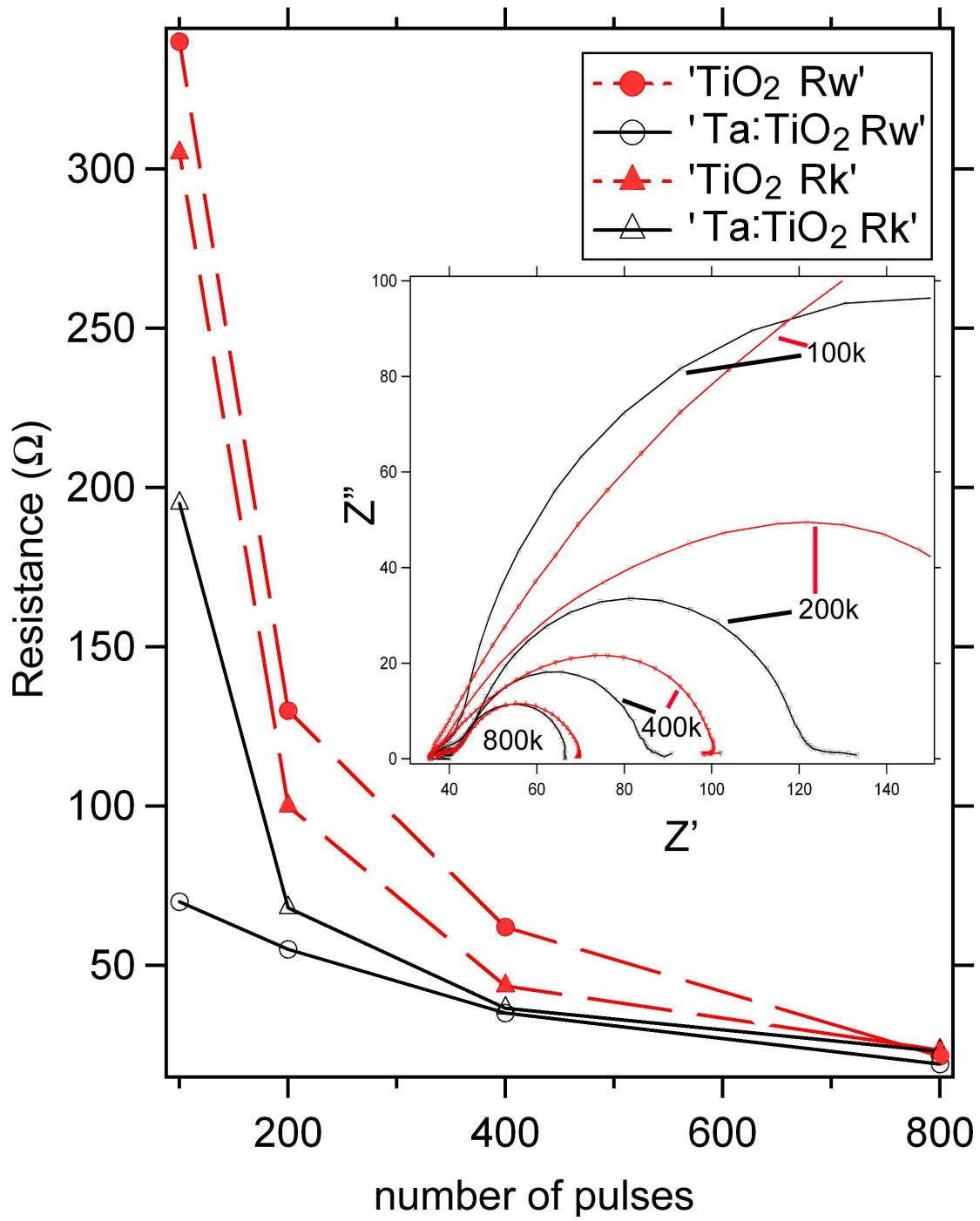
Figure 4.18: Comparing TiO_2 and $Ta:TiO_2$ fitted transmission line components showing different resistances through device components. R_w is the resistance through the nanoparticle network, while R_k is the resistance to charges traveling from the nanoparticle into the electrolyte.

corresponding increase in the number of injected electrons. From table 4.4 we further note that the dye loading and therefore the absorbance are very similar for TiO_2 and Ta: TiO_2 for all thicknesses. The short circuit current (J_{sc}) per mole of dye loaded can be used as a measure of charge collection efficiencies (11). Over all thicknesses, we see a lower J_{sc} per dye loading for TiO_2 compared to Ta: TiO_2. This further points to a better charge transfer pathway for the Ta:TiO_2 than TiO_2. It is also interesting to note that for TiO_2 there is a monotonic improvement of this factor with increase in thickness (7.7 to 17.5), while for Ta: TiO_2 it is more uniform (26 +/- 3) over all thicknesses as well as much higher than that of TiO_2. This points to better charge transfer for thicker TiO_2 films while the pathways for Ta: TiO_2 are much improved even at much lesser thicknesses.

Considering that carrier gradients responsible for the J_{sc} can only be built with strong light absorption and suitable diffusion and recombination characteristics, these thickness differences can be understood considering that the Ta-TiO_2 films have reduced recombination rates and an increase in electron concentration in combination with the light-absorbing capability corresponding to each film thickness. Ta:TiO_2 films with moderate absorptions do well because of their superior transport properties. In contrast, the weaker transport properties of the non-doped TiO_2 results in poor J_{sc} until the light absorption capability becomes quite significant. The improvements in the diffusion parameters can actually be related to an increased film conductivity. This argument is supported by EIS measurements as function of thickness and the corresponding Nyquist plots (figure 4.18). There is a larger increase in the arc diameters for undoped TiO_2 as the thickness increases compared to the Ta-TiO_2 films. The two important parameters from the Nyquist plots are R_w and R_k (resistance through the network and resistance in back electron transfer) are fitted and shown in figure 4.18. Because of the increased electron concentration in Ta-doped TiO_2, both resistances are decreased. However, at

smaller thicknesses the difference in R_w is much larger than the differences in R_k which accounts for the lesser improvement of J_{sc} per dye loading with thickness for TiO_2.

Of the many factors contributing to DSSC performance, the positive shift of the conduction band of TiO_2 due to M^+ doping appears to play a major role. Liu, Lu ((27), (28))and this report have noted a positive shift of the conduction band of TiO_2 when doped with Ta^{5+} or Nb^{5+}, as well as, increased photocurrents. The positive shift in the conduction band increases the driving force for excited-state injection into the metal oxide and reduces the back-electron transfer rate. Device performance is also improved due to the increased electron concentration and weaker recombination constants in Ta-TiO_2, thus resulting in overall larger photocurrents.

In conclusion, I have fabricated Ta doped TiO_2 based DSSCs using pulsed laser deposition. The Ta-TiO_2 devices exhibit higher photocurrents without significant drop in open circuit voltage compared to those for undoped TiO_2. The increased J_{sc} values combined with a nominal decrease in V_{oc} results in over 60% improvement in overall device efficiencies for tantulum-doped films compared to undoped TiO_2. The enhanced performance is attributed to a combination of increased electron concentration and reduced electron recombination.

References

1. O'regan, B. and Gratzel, M. (1991) A low-cost, high-efficiency solar cell based on dye-sensitized colloidal TiO$_2$ films. Nature **353**, 737–740

2. Chen, C., Wang, M., Li, J., Pootrakulchote, N., Alibabaei, L., Ngoc-Le, C., Decoppet, J., Tsai, J., Gratzel, C., Wu, C., et al. (2009) Highly efficient light-harvesting ruthenium sensitizer for thin-film dye-sensitized solar cells. ACS nano **3**, 3103–3109

3. J Frank, A., Kopidakis, N., and Lagemaat, J. (2004) Electrons in nanostructured TiO$_2$ solar cells: transport, recombination and photovoltaic properties. Coordination Chemistry Reviews **248**, 1165–1179

4. Wei, D. (2010) Dye sensitized solar cells. International Journal of Molecular Sciences **11**, 1103–1113

5. Nakade, S., Saito, Y., Kubo, W., Kitamura, T., Wada, Y., and Yanagida, S. (2003) Influence of tio$_2$ nanoparticle size on electron diffusion and recombination in dye-sensitized TiO$_2$ solar cells. The Journal of Physical Chemistry B **107**, 8607–8611

6. O'Regan, B., Moser, J., Anderson, M., and Graetzel, M. (1990) Vectorial electron injection into transparent semiconductor membranes and electric field effects on the dynamics of light-induced charge separation. Journal of Physical Chemistry **94**, 8720–8726

7. Soedergren, S., Hagfeldt, A., Olsson, J., and Lindquist, S. (1994) Theoretical models for the action spectrum and the current-voltage characteristics of microporous semiconductor films in photoelectrochemical cells. The Journal of Physical Chemistry **98**, 5552–5556

8. Nakade, S., Kubo, W., Saito, Y., Kanzaki, T., Kitamura, T., Wada, Y., and Yanagida, S. (2003) Influence of measurement conditions on electron diffusion in nanoporous TiO$_2$ films: Effects of bias light and dye adsorption. The Journal of Physical Chemistry B **107**, 14244–14248

9. Leng, W., Barnes, P., Juozapavicius, M., ORegan, B., and Durrant, J. (2010) Electron diffusion length in mesoporous nanocrystalline TiO$_2$ photoelectrodes during water oxidation. The Journal of Physical Chemistry Letters **1**, 967–972

10. Law, M., Greene, L., Johnson, J., Saykally, R., and Yang, P. (2005) Nanowire dye-sensitized solar cells. Nature Materials **4**, 455–459

11. Snaith, H. and Schmidt-Mende, L. (2007) Advances in liquid-electrolyte and solid-state dye-sensitized solar cells. Advanced Materials **19**, 3187–3200

12. Boucle, J., Snaith, H., and Greenham, N. (2010) Simple approach to hybrid polymer/porous metal oxide solar cells from solution-processed ZnO nanocrystals. The Journal of Physical Chemistry C **114**, 3664–3674

13. Sauvage, F., Di Fonzo, F., Li Bassi, A., Casari, C., Russo, V., Divitini, G., Ducati, C., Bottani, C., Comte, P., and Graetzel, M. (2010) Hierarchical TiO$_2$ photoanode for dye-sensitized solar cells. Nano letters **10**, 2562–2567

14. Walczak, M., Oujja, M., Marco, J., Sanz, M., and Castillejo, M. (2008) Pulsed laser deposition of TiO$_2$: diagnostic of the plume and characterization of nanostructured deposits. Applied Physics A: Materials Science & Processing **93**, 735–740

15. Walczak, M., Papadopoulou, E., Sanz, M., Manousaki, A., Marco, J., and Castillejo, M. (2009) Structural and morphological characterization of TiO$_2$ nanostructured films grown by nanosecond pulsed laser deposition. Applied Surface Science **255**, 5267–5270

16. Sanz, M., Walczak, M., Oujja, M., Cuesta, A., and Castillejo, M. (2009) Nanosecond pulsed laser deposition of TiO$_2$: nanostructure and morphology of deposits and plasma diagnosis. Thin Solid Films **517**, 6546–6552

17. Sanz, M., Walczak, M., de Nalda, R., Oujja, M., Marco, J., Rodriguez, J., Izquierdo, J., Bañares, L., and Castillejo, M. (2009) Femtosecond pulsed laser deposition of nanostructured TiO$_2$ films. Applied Surface Science **255**, 5206–5210

18. Vo Thi, T., Rouet, J., Brault, P., Bauchire, J., Cordier, S., and Josserand, C. (2008) A continuous non-linear shadowing model of columnar growth. Journal

of Physics D: Applied Physics **41**, 022003

19. Nazeeruddin, M., Kay, A., Miiller, E., Liska, P., Vlachopoulos, N., Gratzel, M., et al. (1993) Conversion of light to electricity by scn- on nanocrystalline TiO_2 electrodes. Journal of the American Chemical Society **115**, 6382–6390

20. Jose, R., Thavasi, V., and Ramakrishna, S. (2009) Metal oxides for dye-sensitized solar cells. Journal of the American Ceramic Society **92**, 289–301

21. Feng, X., Shankar, K., Paulose, M., and Grimes, C. (2009) Tantalum-doped titanium dioxide nanowire arrays for dye-sensitized solar cells with high open-circuit voltage. Angewandte Chemie **121**, 8239–8242

22. Le Viet, A., Jose, R., Reddy, M., Chowdari, B., and Ramakrishna, S. (2010) Nb_2O_5 photoelectrodes for dye-sensitized solar cells: Choice of the polymorph. The Journal of Physical Chemistry C

23. Wang, Z., Kawauchi, H., Kashima, T., and Arakawa, H. (2004) Significant influence of TiO_2 photoelectrode morphology on the energy conversion efficiency of N719 dye-sensitized solar cell. Coordination chemistry reviews **248**, 1381–1389

24. Fusi, M., Di Fonzo, F., Casari, C., Maccallini, E., Caruso, T., Agostino, R., Bottani, C., and Li Bassi, A. (2011) Island organization of TiO_2 hierarchical nanostructures induced by surface wetting and drying. Langmuir

25. Chandiran, A., Sauvage, F., Casas-Cabanas, M., Comte, P., Zakeeruddin, S., and Graetzel, M. (2010) Doping a TiO_2 photoanode with Nb^{5+} to enhance transparency and charge collection efficiency in dye-sensitized solar cells. The Journal of Physical Chemistry C

26. Zhang, X., Liu, F., Huang, Q., Zhou, G., and Wang, Z. (2011) Dye-sensitized W-doped TiO_2 solar cells with tunable conduction band and suppressed charge recombination. The Journal of Physical Chemistry C

27. Liu, J., Yang, H., Tan, W., Zhou, X., and Lin, Y. (2010) Photovoltaic performance improvement of dye-sensitized solar cells based on tantalum-doped TiO_2 thin films. Electrochimica Acta **56**, 396–400

28. Lu, X., Mou, X., Wu, J., Zhang, D., Zhang, L., Huang, F., Xu, F., and Huang, S. (2010) Improved-performance dye-sensitized solar cells using Nb-doped TiO$_2$ electrodes: Efficient electron injection and transfer. Advanced Functional Materials **20**, 509–515

Chapter 5

Other applications of pulsed laser deposited thin films

5.1 Introduction

Being able to tailor thin film structures opens up many possible applications using a single deposition system. In the last chapter I concentrated on the vertically-aligned nanostructures that were especially suited for DSSCs. In this chapter I focus on other possible structures and applications. In the first section I use extremely uniform, compact, thin (~ 8 nm) films for band edge measurements of metal oxides. In the following section I use the other extreme and explore the efficiency of PLD-fabricated porous structures as gas sensors.

5.2 Measurement of energy bands of metal oxides

One of the main factors influencing the performance of DSSCs is the relative energy band positions of the metal oxides with respect to the dye. A material with a higher conduction band will be able to produce a higher open circuit voltage as long as the electrons from the dye-LUMO can inject into the conduction band. Therefore both choice of metal oxides and design of dyes require knowledge of the position of the energy levels.

In order to be able to make these measurements I utilize a combined direct (XPS and UPS) and inverse photoemission (IPS) spectroscopy study (schematic of methods shown in figure 5.1), performed in a single ultra-high-vacuum (UHV) chamber. Explanations of the experimental setup, procedures and results are as follows.
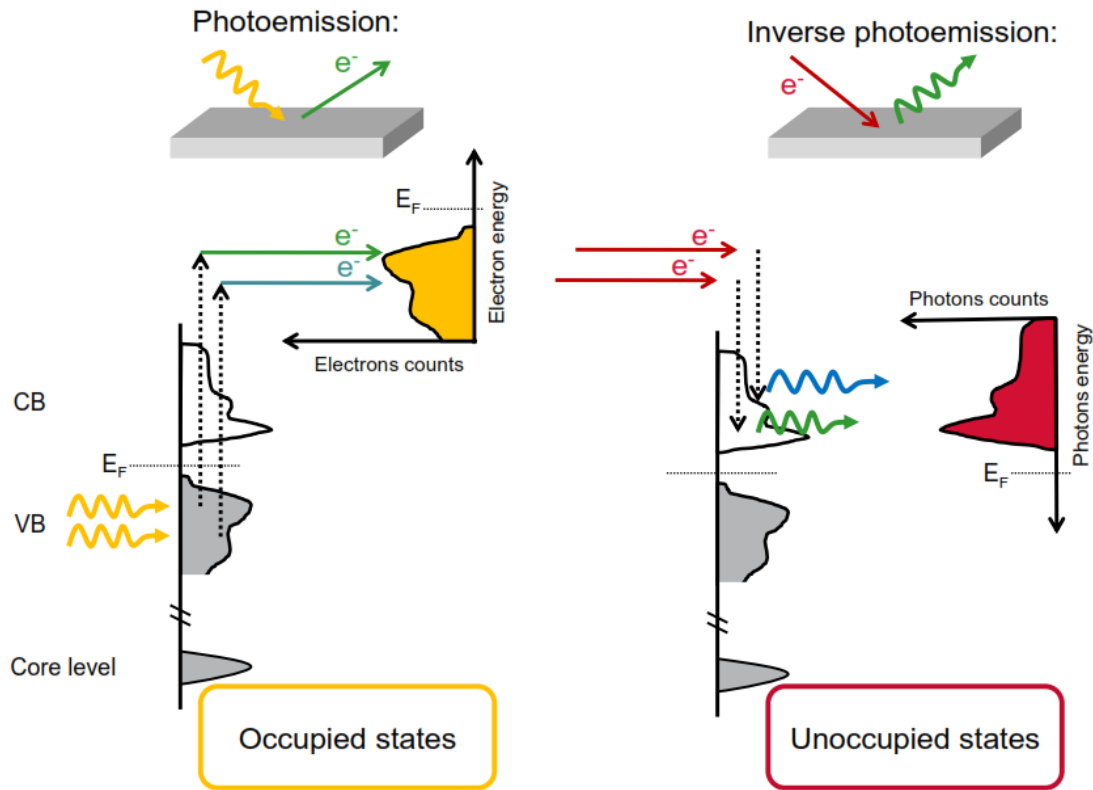
Figure 5.1: Schematic figures of photoemission and inverse photoemission processes used for XPS, UPS and IPS techniques.

5.2.1 Experimental

PLD fabrication of continuous thin films

Thin films of the metal oxides on 1cm^2 indium doped tin oxide (ITO) substrates were fabricated by pulsed laser deposition(PLD) settings mentioned in section 4.2.1. Prior to deposition, the PLD chamber was evacuated to a base pressure of 6 x 10^{-6} Torr. During

deposition background oxygen pressure inside the chamber of 10mTorr was maintained with a flow rate of 5sccm. All films were made with 2k pulses.

Spectroscopic methods

The spectroscopic measurements presented here were obtained using a single ultrahigh vacuum experimental chamber that housed instrumentation for x-ray and ultraviolet photoemission spectroscopies (XPS and UPS) as well as inverse photoemission spectroscopy (IPS). The base pressure of the chamber was less than $5\text{x}10^{-10}$Torr. Valence band photoelectrons were excited using a Leybold-Heraeus helium discharge photon source (HeII: 40.8 eV) and core levels were probed using the non-monochromatized Al Kα line of a SPECS XR50 dual anode source. The energy analysis of the emitted electrons was performed in an angle-integrated mode using a double pass Phi 15-255G cylindrical mirror analyzer (CMA). The axes of the photon sources and the CMA formed a 90º angle and the sample normal was oriented midway between the two.

Inverse photoemission spectra were obtained using a grating spectrometer, which was mounted in the same experimental chamber. A well-collimated, monoenergetic electron beam (of incident kinetic energy E = 20.3 eV) was directed towards the sample along the surface normal. The electrons couple to high-lying unoccupied states and a subset of them relax via a direct optical transition to low-lying unoccupied states in the conduction band, emitting a photon in the process. The photons were dispersed by a concave spherical diffraction grating and detected by a microchannel plate with a position sensitive resistive anode encoder. With this approach, the intensity of photons as a function of photon energy reflects the density of unoccupied states in the conduction band. In the photoemission and inverse photoemission spectra, the valence band maximum (VBM) and the conduction band minimum (CBM) are both measured with respect to the Fermi level of a gold sample in contact with the samples. The overall energy resolutions for

the UPS and IPS spectra are estimated to be 0.3 eV and 0.6 eV respectively.

The IPS measurements presented in this work have been taken while keeping a small sample current (0.5-1μA) for a beam size of 1 mm^{2}and by sampling several spots on a large 1 cm^2 sample with short beam exposure (3-10 min). For such electron doses, no beam damage was observed during IPS nor in subsequent UPS and XPS spectra.

5.2.2 Results and Discussions

Stoichiometry and core levels

In order to characterize both the stoichiometry and the electronic structure of the thin oxide films, chosen core levels and valence bands spectra have been measured for each sample using incident Al-Kα radiation. Although it is possible to find core levels information for these oxides in the literature, the valence band measured at this energy is rarely found.
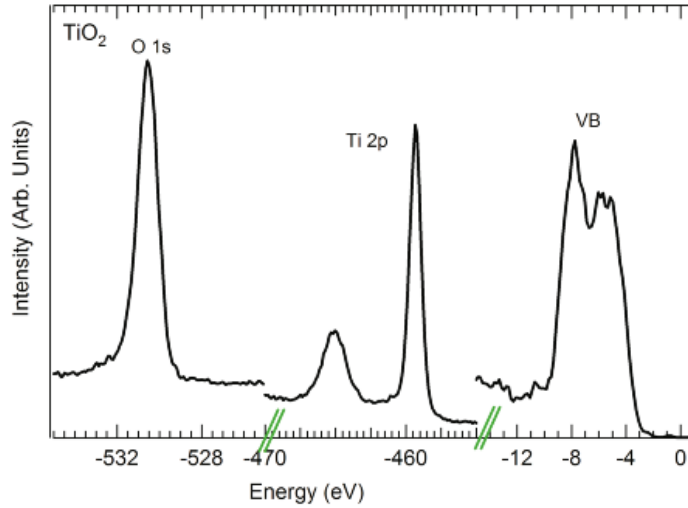

Figure 5.2: O 1s and Ti 2p core levels and valence band spectra measured on a TiO$_2$ thin film.

The TiO$_2$ thin film had the expected stoichiometry and the O 1s and Ti 2p$_{3/2}$ core
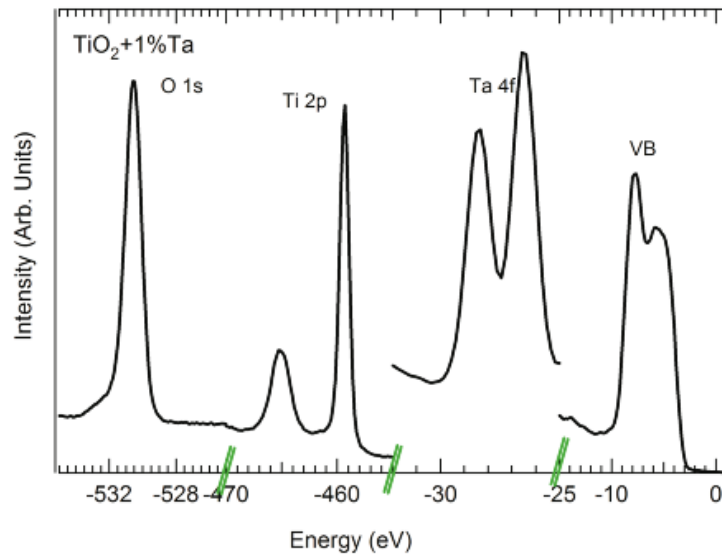
Figure 5.3: O 1s, Ti 2p and Ta 4f core levels and valence band spectra measured on a Ta doped TiO$_2$ thin film.

Figure 5.4: O 1s and Nb 3d core levels and valence band spectra measured on a Nb$_2$O$_5$ thin film.

levels (shown figure 5.2) were found respectively at -530.6 eV and -459.3 eV. The doping level of the Ta-doped TiO$_2$ was found to be 1%. Similar to what was found for TiO$_2$, the O 1s and Ti 2p core levels were found at -530.5 eV and -459.2 eV respectively, and
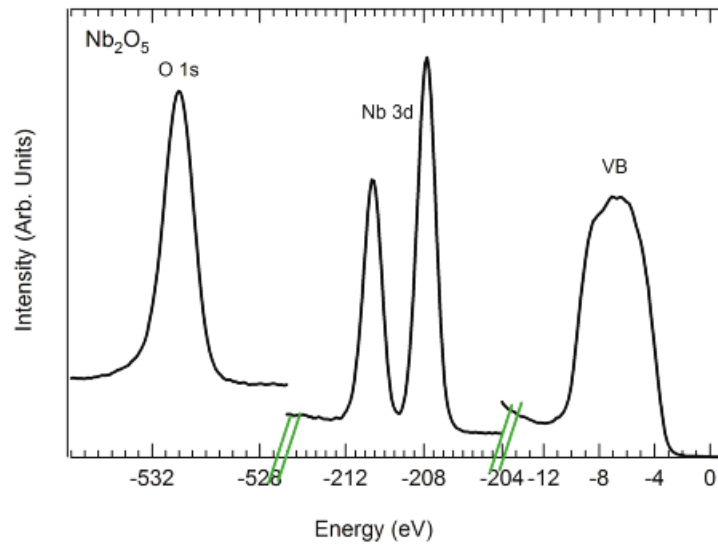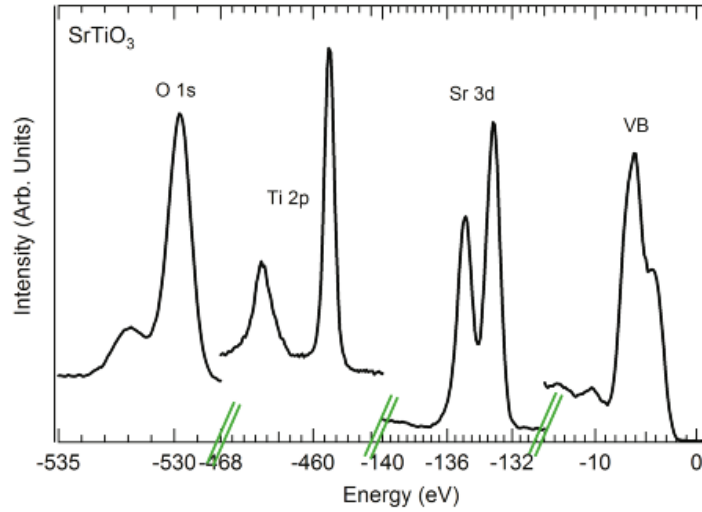
Figure 5.5: O 1s, Ti 2p and Sr 3d core levels and valence band spectra measured on a SrTiO$_3$ thin film.

the Ta 4fp$_{7/2}$ core level was found at -26.5 eV.

The Nb$_2$O$_5$ film had the expected stoichiometry with the O 1s and Nb 3d$_{5/2}$ core levels were found at 531.0 eV and 210.7 eV respectively. The SrTiO$_3$ sample was found to be slightly Sr rich with a final composition of Sr$_{1.5}$TiO$_3$.

Energy gap and electron affinity

The valence band and conduction band spectra of the oxides thin films, measured using UPS and IPS respectively, are shown in figure 5.6. As the energy scale is referenced to the Fermi level of the system (set at zero), the valence bands and conduction bands spectra are characterized respectively by a negative energy scale and a positive energy scale. The band gap of each oxide is determined using a using a linear fit of the band edges to the background of the spectra (indicated by the green lines).

The valence band of these oxides is mostly composed of O 2p states. After annealing at 200 C for 1 hour in UHV, some OH was still present at the surface of the oxides leading to a small contribution to the spectra around -11 eV (indicated by *). The
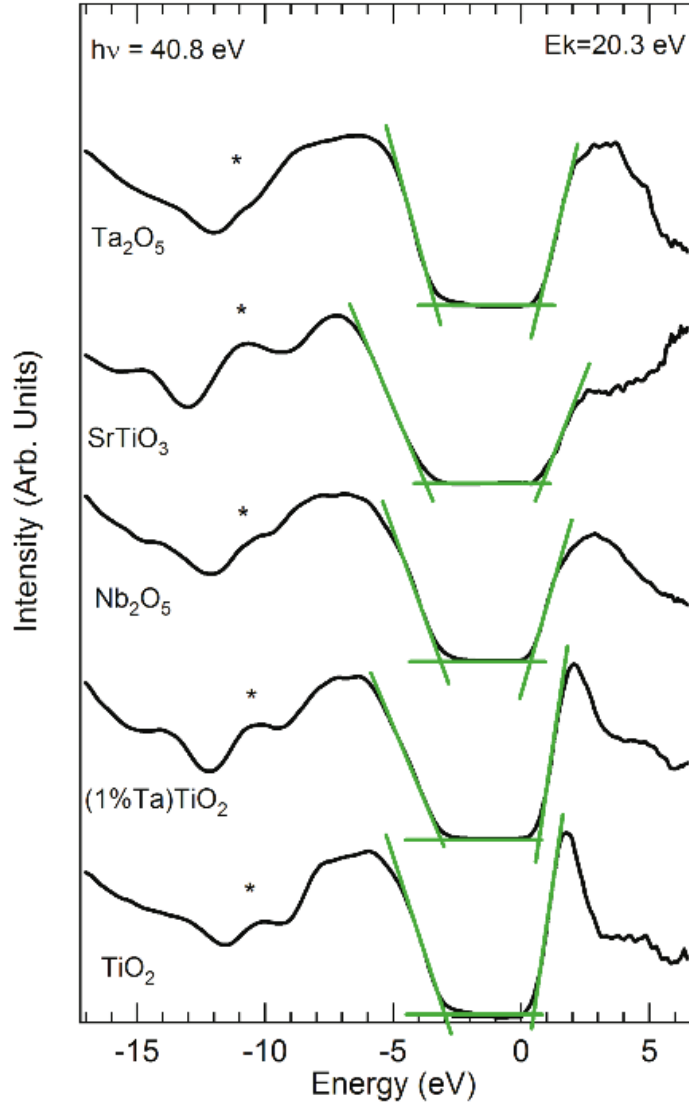
Figure 5.6: Valence band spectra measured in UPS (energy <0) and conduction band spectra measured in IPS (energy >0) of the different oxides. The energy scale is referenced to the Fermi level of the system. The energy band gap of the oxides is deduced using a linear fit of the valence and conduction band edges to the background of the spectra.

valence band edges positions are reported in table 5.1. The conduction bands of TiO_2 and Ta-doped TiO_2 are composed of narrow Ti 3d states, characterized by a large cross section in IPS at this energy, and are found between 0.5 and 3 eV. The conduction bands of Nb_2O_5 and Ta_2O_5 are dominated by Ta 5d and Nb 4d states respectively. The

conduction band edge of $SrTiO_3$ is delimited by Ti 3d states leading to a band edge found at 0.7 eV. Above 4 eV, Sr 4d states are visible.

Sample	VB edge	CB edge	E_{gap}	EA
TiO_2	-3.0	+0.5	-3.5	3.4
Ta-TiO_2	-3.1	+0.6	3.7	3.5
Nb_2O_5	-3.1	+0.4	3.5	3.5
$SrTiO_3$	-3.7	+0.7	4.4	2.6
Ta_2O_5	-3.1	+0.8	3.9	3.9

Table 5.1: Band edges positions with respect to the Fermi level, and electron affinity measured for the oxides thin films. All numbers are in eV.

Electron affinity (EA) measurements have also been performed using the He I UV source with a -5 V bias on the sample. The total width of the spectrum, W, is extracted using a linear extrapolation of the data to the background intensity level at both the high- and low kinetic-energy ends of the spectrum. The electron affinity is then obtained as EA = $h\nu$-W-E_{gap}, where $h\nu$ is the photon source energy and E_{gap} is the experimentally measured gap of the oxide films. The corresponding values are reported in Table 5.1.

5.3 WO_3 as gas sensor

The ion coloration properties of tungsten trioxide have been the subject of thorough investigation for electrochromic applications since Deb's seminal paper ([1]). There has been a rise in interest in WO_3 gasochromic coloration due to its response to H_2 gas ([2], [3]). In a typical gasochromic device H_2 is dissociated into H ions by a thin catalyst film (Pd or Pt) on top of the WO_3 layer. Bleaching is accomplished by exposing the film to air or oxygen.

The coloration change is believed to be the result of the double injection of electrons and H^+ ions, however the details of the coloration mechanism remain controversial ([4], [5]). Given their simple bi-layer structure, these gasochromic devices are prime

candidates for large-area solar control windows and for optically-based hydrogen sensors ((4),(6),(7), (8), (9)). Work on optical hydrogen sensors has been prompted by the development of hydrogen as a carrier and storage medium of energy. Optical monitoring of hydrogen is a better method due to its safe nature compared to techniques requiring electrical measurements, especially in environments where the H_2air mixture might reach explosive potential.

Although WO_3 gasochromic windows have been demonstrated to switch thousands of times under closed conditions ((4)), when films are exposed to air they have a very limited lifetime ((2)). In order to use WO_3 in gasochromic H_2 sensors, it is essential to overcome its air poisoning problem and to characterize the optical contrast achievable under H_2 exposure. In this section I present a model that connects the changes in the optical constants of WO_3 with H_2 partial pressure using the Langmuir adsorption equation ((10)). This establishes the limits in WO_3 atmospheric gasochromic coloration to 57.9% of the electrochromic ion injection. I also show that air poisoning is alleviated by coating with polydimethylsiloxane (PDMS) which extends the life of the device without adversely affecting its H_2 sensitivity. A mechanism behind this positive effect is proposed.

5.3.1 Experimental

WO_3 films were fabricated by pulsed laser deposition (PLD) from a 99.98% pure compressed target $WO_{2.9}$ using laser settings mentioned in section 4.2.1. The plume obtained was then simultaneously deposited on Si, glass and graphite substrates. Magnetron sputtering was used to deposit a catalytic Pt layer ($\sim$ 5 nm) only on films to be used in gasochromic experiments. To optimize the film stoichiometry I varied the partial oxygen pressure inside the PLD chamber from high vacuum to 13.3 Pa. Prior to deposition, the PLD chamber was evacuated to a base pressure of 8×10^{-4} Pa. All experiments were

performed at room temperature using 20,000 pulses for a film thickness of 250270 nm as verified by spectroscopic ellipsometry.

The oxygen-to-tungsten ratios (O/W) of the different films were obtained using Rutherford backscattering spectroscopy (RBS). RBS was performed on the WO_x films deposited on clean graphite substrates (He^+ at 1.7 MeV, 170 backscattered angle). As can be seen in Fig. 5.7, oxygen pressures of less than 2.67 Pa yielded O/W ratios that were too low (<3) while pressures between 5.33 and 6.67 Pa yielded correct stoichiometries. I found that with O_2 pressures above 6.67 Pa the O/W ratios declined.
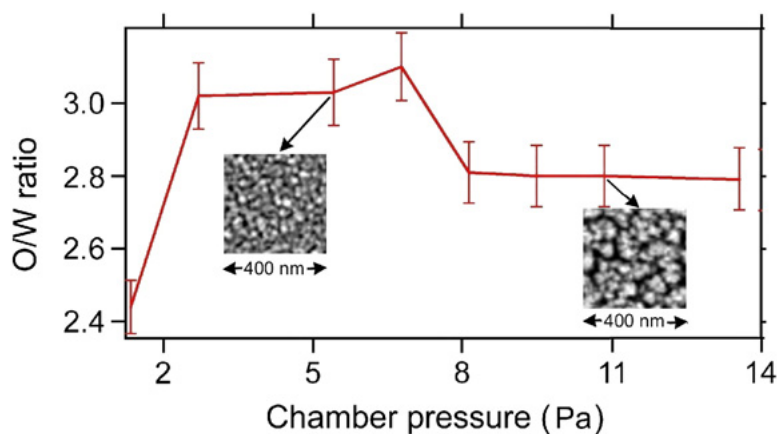
Figure 5.7: Stoichiometric ratio of WO_3 films deposited at different oxygen pressures.

The morphological characteristics of these amorphous films were obtained using a Hitachi S-4700 scanning electron microscope (SEM) operated at an accelerating voltage of 2 kV and a Veeco Explorer atomic force microscope (AFM) operating with a cantilever tip Olympus 240TS 70 kHz in tapping mode. The films presented a columnar structure from surface to substrate for oxygen pressures greater than 2.67 Pa. AFM analysis demonstrated a 10 nm rms surface roughness at the top (not shown in figures). Films produced under oxygen pressures higher than 6.67 Pa showed increasing porosity as observed from the SEM micrographs (insets in figure 5.7).

The optical transmittance of the films at different wavelengths (400 to 900 nm)

was studied in the colored state (after films were exposed to one atmosphere of 2%
H_2 (in Ar)). The optical transmittance for the bleached films (films exposed to one
atmosphere of O_2) was also measured. A typical normalized transmission curve for a
freshly-prepared sample versus time is shown as a solid line in Fig. 5.8. As expected
from the RBS findings, films fabricated with 6.67 Pa background O_2 pressure presented
the largest optical transmission contrast between the colored and bleached states. Films
deposited outside the 5.336.67 Pa range of oxygen pressures did not show any significant
gasochromic effect.
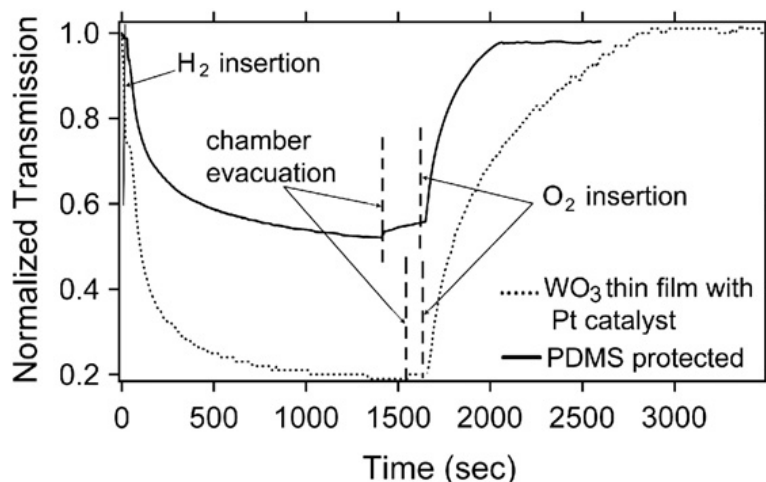
Figure 5.8: Change in WO_3 thin film transmission upon exposure to H_2. The figure
shows the drop in transmission with the introduction of H_2 in the chamber. The trans-
mission increases with the introduction of O_2 in the chamber.

5.3.2   Results and Discussions

In order for WO_3 thin films to be suitable candidates for optical H_2 sensing devices it is
necessary to obtain the limiting values of the optical changes due to hydrogen exposure.
In electrochromic devices, the relationship between changes in optical constants to the
injected charges is readily available. Reversing this intrinsic connection, the achievable
H^+ concentration can be obtained from the resulting optical constants at a given H_2

partial pressure. Although optical constants relating to electrochromic changes are readily available [11], analogous data for gasochromic change have not been reported. The frequency-dependent complex refractive index (n+ik) was obtained in the colored and bleached states via spectroscopic ellipsometry (400 to 900 nm) at incident angles of 45 and 70 degrees. The tungsten oxide layer was modeled using a general oscillator function composed of three Lorentz oscillators. The initial reference parameters of the fit were approximate optical constants in the bleached state obtained from a Cauchy model of tungsten oxide on Si. The thin Pt layer and the roughness of the film, as observed in the AFM analysis, were incorporated into the model as a Bruggeman effective medium consisting in part of WO_3 (coupled to the general oscillator layer), Pt, and air (void). The computed thicknesses agreed with prior data taken on individual components that had been deposited on Si. The standard mean squared errors (MSE) of both fits (bleached and colored state) were 3.1 and 1.0, respectively. Fig. 5.9 presents the results of the complex optical constants in both states.
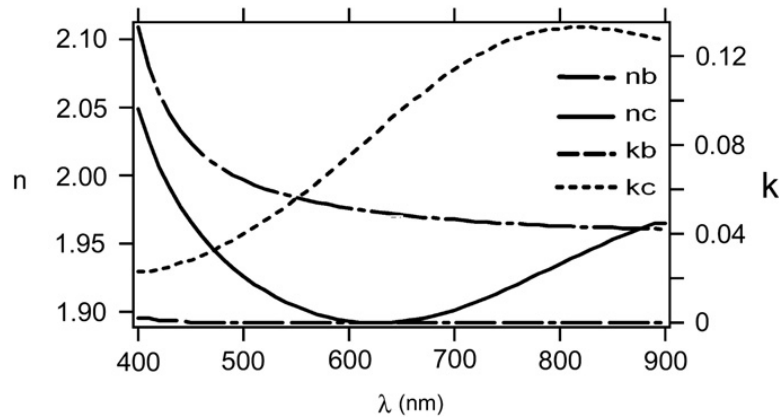
Figure 5.9: Optical constants of WO_3 in the colored and bleached states.

Remarkably, the optical constants obtained on exposure to 2% H_2:Ar gas matched almost perfectly those obtained by direct Li ion injection with a 15 $\mu C/cm^2 \mu m^{-1}$ charge density ((11)) (correlation coefficient=0.99). This fact can be used to find a quantitative relationship between charge density and partial pressure of H_2. It has been established by

Lundstrom ((10)) that the Langmuir adsorption equation can relate surface adsorption coverage and ion concentration in the volume of thin films to such partial pressures. For our experimental conditions the Langmuir equation may be written as below:

$$\delta\varepsilon_s = \delta\varepsilon_{max}(\frac{\alpha(T)P(H_2)}{1 + \alpha(T)P(H_2)})$$

where $\delta\varepsilon_s$ stands for the ion concentration corresponding to a partial pressure, $P(H_2)$ in the chamber, $\delta\varepsilon_{max}$ stands for the maximum ion concentration possible in the thin film. Given the concentration I infer from ellipsometric measurements with one atmosphere 2% H_2:Ar and the maximum concentration attainable ((12)) ($\delta\varepsilon_{max} = 91.5mC/cm^2$ μm^{-1}), the value of α is set to be 4.33 x $10^3 Pa^{1/2}$ at room temperature. This value of α is a relatively large Langmuir constant that translates to a rapid rise in ion concentration with $P(H_2)$, predicting high sensitivity for low hydrogen pressures. However, this estimated value of α also means that the Langmuir curve saturates quickly. Even one atmosphere of pure H_2 could only achieve 57.9% of the maximum concentration reachable by field ion injection, seriously limiting the change in optical constants that can be achieved using the H_2 gasochromic effect.

The Langmuir equation also highlights the fact that the coloration is directly proportional to the number of available adsorption sites. Hence the presence of pollutants that reduce the number of adsorption sites drastically limits the practicality of WO_3 films as H_2 sensors. The effects of poisoning have been shown to be considerably reduced if samples are stored in vacuum or Ar atmosphere ((13)), however this defeats the purpose of using the films as gas detectors. In order to overcome this problem, I tested a protective PDMS coating in our gasochromic devices. PDMS was chosen as the protective layer because of its well-known capability of encapsulation and permeability to all common atmospheric gases.

Four Pt-coated WO_3 films (A, B, C, and D) were prepared using the method de-

scribed earlier in section 5.3.1. Samples C and D were additionally covered with thin films of PDMS. In order to encapsulate sample C, a PDMS layer was preparing by adding 2.5 g of the silicone elastomer base (from SYLGARD 184 silicone elastomer kit) to 0.5 g of the curing agent and 31 g of n-Hexane (Fisher Scientific). The resulting mixture was then spin-coated on the sample for 150s at 8000 rpm, followed by curing for an hour at 80 C. This resulted in a PDMS film thickness of 862 nm (ellipsometric measurement). Sample D was coated using the same procedure but with a different amount of the starting material. For PDMS coating of sample D, 5 g of the elastomer base was added to 0.5 g of the curing agent and 138.5 g of n-Hexane to produce a polymer film thickness of 181 nm. The four samples were then subjected to a coloration/bleaching cycle over an extended period of time. For each cycle the bleached and colored transmissions were measured at $\lambda = 720$ nm. The ratio of those measurements defines the coloration contrast (Tcolored/Tbleached). Change in coloration contrast over time is the indicator of air poisoning and/or aging. The film was stored in rough vacuum ($\sim 10^{-3}$ Torr) between cycles. Films B, C and D were left exposed to air between coloration and bleaching cycles.

Fig. 5.10 shows the coloration contrast curves for the PDMS coated and control samples. Although the initial performance of films A and B is significantly better (larger coloration contrast) compared to films with a protective layer, they are poisoned rapidly. After several days, the rate of poisoning slows down in the unprotected films, but they continue to age. In contrast, films C and D do not seem to age at all over a ten day period. Note that the thickness of the PDMS layer itself does not play a significant role on the efficiency of the film. In addition, the kinetics of the PDMS coating cycle are not retarded by the protective layer (Fig. 5.8). The coloration contrast was lower (worse performance) than that of fresh films. This is probably due to the air exposure during the time lapse between Pt: WO_3 deposition and PDMS spin coating. However,

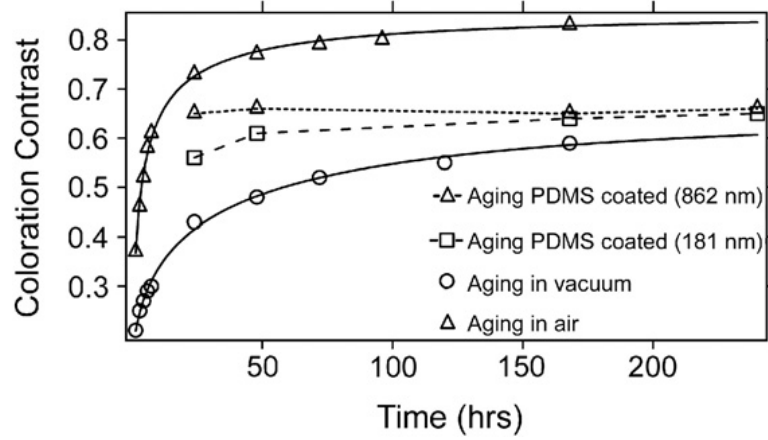the coloration contrast is still high enough to be easily detected.

Figure 5.10: Degradation of film sensitivities over time with and without a protective layer.

The mechanism behind the beneficial effect relies on PDMS's selective permeability to atmospheric gases that block any larger molecular pollutants present in the air. This experimental demonstration surely rules out catalytic poisoning due to CO since PDMS is known to be permeable to this gas ((13)). Physical blocking of pores due to water vapor as a possible retardant can also be dismissed on the same grounds ((14), (15)).

5.3.3 Conclusions

In summary, the limits of WO_3 as an optical gas sensor were derived by establishing the change in optical constants induced by 2% H_2 in Ar. By comparison to ion injection experiments I was able to conclude using the Langmuir adsorption model that the maximum coloration change was 57.9% of that achievable by electric field injection. PDMS layers were proven to be an effective protective coating against the deterioration of gasochromic effect in WO_3 films.

112

References

1. Deb, S. (1973) Optical and photoelectric properties and colour centres in thin films of tungsten oxide. <u>Philosophical Magazine</u> **27**, 801–822

2. Vitry, V., Renaux, F., Gouttebaron, R., Dauchot, J., and Hecq, M. (2006) Preparation and characterization of gasochromic thin films. <u>Thin solid films</u> **502**, 265–269

3. Georg, A., Graf, W., Schweiger, D., Wittwer, V., Nitz, P., and Wilson, H. (1998) Switchable glazing with a large dynamic range in total solar energy transmittance (tset). <u>Solar Energy</u> **62**, 215–228

4. Georg, A., Graf, W., Neumann, R., and Wittwer, V. (2000) Mechanism of the gasochromic coloration of porous wo₃ films. <u>Solid State Ionics</u> **127**, 319–328

5. Lee, S., Cheong, H., Liu, P., Smith, D., Tracy, C., Mascanrenhas, A., Pitts, J., and Deb, S. (2000) Gasochromic mechanism in a-wo thin films based on raman spectroscopic studies. <u>Journal of Applied Physics</u> **88**, 3076

6. Azens, A. and Granqvist, C. (2003) Electrochromic smart windows: energy efficiency and device aspects. <u>Journal of Solid State Electrochemistry</u> **7**, 64–68

7. Pedersen, T., Salinga, C., Weis, H., and Wuttig, M. (2003) Mechanical stresses upon hydrogen induced optical switching in thin films. <u>Journal of applied physics</u> **93**, 6034

8. Bange, K. (1999) Colouration of tungsten oxide films: A model for optically active coatings. <u>Solar Energy Material and Solar cells</u> **58**, 1–131

9. Granqvist, C. (1995) <u>Handbook of inorganic electrochromic materials</u>. Elsevier Science

10. Lundstrom, I. (1981) Hydrogen sensitive mos-structures. <u>Sensors and Actuators</u> **1**, 403–426

11. Von Rottkay, K., Rubin, M., and Wen, S. (1997) Optical indices of electrochromic tungsten oxide. <u>Thin Solid Films</u> **306**, 10–16

12. Wang, J., Bell, J., and Skryabin, I. (1999) Kinetics of charge injection in sol–gel deposited wo$_3$. <u>Solar energy materials and solar cells</u> **56**, 465–475

13. Merkel, T., Gupta, R., Turk, B., and Freeman, B. (2001) Mixed-gas permeation of syngas components in poly (dimethylsiloxane) and poly (1-trimethylsilyl-1-propyne) at elevated temperatures. <u>Journal of Membrane Science</u> **191**, 85–94

14. Shanak, H., Schmitt, H., Nowoczin, J., and Ziebert, C. (2004) Effect of pt-catalyst on gasochromic wo$_3$ films: optical, electrical and afm investigations. <u>Solid state ionics</u> **171**, 99–106

15. Georg, A., Graf, W., Neumann, R., and Wittwer, V. (2000) Stability of gasochromic wo$_3$ films. <u>Solar energy materials and solar cells</u> **63**, 165–176

Chapter 6

Conclusion

In this thesis I have shown a way to obtain tailored film structures varying from thin compact structures to open porous networks. The film structure is shown to be dependent on the forward momentum remaining in particles when they reach the substrate. Modulating factors which affect the final forward momentum (pulse energy, background gas pressure, target to substrate distance) produce films with widely-varying structures, while changing other parameters (pulse rate, number of pulses) does not. Smooth, compact films are obtained when particles reach the substrate with high forward momentum (high pulse energy, low background gas pressure, small target to substrate distance) while open porous structures are obtained for particles reaching the substrate with small forward momentum (low pulse energy, high background pressure, large target to substrate distance). Between these extreme cases, vertically-aligned nanostructures may be obtained with the right set of deposition parameters.

These vertically-aligned structures were shown to be especially applicable for photoanodes used in dye sensitized solar cells. TiO$_2$ photoanodes based on conventional sol-gel routes were compared to films obtained using pulsed laser deposition. Better DSSC device performances were noted for vertically-aligned structures obtained from PLD compared to the conventional nanoparticle films as well as other structures ob-

tained using PLD. Improved device performance was attributed to a combination of high dye loading (due to nanoparticles) and improved charge transfer pathways (due to vertical alignment).

Nb_2O_5 was also fabricated under different PLD growth conditions. Amongst the different PLD-Nb_2O_5 structures, vertically-aligned structures performed best as DSSC devices for reasons similar to those mentioned in the last paragraph. Devices performances of Nb_2O_5-DSSCs were worse than those of TiO_2 due to a combination of lower dye loading and lower conduction band.

DSSCs based on PLD-fabricated TiO_2 and Ta doped TiO_2 were compared. Devices made with Ta-doped TiO_2 were shown to have better overall device performance. Ta-TiO_2 showed much improved photocurrents over those of TiO_2 for all thicknesses. This increased photocurrent was due to the lower recombination rate of Ta: TiO_2.

Other applications of PLD nanostructures were also explored. These included synthesis of thin compact films for energy band measurements of different metal oxides using X-ray and Ultra violet photoemission spectrocopy (XPS-UPS) and Inverse photoemission spectroscopy (IPS). Further applications explored using PLD-WO_3 as a H_2 gas sensor. Optical constants for the PLD-WO_3 film in the colored and bleached states were measured and gasochromic and elctrochromic changes were correlated. A PDMS covering of the film was shown to reduce aging of films noticeably.

References

1. Deb, S. (1973) Optical and photoelectric properties and colour centres in thin films of tungsten oxide. Philosophical Magazine **27**, 801–822

2. Vitry, V., Renaux, F., Gouttebaron, R., Dauchot, J., and Hecq, M. (2006) Preparation and characterization of gasochromic thin films. Thin solid films **502**, 265–269

3. Georg, A., Graf, W., Schweiger, D., Wittwer, V., Nitz, P., and Wilson, H. (1998) Switchable glazing with a large dynamic range in total solar energy transmittance (tset). Solar Energy **62**, 215–228

4. Georg, A., Graf, W., Neumann, R., and Wittwer, V. (2000) Mechanism of the gasochromic coloration of porous wo$_3$ films. Solid State Ionics **127**, 319–328

5. Lee, S., Cheong, H., Liu, P., Smith, D., Tracy, C., Mascanrenhas, A., Pitts, J., and Deb, S. (2000) Gasochromic mechanism in a-wo thin films based on raman spectroscopic studies. Journal of Applied Physics **88**, 3076

6. Azens, A. and Granqvist, C. (2003) Electrochromic smart windows: energy efficiency and device aspects. Journal of Solid State Electrochemistry **7**, 64–68

7. Pedersen, T., Salinga, C., Weis, H., and Wuttig, M. (2003) Mechanical stresses upon hydrogen induced optical switching in thin films. Journal of applied physics **93**, 6034

8. Bange, K. (1999) Colouration of tungsten oxide films: A model for optically active coatings. Solar Energy Material and Solar cells **58**, 1–131

9. Granqvist, C. (1995) Handbook of inorganic electrochromic materials. Elsevier Science

10. Lundstrom, I. (1981) Hydrogen sensitive mos-structures. Sensors and Actuators **1**, 403–426

11. Von Rottkay, K., Rubin, M., and Wen, S. (1997) Optical indices of electrochromic tungsten oxide. Thin Solid Films **306**, 10–16

12. Wang, J., Bell, J., and Skryabin, I. (1999) Kinetics of charge injection in sol–gel deposited wo$_3$. Solar energy materials and solar cells **56**, 465–475

13. Merkel, T., Gupta, R., Turk, B., and Freeman, B. (2001) Mixed-gas permeation of syngas components in poly (dimethylsiloxane) and poly (1-trimethylsilyl-1-propyne) at elevated temperatures. Journal of Membrane Science **191**, 85–94

14. Shanak, H., Schmitt, H., Nowoczin, J., and Ziebert, C. (2004) Effect of pt-catalyst on gasochromic wo$_3$ films: optical, electrical and afm investigations. Solid state ionics **171**, 99–106

15. Georg, A., Graf, W., Neumann, R., and Wittwer, V. (2000) Stability of gasochromic wo$_3$ films. Solar energy materials and solar cells **63**, 165–176